# BRNO UNIVERSITY OF TECHNOLOGY
VYSOKÉ UČENÍ TECHNICKÉ V BRNĚ

## FACULTY OF MECHANICAL ENGINEERING
FAKULTA STROJNÍHO INŽENÝRSTVÍ

## INSTITUTE OF PHYSICAL ENGINEERING
ÚSTAV FYZIKÁLNÍHO INŽENÝRSTVÍ

# DESIGN OF THE TRANSMISSION ELECTRON MICROSCOPE PROJECTION SYSTEM FOR THE SINGLE PARTICLE ANALYSIS
NÁVRH PROJEKTOROVÉ SOUSTAVY TRANSMISNÍHO ELEKTRONOVÉHO MIKROSKOPU PRO METODU SINGLE PARTICLE ANALYSIS

## MASTER'S THESIS
DIPLOMOVÁ PRÁCE

**AUTHOR**            Bc. Ondřej Bačo
AUTOR PRÁCE

**SUPERVISOR**            Ing. Ondřej Sháněl, Ph.D.
VEDOUCÍ PRÁCE

**BRNO 2020**

# Specification Master's Thesis

Pursuant to Act no. 111/1998 concerning universities and the BUT study and examination rules, you have been assigned the following topic by the institute director Master's Thesis:

## Design of the Transmission Electron Microscope projection system for the Single Particle Analysis

**Concise characteristic of the task:**

The Single Particle Analysis (SPA) method allows scientists around the world to study structures of proteins, viruses and other biological samples by reconstructing a 3D model of the studied biological entity from a series of Transmission Electron Microscope (TEM) images. Although individual images usually do not allow a direct study of the structure, they still have to be acquired with the highest possible resolution which can only be achieved with high magnification and low distortion projection system to enable final 3D reconstruction from thousands of 2D images. The main focus of this diploma thesis is to design a new TEM projection system which will provide optimal magnification and distortion for SPA method. Optical properties of the projector lenses will be computed using Electron Optical Design software (EOD). Different approaches and approximations (e.g. thin vs. thick lens) will be used to obtain magnification series and optical properties of the projection system by matrix optics.

**Goals Master's Thesis:**

1. Provide a theoretical study of the TEM and SPA.
2. Introduce new optimized TEM projection system for SPA use case.
3. Compare results of different approaches to obtain optical properties of the introduced TEM projection system.

**Recommended bibliography:**

HAWKES, P. W. a E. KASPER. Principles of electron optics. Second edition. London: Elsevier/AP, Academic Press, an imprint of Elsevier, 2018. ISBN 978-008-1022-566.

ORLOFF, J. Handbook of Charged Particle Optics. 2. Boca Raton: CRC Press, 2009. ISBN 978-14-
-0045-543.

Deadline for submission Master's Thesis is given by the Schedule of the Academic year 2019/20

In Brno,

L. S.

..............................................                    ..............................................
prof. RNDr. Tomáš Šikola, CSc.                    doc. Ing. Jaroslav Katolický, Ph.D.
Director of the Institute                                           FME dean

**Abstrakt**
Předkládaná práce se zabývá návrhem projektorové soustavy transmisního elektronového mikroskopu (TEM) pro metodu single particle analysis (SPA). Návrh projektorové soustavy byl vytvořen v programu Electron Optical Design (EOD) verze 4.020. Série buzení jednotlivých čoček pro zvětšení projektorové soustavy v rozsahu od 50 do 10 000 byla vypočítaná pomocí přístupu využívajícího aproximaci tenké čočky, dále pomocí přístupu využívajícího aproximaci tlusté čočky, metodou linearního zaostření v programu EOD a metodou nelineárního zaostření v programu EOD ve verzi 5.003. Dosažené výsledky byly porovnány a ověřeny pomocí reálného trasování částic v programu EOD.

**Summary**
This thesis deals with the design of the transmission electron microscope (TEM) projection system for single particle analysis (SPA). The projection system design was created in Electron Optical Design (EOD) software version 4.020. The lens excitation series for projection system magnifications ranging from 50 to 10 000 were calculated using thin lens approximation approach, thick lens approximation approach, EOD linear focus method and EOD nonlinear focus method, as implemented in 5.003 version. Obtained results were compared and validated utilizing EOD real particle tracing method.

**Klíčová slova**
TEM, SPA, projektorová soustava, elektronová optika, EOD, paraxialní aproximace

**Keywords**
TEM, SPA, projection system, electron optics, EOD, paraxial approximation

I declare that I have written my master's thesis on the theme of "Design of the Transmission Electron Microscope projection system for the Single Particle Analysis" independently, under the guidance of the master's thesis supervisor and using the technical literature and other sources of information which are all quoted in the thesis and detailed in the list of literature at the end of the thesis. As the author of the master's thesis I furthermore declare that, as regards the creation of this master's thesis, I have not infringed any copyright. In particular, I have not unlawfully encroached on anyone's personal and/or ownership rights and I am fully aware of the consequences in the case of breaking Regulation S 11 and the following of the Copyright Act No 121/2000 Sb., and of the rights related to intellectual property right and changes in some Acts (Intellectual Property Act) and formulated in later regulations, inclusive of the possible consequences resulting from the provisions of Criminal Act No 40/2009 Sb., Section 2, Head VI, Part 4.

<div align="right">Ondřej Bačo</div>

# Contents

# Introduction

Transmission electron microscopy is an exceptionally powerful and versatile microscopic technique, which accelerated research in chemistry, materials science, physics and biology. The first transmission electron microscope was developed in 1931 by Ernst Ruska and Max Knoll and although its potential was immediately recognized by many scientists and technological companies, it took decades to reach an atomic resolution and to fully discover its potential.

Many technological challenges had been overcome in the past 90 years and reaching an atomic resolution on modern computer controlled transmission electron microscopes became a routine task even for novice users. This aspect played the key role in the technology adoption and nowadays hundreds of transmission electron microscopes are manufactured every year.

Three years ago, in 2017, transmission electron microscopy reached another important milestone. It is the year when Jacques Dubochet, Joachim Frank and Richard Henderson were awarded the Nobel Prize in Chemistry for developing cryo-electron microscopy for the high-resolution structure determination of biomolecules in solution [1]. Their extensive research in the field of sample vitrification and image reconstruction and analysis was rapidly accelerated by recent developments in direct electron detection and caused a revolution in 3D imaging of single biological assemblies. This leas to an ever-growing number of new entries to the protein data bank by cryo-electron microscopy.

The dominant cryo-electron microscopy contributor is the single particle analysis method, which uses images of thousands of randomly distributed biomolecules to determine their 3D structure with few-angstrom resolution. [2, 3, 4, 5]. Therefore, the objective lens and the projection system of a transmission electron microscope must ensure that the information about the finest details is transferred from the sample to the detector. The main goal of this thesis is to create the optical design of the projection system, which enables single particle analysis measurements.

The first chapter of this thesis is dedicated to transmission electron microscopy. Discussed is the design of a transmission electron microscope as well as transmission electron microscopy techniques and theory of the contrast origin. In the second chapter, matrix optics formalism is introduced and the rest of the chapter deals with charged particle optics. The trajectory equation is derived and its paraxial approximation is put into context of aberration theory of round magnetic lenses.

The third chapter highlights the growing importance of single particle analysis method. Single particle analysis workflow is explained step-by-step including the sam-

ple preparation steps.

The last part of this thesis describes the designed optical model of the projection system. Roles of various parameters are studied and documented by numerous figures. Thick lens approximation, thin approximation and linear and nonlinear focus methods implemented in Electron Optical Design software are used to obtain lens excitation series for the final projection system design. Their results are compared and validated.

# 1. Transmission Electron Microscopy

In transmission electron microscopy (TEM, note that in the following text the same abbreviation is used also for the instrument itself, the transmission electron microscope), a thin specimen is irradiated with an electron beam, transmitted electrons are then detected and an image is obtained. The acceleration voltage of a common instrument ranges from 60 to 300 kV. Although high-voltage instruments with the acceleration voltage reaching 3 MV exist, they are not discussed in this thesis [6].

Incident electrons are strongly interacting with a matter and therefore only very thin specimens can be studied. The typical thickness of specimen spans from units to a few hundred of nanometers, depending on the used acceleration voltage and on the density and elemental composition of the specimen. Sample preparation methods include wide variety of techniques such as chemical etching, ion etching, ion milling, microtomy, vitrification and many others. These techniques enable crystalline materials, polymers, semiconductor devices and even biological samples to be studied inside a TEM with atomic resolution.

In the last decade, 3D reconstruction of biomolecules with atomic resolution became a routine task, thanks to the developments in sample vitrification, data processing and electron detection. The enhanced stability of electronics and mechanical construction, more precise machining, together with improvements in user-friendliness, namely automated sample insertion and software assisted microscope alignments, resulted in recent increases of sample throughput. All these developments transformed a TEM from a purely scientific instrument to a robust and multifunctional tool which is not being used for reasearch purposes only, but also to control fabrication quality of semiconductor devices or to troubleshoot the drug development process in pharmaceutical companies.

Following subchapters are dedicated to 3 essential parts of the TEM design and to the explanation and instrumentation of the most common TEM techniques.

## 1.1 TEM Design

This subchapter describes the essential TEM parts that are directly related to the electron beam. In the first part, the differences between used electron emission regimes are explained and characteristics of the most frequently used TEM electron guns are listed and compared. The following part is dedicated to the electron optical elements and their design. The physics of electron optics is then described in the dedicated chapter 2. The last part of this subchapter explains various electron detection approaches.

Note that there is a long list of TEM modules which are also necessary for its operation, e.g. vacuum and cooling systems, electronic controllers, etc. There is an even longer list of the modules which enhance the imaging performance or enable new ways of measurement and analysis, like aberration correctors, electron energy filters or ultrafast laser systems. Unfortunately these topics exceed the scope of this thesis and thus are not discussed. These books [7, 8, 6] may serve as a source of high quality information on the basic and also many advanced topics.

### 1.1.1 Electron Sources

A design of an electron source (emitter) determines the key electron beam parameters, its brightness and energy spread. Both are critical to the imaging performance of the TEM. But these are not the only parameters that characterize electron guns. Different emitters have different vacuum requirements and high demands are put also on the beam current stability, emitter lifetime and its price, see Tab. 1.1. Based on the emission regime, electron sources can be divided into three groups – thermionic, Schottky and field emission sources.

Tab. 1.1: Characteristics of main electron sources used in transmission electron microscopes [7, 9, 10, 11, 12, 13].

|  | Units | Tungsten filament | LaB$_6$ | Schottky emitter | CFEG |
|---|---|---|---|---|---|
| Emission regime | – | thermionic | thermionic | thermionic | cold field |
| Operational temperature | K | 2700 | 1700 | 1700 | 300 |
| Brightness (at 100 kV) | A/m$^2$sr | $10^{10}$ | $5 \times 10^{11}$ | $5 \times 10^{12}$ | $10^{13}$ |
| Energy spread (at 100 kV) | eV | 3 | 1.5 | 0.7 | 0.3 |
| Emission current stability | %/h | $< 1$ | $< 1$ | $< 1$ | $< 5$ |
| Required vacuum | Pa | $< 10^{-2}$ | $< 10^{-4}$ | $< 10^{-6}$ | $< 10^{-9}$ |
| Lifetime | h | 100 | $> 1000$ | $> 5000$ | $> 5000$ |
| Price | USD | 20 | 1000 | 3000 | 3000 |

**Thermionic Electron Sources**

In the thermionic regime, the emitter is heated to a high temperature, so energies of some of the conductance electrons exceed the work function, as shown in Fig. 1.1. The electron energy distribution changes with the temperature and thus it can be used to control the emission current and energy spread. However, at a certain temperature the emission current reaches its maximum and further heating results only in a reduced lifetime of the emitter. The most common thermionic emitter material in TEM electron source is a single crystal lanthanum hexaboride (LaB$_6$) [7]. Alternatively, the cerium hexaboride (CeB$_6$) single crystal can be used. It has similar properties and pricing to a LaB$_6$ emitter [13]. The other alternative is a tungsten filament, which has worse performance and thus is not frequently used in modern TEMs.

The emitter is used as a cathode in the electron gun assembly, see Fig. 1.2. Typically a high negative electrical potential ($\approx -100$ kV) is applied to the cathode and emitted

electrons are accelerated towards an earthed anode. A small negative bias is applied to the Wehnelt cup, which acts as an electrostatic lens. It can be shown that there exists an optimum in emission current and a Wehnelt bias voltage, which ensures the highest brightness [7].
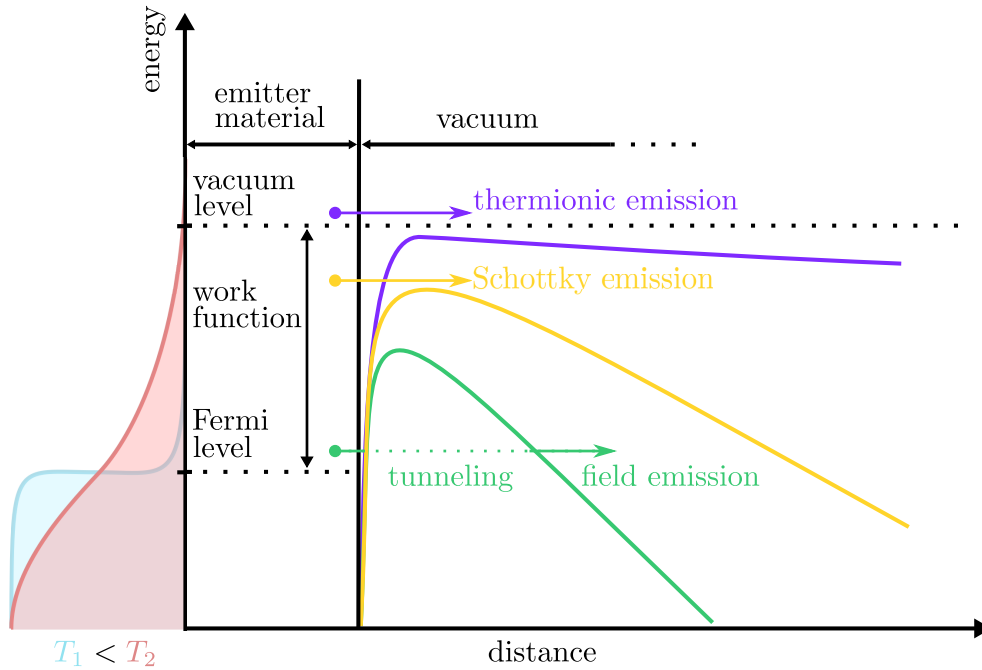


Fig. 1.1: Energy diagram at the emitter–vacuum boundary, with the distance perpendicular to an emitter surface on the horizontal axis and the energy on the vertical axis. Depicted are thermionic, Schottky and field emission principles. Denoted by the violet, yellow and green solid line are the surface barriers. The violet solid line shows the surface barrier in the presence of a low electric field at the emitter surface. The green line corresponds to the presence of the highest electric field. On the left side of the diagram are shown probabilities of occupancy of energy levels by electrons for two different temperatures, $T_1$ (light blue) lower than $T_2$ (light red).

**Schottky Electron Sources**

Schottky sources are often categorized as field emission guns, but when used in TEMs and operated under normal conditions, they work in thermionic regime [8]. The emitter is negatively biased relative to its surrounding and a high electric field at the emitter surface lowers the surface barrier as shown in Fig. 1.1. This phenomenon is called the Schottky effect. The emitter is a single crystal tungsten tip with a zirconium oxide coating and a reservoir around it, as shown in Fig. 1.3. Zirconium oxide layer lowers the work function of tungsten and together with the Schottky effect it allows to operate the source in thermionic regime at temperature of approximately $1800\,\mathrm{K}$ [7]. With its high brightness, generally over $5 \times 10^{12}$ at $100\,\mathrm{kV}$, and low energy spread of $0.7\,\mathrm{eV}$, the Schottky electron guns make atomic resolution measurements a routine. An exhaustive review of Schottky emitters by Lyn W. Swanson and Gregory A. Schwind can be found in [14].
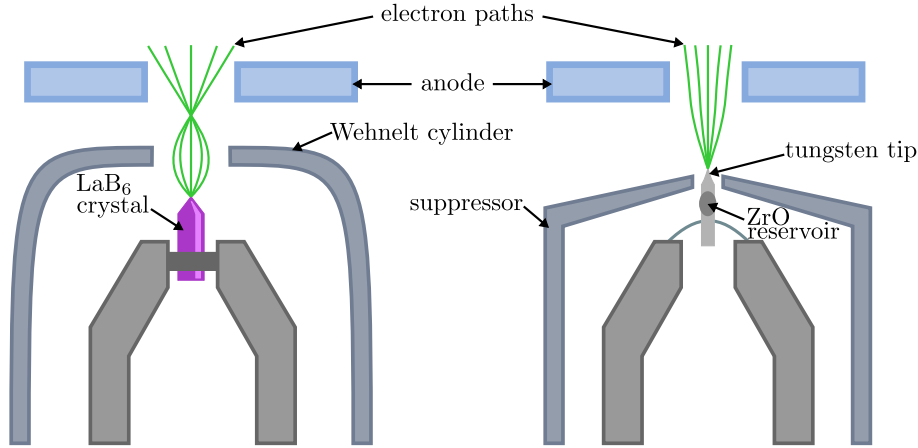
Fig. 1.2: Schematic depiction of a LaB$_6$ gun assembly (left) and a Schottky gun assembly (right). The configuration of electrodes in tungsten filament gun assemblies is identical to the LaB$_6$ configuration and the electrode configuration of a field emission gun is the same as the Schottky electron gun configuration.
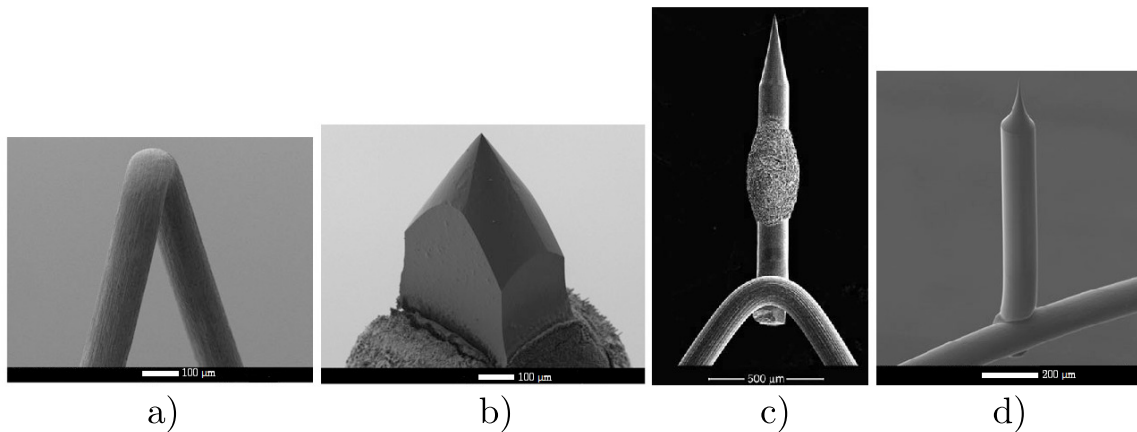


Fig. 1.3: a) Tungsten filament emitter, from [15]. b) LaB$_6$ emitter [15]. c) Schottky emitter, a tungsten monocrystal with a zirconium oxide reservoir attached to a tungsten filament, from [14]. d) Cold field emitter, a tungsten monocrystal attached to a tungsten filament, from [15].

**Field Emission Electron Sources**

Compared to thermionic and Schottky sources, current emitted from a field emission gun is not dominated by electrons which have higher energy than the surface barrier or the work function, but it is dominated by the electrons which tunneled through the barrier. Thus, in order to operate an electron gun in the field emission regime, the surface barrier has to be significantly lowered using the Schottky effect, to allow the electrons to tunnel through. The typical magnitude of the electric field at the emission surface is in the order of $10^{10}$ V/m. The surface has to be free of any contaminants. and to remain clean for a sufficient time and to avoid sparks from the tip emitter, the field emission gun requires ultra-high vacuum conditions ($< 10^{-9}$ Pa). The emitter is a tungsten monocrystal shaped into a sharp tip. The tip radius is similar to the Schottky emitter, it ranges from 100 nm to 1 µm. Unlike the Schottky emitter, the field emitter

is not coated and its work function depends only on the crystallographic orientation of the emitting surface.

The field emission regime can be further divided into thermally assisted field emission and cold field emission. Thermally assisted means, that the electron source is heated, but the emitted current is still dominated by tunneled electrons. A cold field emission gun (CFEG) is operated at room temperature. CFEG has the lowest energy spread of the mentioned electron sources and the highest brightness but it also has several drawbacks. The main drawback is the lower current stability. This is a direct consequence of gas adsorption on the emitting surface, which is higher at lower temperatures. The other drawback is its price. Although a cold field emitter itself comes at a similar price as a Schottky emitter, the price of the whole module is several times higher, which is mainly caused by high vacuum requirements.

## 1.1.2   Electron Optical Elements

With regard to how they act an electron beam, the basic TEM electron optical elements can be divided into four groups: lenses, deflectors, stigmators and apertures. Electron lenses change the convergence of the beam, deflectors change its angle against the optical axis, stigmators change its shape and apertures limit the beam. These effects are illustrated in Fig. 1.4. Different ways of usage of the optical elements are discussed in 1.2.
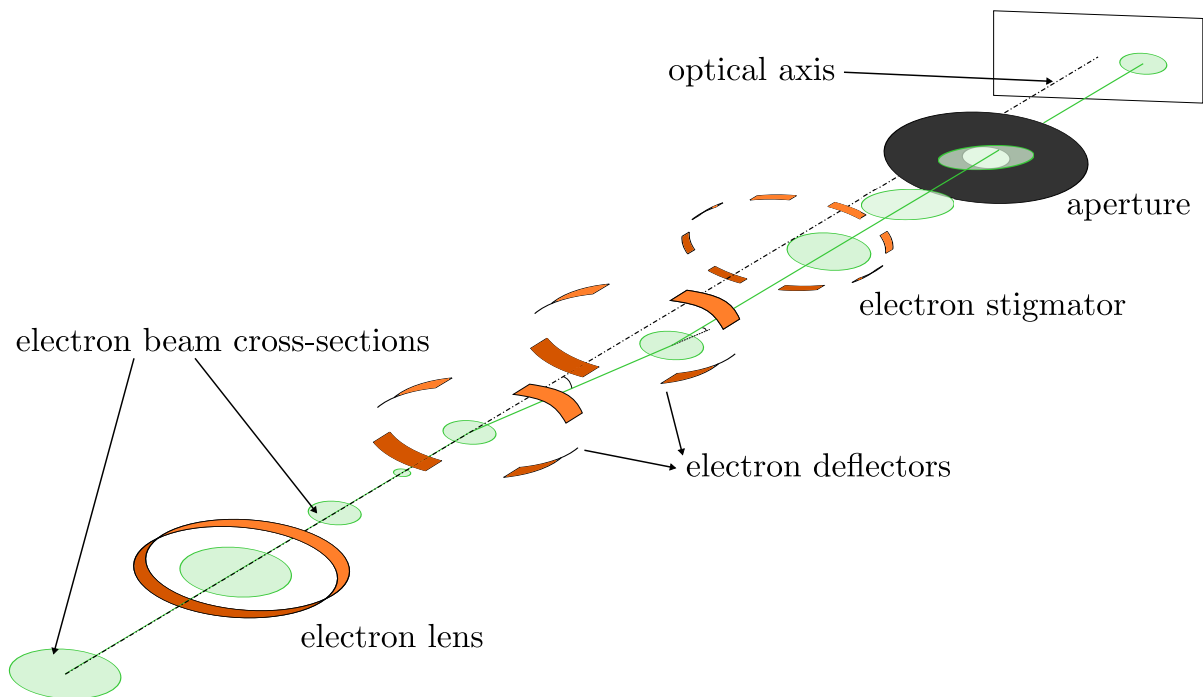


Fig. 1.4: Schematic drawing of the electron beam traveling from left to right through an electron lens, two sets of deflectors, a stigmator and an aperture. Shown are the beam cross-sections, denoted by green ellipses and circles.

**Electron Lenses**

Two types of electron lenses are used in TEMs, electrostatic lenses and magnetic lenses. Unlike the magnetic component of the Lorentz force (Eq. **??**), the electrostatic component does not scale with the charged particle's velocity, which is why the electrostatic lenses are mainly used to act on the beam before it is accelerated to high energies. In $LaB_6$ and tungsten filament electron guns, the Wehnelt cylinder acts as the first electrostatic lens, Fig. 1.2. An extractor in field emission and Schottky gun assemblies is often followed by an electrostatic gun lens, which creates the first crossover.

After an electron beam is accelerated, magnetic lenses are used to control the irradiated area of the specimen and to transfer transmitted electrons to a detector or a camera. Function-wise, lenses can be classified into three categories: condenser lens, objective lens and projector lens. Condenser lenses are placed above the specimen, and they control the incident beam. Typically three or four lenses, including condensor mini-lens [7], are used to control the size of illuminated area, the convergence angle and the beam current. The specimen is immersed in the magnetic field of the objective lens. The main benefit of this configuration is minimizing the spherical and the chromatic aberration [16]. The image or the diffraction pattern created by the objective lens is then magnified and transferred to a detection system using projector lenses. The number of projector lenses in a system may vary from three to five for different TEMs.

A schematic drawing of a general magnetic lens is shown in Fig. 1.5. Copper coil windings are positioned inside a cylindrically symmetrical yoke. A current through the coil generates a magnetic field inside the lens yoke and this field is directed by the polepieces to the gap between them as shown in Fig. 1.5, where the magnetic field is symbolized by red lines.
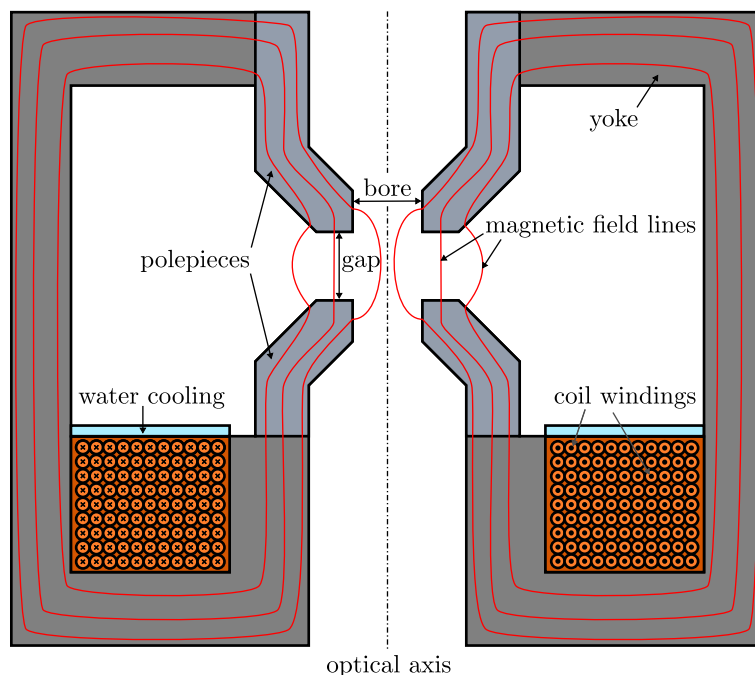


Fig. 1.5: Schematic drawing of a magnetic lens.

The passing current, not only generates the magnetic field, but it also produces

heat, which can cause thermal expansion of the polepieces. The produced heat can be transferred away by water cooled elements, which keep the lens temperature stable. The cooling system must be carefully designed not to cause any mechanical vibrations. The temperature stability is most critical in case of an objective lens because a specimen is positioned between its polepieces. Temperature changes near the specimen cause thermal drift of the specimen which significantly worsens the imaging performance of a TEM.

Lens design should ensure that the magnetic flux remains within its yoke and the coil region, except for the gap between polepieces. Since the magnetic field needs to be frequently changed during a TEM operation, e.g. illumination and magnification changes, the yoke and polepieces are made of magnetically soft materials, i.e. materials with low coercivity. The yoke is usually made of soft iron, but polepieces typically require higher saturation magnetization and that is why cobalt-iron alloys are often employed [17].

**Deflection Systems**

Electron beam deflection plays an essential role not only in scanning TEM (STEM), but also in conventional (i.e. static beam) TEM, where it ensures that the beam is aligned with optical axes of the lenses. The importance of this alignment is emphasized in section 2.4. Deflectors are positioned near TEM module interfaces, where the mechanical shift and tilt occurs, as shown in Fig. 1.6.
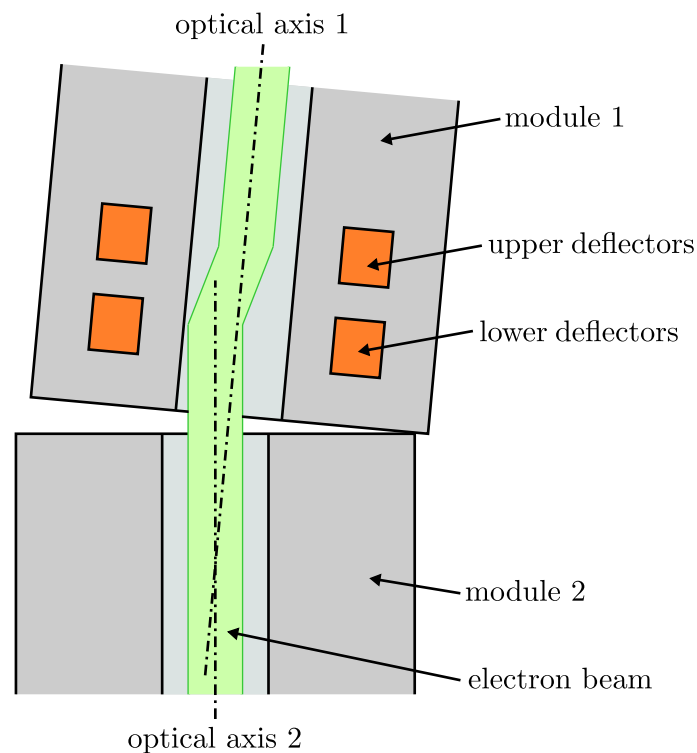


Fig. 1.6: Schematic drawing of two mechanically misaligned modules. An electron beam which travels along the optical axis of module 1 is tilted and shifted by double deflection system so it is aligned with the optical axis of module 2.

Commonly, three sets of deflectors are used in TEMs. The gun deflectors, which align an electron beam with the optical axis of the condensor module, the beam deflectors, which align the beam with the optical axis of the objective lens and the image deflectors, which align the beam with the optical axis of the projection system.

For given $x$-$z$ or $y$-$z$ plane, where $z$ is identical with the optical axis, one level of deflectors can only tilt the electron beam. Combination of two levels of the deflectors enables to shift or to tilt the beam independently. Deflectors are placed above each other and each level consists of two deflection elements perpendicular to each other, so deflection in an arbitrary direction may be achieved. Deflectors can be either electric or magnetic, but magnetic deflection systems are preferred in TEMs for the same reason magnetic lenses are preferred.

There are two different types of magnetic deflectors, the toroidal coils deflector and the saddle coils deflector, a) and b) in Fig. 1.7, respectively [18]. The most of TEMs use the saddle coils deflectors.
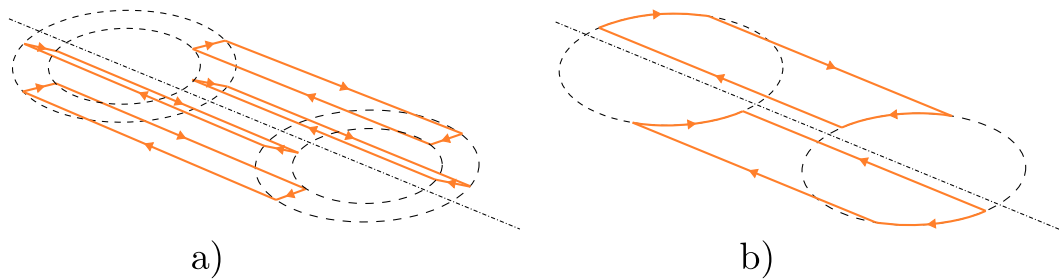


Fig. 1.7: Schematic drawing of a) toroidal coils deflector and b) saddle coils defletor. Arrows indicate electrical current direction through coils. Adapted from [18].

**Stigmators**

A stigmator, as its name suggests, is used to correct for astigmatism. This is a parasitic aberration of round optical elements, which raises from limited machining precision. As shown here [19], the ellipticity of magnetic lens polepieces acts as a source of astigmatism. Three stigmators are in general used in TEM to stigmate the incident beam, the image and the diffraction pattern created by an objective lens [20].

Astigmatism can be corrected by means of a quadrupole field, which can be produced by a set of four electrodes or four saddle coils. Stigmators using saddle coils are dominant in TEMs. However, to produce a quadrupole magnetic field of an arbitrary orientation, more than four saddle coils must be employed. Fig. 1.8 shows an example of creating an arbitrarily oriented quadrupole field utilizing eight saddle coils.
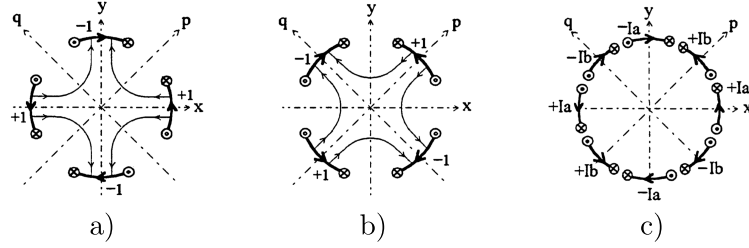
Fig. 1.8: Schematic depiction of principle of producing an arbitrarily oriented quadrupole field using eight saddle coils. In a), unit currents through four coils are used to created a xy oriented quadrupole field. In b), four 45°-rotated coils produce a pq oriented quadrupole field. c) combines a) and b), a linear combination of a) and b) currents can be used to produce a quadrupole field of an arbitrary strength and orientation. From [21].

**Apertures**

This section is dedicated to optical apertures, however there is an another type of apertures, which also play an important role in TEM. Differential pumping apertures are used to maintain a large difference in pressure between distinct vacuum sections of a TEM. Unlike the optical apertures, differential pumping apertures are not design to limit an electron beam. If it happens it may result in electron beam artifacts and cutoffs which significantly reduce the imaging performance of a TEM.

The optical apertures are used to limit the electron beam current or to control the beam convergence angle. There are also apertures which have more specific use case, such as objective aperture and selected area aperture. These are discussed later in 1.2.

In an accelerator module there is normally a set of several fixed apertures, which prevent stray electrons from propagating down the column. TEM condenser system can be equipped with two movable apertures, C1 and C2 aperture. The first condenser aperture C1 is used to increase the spatial coherence electron beam and the second condenser aperture C2 is generally used as the last beam limiting aperture. Hence its size has a direct impact on illumination conditions, namely the aperture angle, Fig. 1.11 d). A holder with apertures of multiple sizes or a strip aperture is used to provide an easy aperture size selection and centering. The size of commercially available apertures (including the objective and selected-area aperture) spans from tens to hundreds of micrometers [22].

### 1.1.3 Cameras and Detectors

Discussed bellow are only the forward-scattered electron detectors. X-ray, secondary electron or back-scattered electron detectors are out of scope of this thesis because they are not used for single particle analysis (SPA). For the same reason, there is only a basic distinction between STEM detectors with no further comments regarding their working principle. In following paragraphs, the terms detector and camera are used as follows: detector is a non-pixelated device which integrates detected signals, whereas camera is a pixelated signal detection device.

Electron detection and image recording belongs to the most rapidly developing

fields in TEM. Binoculars and photographic emulsions have been replaced by digital indirect and direct electron detection cameras. Fiber-coupled charge-coupled device (CCD) and complementary metal–oxide–semiconductor (CMOS) image sensors became a new standard for image recording in TEM [6]. Mentioned recent developments are strongly related to hardware and software advances in computer technology, which enable recording of high-resolution images at speeds which exceed 1000 frames per second [23].

TEM can accommodate multiple cameras and detectors. Here, they are divided into three categories with regard to their main purpose. A schematic cross-section of a detection module equipped with three STEM detectors, one alignment camera and two image recording cameras is shown in Fig. 1.9.
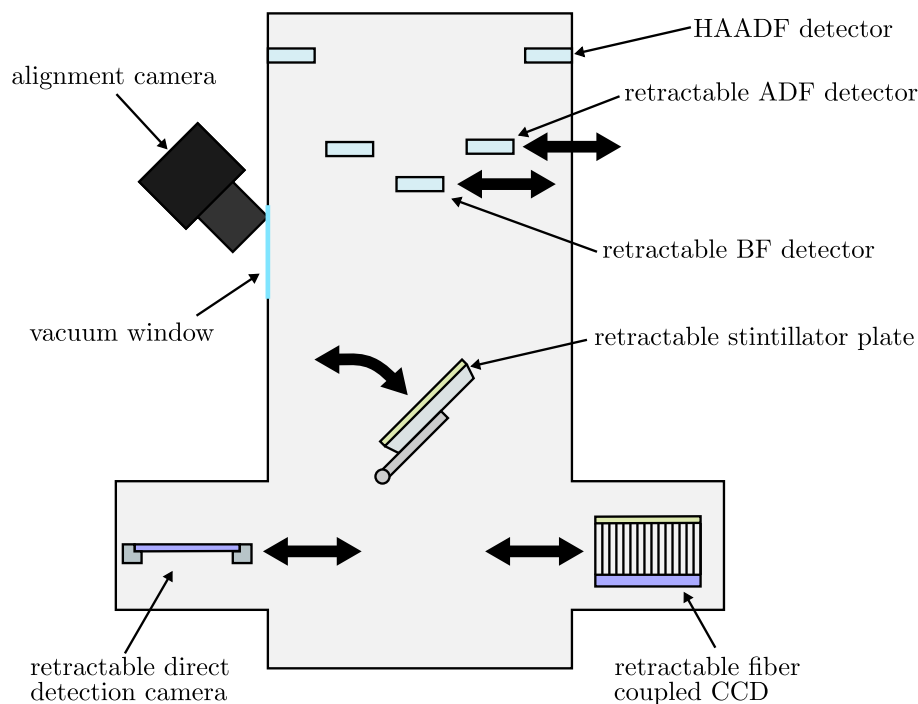


Fig. 1.9: Schematics of detection module equipped with HAADF, ADF and BF detectors, side-mounted alignment camera and two types of image recording cameras.

**Alignment Camera**

Modern TEMs are typically equipped with a basic camera which is used for optical alignment procedure. Fine alignments are then done on an image recording camera before a micrograph acquisition. As shown in Fig. 1.9, the alignment camera can be side-mounted to a detection module and record a signal coming from a retractable scintillator plate. The scintillator plate is a metal plate coated with a scintillation layer. Impinging electrons cause visible light flashes which are coupled by a camera lens.

The configuration with an alignment camera outside the vacuum chamber suffers from low detection efficiency and resolution, but it allows significant reduction in complexity and costs. Another advantage is that the scintillator plate can sustain much higher electron doses[1] than the more sensitive image recording cameras. An entire

---

[1]Electron dose in TEM is defined as charge per unit area $(C/m^2)$ [7]. Using the elementary charge

diffraction pattern or a focused electron beam can be imaged without causing any damage to the scintillator.

**High Resolution Image Recording Camera**

The main image recording camera is used to acquire high resolution micrographs. Generally it is mounted to the bottom of a detection module. There are two dominant TEM camera designs, fiber optical coupled and direct detection. Fig. 1.9 shows both of them mounted to the detection module, utilizing a retractable mechanism.

Fiber coupled CCD uses optical fibers coated with a scintillation layer, to directly couple visible light flashes to CCD pixels. Fiber coupling offers several times higher signal transfer efficiency than lens coupled systems [24]. In general, fiber optic couplers consist of hexagonal arrays of optical fibers fused together. Opaque fibers at array interfaces causes a "chicken wire" pattern, as shown in Fig. 1.10, and this artifact needs to be software corrected.
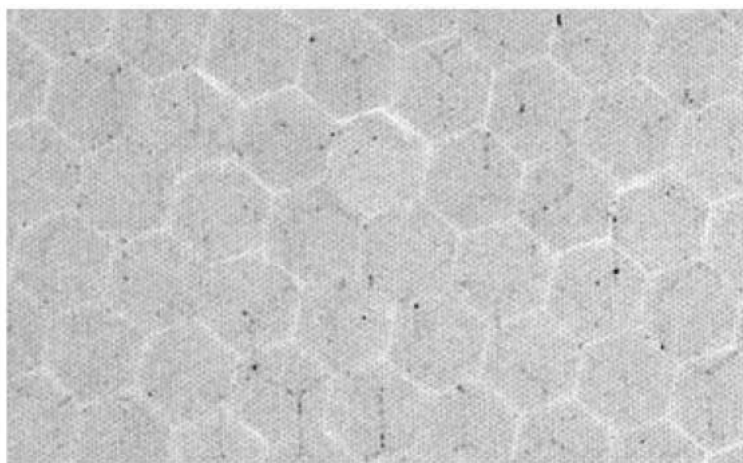


Fig. 1.10: A chicken wire pattern in fiber optical coupled CCD. From [24].

Direct detection cameras are quite a recent and quickly developing piece of technology. Because of its superior performance in low electron dose detection, it was immediately adopted by bioscientists, for whom the electron dose is a critical criterion. Thus, direct detection cameras became an essential part of cryogenic TEMs [25]. These cameras excel not only in low dose detection, but they also facilitate frame rates reaching 1500 frames per second [23]. However, exposing a direct detection camera to high electron doses may cause its permanent damage. Not only performance plays an important role in a new technology adoption, it is also the price at which it comes. The price is rather exclusive in case of direct detection cameras, which may cost up to 500 000 USD (2015) [8].

**Scanning TEM Detector**

In general there are three types of detectors, a high-angle annular dark-field (HAADF) detector, an annular dark-field (ADF) detector and a bright-field detector (BF). These

---

$e$ it can be easily converted to number of electron hits per area.

semiconductor detectors integrate the signal from each scanning point and convert it to the intensity of individual pixels, which build up a micrograph.

## 1.2 TEM Techniques

TEM is an instrument that can utilize a wide variety of sample analysis techniques. Explained below are the essential TEM imaging and diffraction techniques and selected advanced techniques. Single particle analysis is described later in chapter 3.

### 1.2.1 TEM Imaging

In a conventional TEM, the condenser lenses are used to illuminated the specimen with an electron beam parallel with the optical axis. The way of producing a parallel illumination is shown Fig. 1.11 a) and b). Displayed are not only condensor lenses C1 and C2, but also a condensor mini-lens and the upper part of an objective lens magnetic field, which also acts as part of the illumination system.
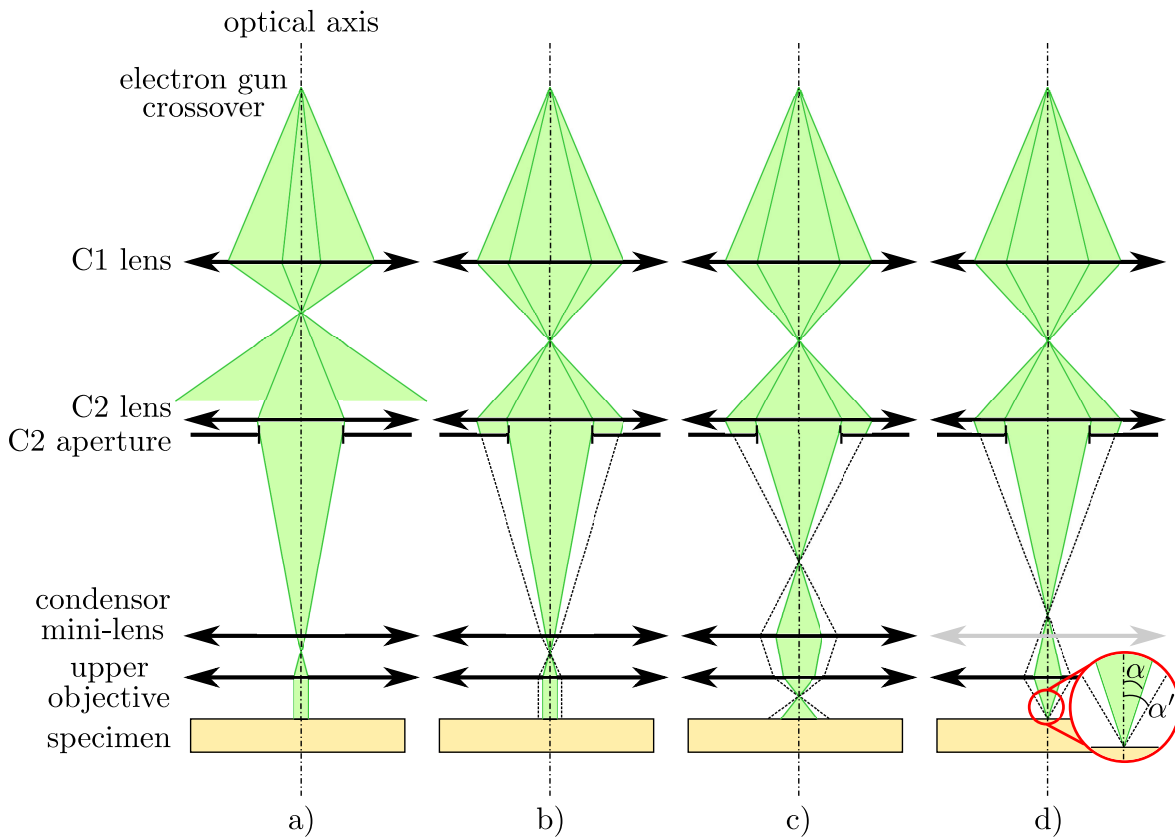


Fig. 1.11: Comparison of a) and b) shows the effect of changing C1 lens excitations. b) to c) comparison reveals the effect of C2 lens excitation on the size of the illuminated area. In d) the mini-lens is switched optically off and the C2 excitation is set, so the is focused on the specimen. The effect of the C2 aperture size is ilustrated by the dotted line.

However, mini-lens excitation is typically not varied and it is operated in two regimes. It either acts as a lens or it is not optically active, meaning it does not

affect the electron beam. And since excitation of the objective lens is only fine-tuned, illumination conditions are controlled by C1 and C2 lenses. Note that with such restrictions, the shown condensor system cannot be used to maintain parallel illumination while the size of illuminated area is continuously changed. To provide such capability a C3 lens has to be introduced between the C2 lens and the condensor mini-lens [7].

C1 lens excitation can be used in combination with C2 aperture to reduce the beam current, i.e. the current that reaches the specimen. This is illustrated by Fig. 1.11 a) and b). Note that the excitation of C2 lens also changes in order to maintain the size of an illuminated area.

Fig 1.11 b) and c) demonstrate the effect of increasing the C2 lens excitation on illumination conditions. Excitations of other lenses are the same as in b). The illumination is no longer parallel and the size of the illuminated area increases.

The incident electron beam is scattered by a thin specimen. Scattered and unscattered electrons are transferred by a projection system to create a micrograph, which is recorded by a camera. To explain the origin of contrast in a micrograph, it is necessary to think about the incident beam as an electron wave. Both the electron wave amplitude and phase can be changed by a specimen and both changes give rise to contrast. Although both the amplitude and phase contrast contribute to an image, conditions are typically set so that one dominates [7]. Phase contrast is described in more detail because it explains the contrast origin in single particle analysis micrographs.

**Amplitude Contrast Imaging**

Amplitude contrast describes the image intensity at low and medium magnifications [6]. It is caused by mass and thickness variations in the specimen. Electrons passing through higher density or thicker areas are scattered more than those passing through low density or thin areas. Fig. 1.12 highlights the fact that distinguishing between the sample density and thickness is not straightforward. Hence both are frequently connected to a single factor called mass thickness $x = \rho t$, where $\rho$ is the mass density and $t$ the specimen thickness [6].

The image contrast can be enhanced by an objective aperture which is positioned in the back focal plane of an objective lens. The transmission of electrons through the objective aperture decreases exponentially with increasing mass thickness [6]. Since electrons with lower energy are scattered more than those with higher energy, lowering the acceleration voltage may be also used to increase image contrast. The effect of an objective aperture size on image contrast is demonstrated in Fig. 1.13.

The objective aperture can be positioned to let through either scattered electrons, or unscattered ones, as shown in Fig. 1.14. This is called dark-field (DF) and bright-field (BF) imaging, respectively. DF images have typically lower overall intensity than BF images, hence the terms 'dark' and 'bright', but they yield better contrast. Side by side comparison of BF and DF micrographs is shown in 1.15.

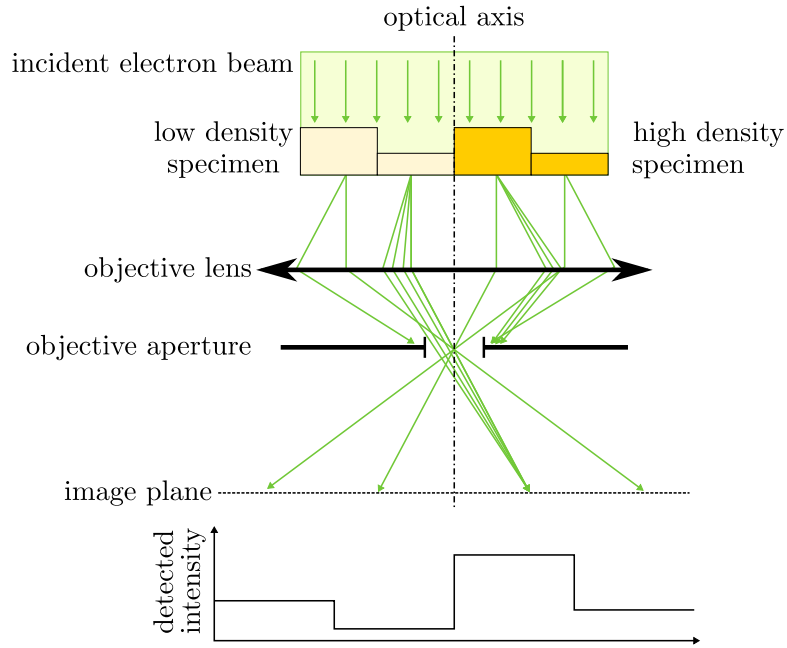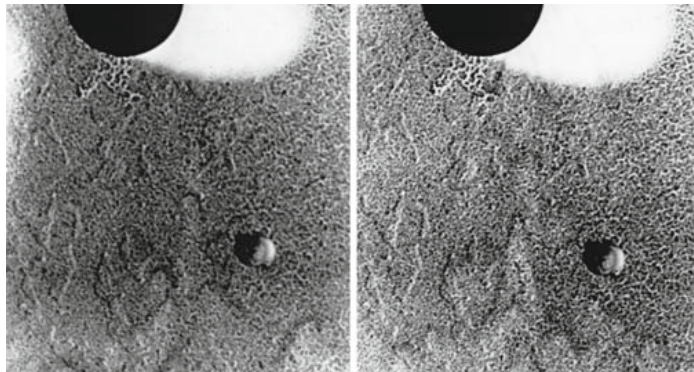Fig. 1.12: Schematic drawing of the contrast enhancement by the objective aperture.



Fig. 1.13: Two images of the same sample area taken using two different sizes of the objective aperture. Image taken with lower size of the aperture is shown on the right. From [7].
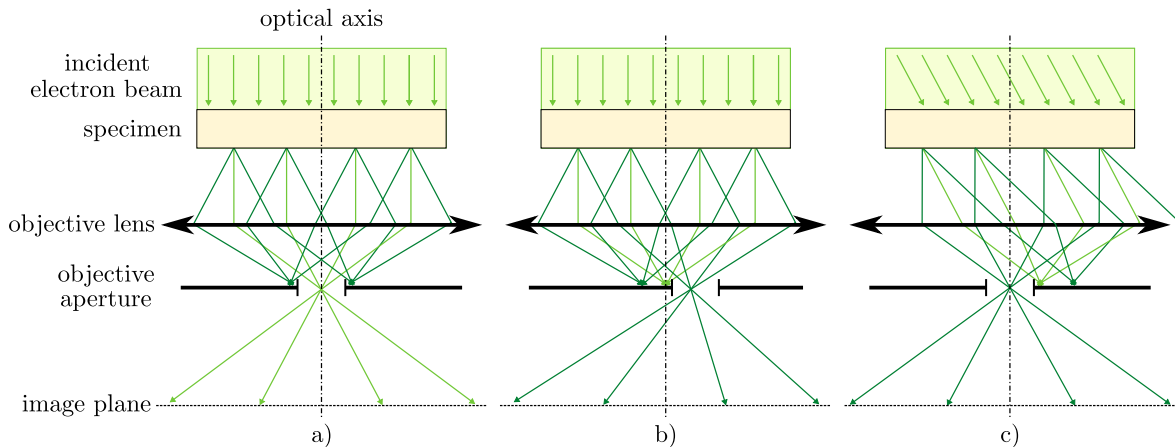


Fig. 1.14: a) Schematic drawing of BF image acquisition. DF image acquisition with parallel beam shown in b) and with tilted beam illumination shown in c).
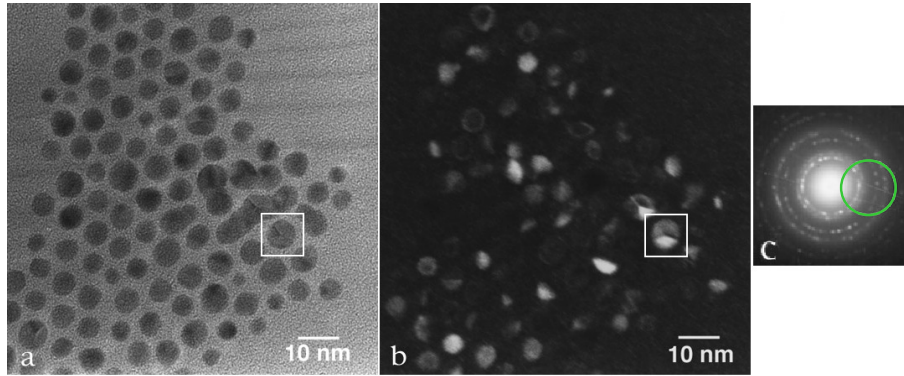
Fig. 1.15: a) BF and b) DF amplitude contrast images of the same area. The green circle in c) denotes the position of the objective aperture during DF image acquisition. From [26].

**Diffraction Contrast Imaging**

Diffraction contrast can be considered a special form of amplitude contrast where electrons are scattered at special angles [7]. As explained in 1.2.2, this occurs when a crystalline specimen is illuminated with a parallel electron beam. BF diffraction contrast imaging is achieved by selecting only the central diffraction spot with the objective aperture. By selecting other strong (high intensity) spot DF diffraction contrast micrograph can be acquired. Fig. 1.16 shows both DF and BF diffraction contrast micrographs of germanium nanowire with a gold catalyst.



a)                              b)                              c)
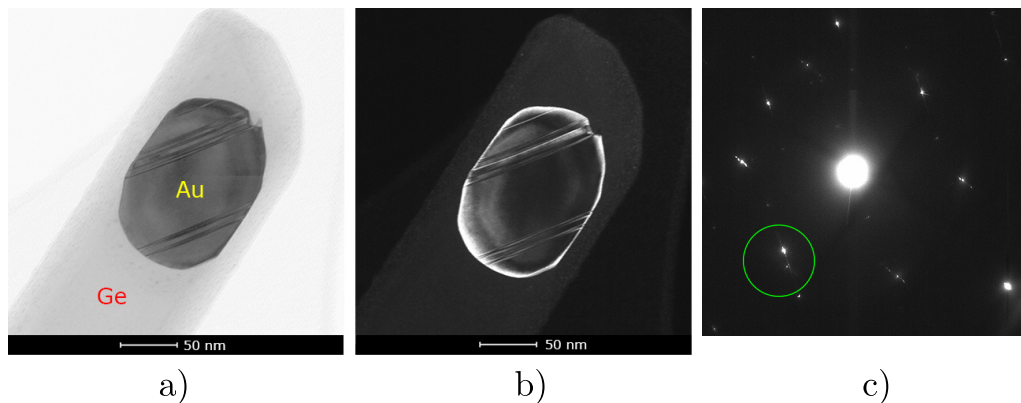
Fig. 1.16: a) BF and b) DF diffraction contrast images of the same area. The green circle in c) denotes the position of the objective aperture during DF image acquisition. From [27].

**Phase Contrast Imaging**

To describe the contrast of a high-resolution transmission electron microscopy micrograph, the wave properties of electrons must be employed. The contrast arises from the interference of transmitted and scattered electron waves in the image plane. Considering a very thin sample, the amplitude of both electron waves remains the same but unlike the transmitted wave, the scattered electron wave undergoes a phase shift. This sample-induced phase modulation of incident electron wave can be expressed as

$e^{-i\phi(\mathbf{r})}$, where $\phi(\mathbf{r})$ is the object function and $\mathbf{r} = \mathbf{r}(x,y)$ denotes a 2D position vector in the thin sample. Assuming a very small phase shift ($\phi \ll 1$) yields:

$$e^{-i\phi(\mathbf{r})} = 1 - i\phi(\mathbf{r}).$$

This approximation is called the weak phase object approximation. Further, assuming ideally parallel illumination of the sample, the incident electron wave $\psi_{\text{in}} = Ae^{-ik_z z}$ is independent of $x$ and $y$ thus it can be written as follows:

$$\psi_{\text{in}}(\mathbf{r}) = \mathbf{constant} = 1.$$

The wave emerging from the sample is obtained by multiplying the incident wave and phase modulation

$$\psi_{\text{ex}}(\mathbf{r}) = \psi_{\text{in}}(\mathbf{r})\left[1 - i\phi(\mathbf{r})\right] = 1 - i\phi(\mathbf{r}). \tag{1.1}$$

According to Abbe's theory of imaging, the objective lens image formation can be described in two steps, as shown in Fig. 1.17. The exit wave (1.1) is then focused by the lower part of the objective lens field to its back focal plane. Since the back focal plane is the image plane of infinity, the far-field condition of Fraunhofer diffraction, which can be represented as the Fourier transform of the exit-plane wave, is fulfilled [28].

$$\psi_{\text{BFP}}(\mathbf{q}) = \mathcal{F}[\psi_{\text{ex}}(\mathbf{r})] = \psi_{\text{ex}}(\mathbf{q}),$$

where $\mathbf{q} = (q_x, q_y)$ denotes the 2D position vector in the spatial frequency domain in the back focal plane.

The next step is to describe effects of the lower part of the objective lens field on the electron wave phase, which can be done by means of the contrast transfer function (CTF). The CTF itself consists of phase contrast transfer function $PCTF = \text{Im}\{CTF\}$ and amplitude contrast transfer function $ACTF = \text{Re}\{CTF\}$. The PCTF here, i.e. only the imaginary part of the CTF, is sometimes referred to as CTF. In such texts the effect of ACTF on the intensity in the image plane is not usually discussed since its contribution to the CTF is, for thin samples, significantly lower than the phase contrast effects introduced by PCTF. In general, for samples with no or very low absorption and inelastic scattering of electrons, the ACTF can be omitted and only PCTF is taken into account.

The wave is modified by the transfer function CTF (or just PCTF for thin samples) and propagates further to the image. The propagation from the back focal plane to the image plane can be described by means of inverse Fourier transform and hence

$$\psi_{\text{det}}(\mathbf{r}) = \mathcal{F}^{-1}[CTF(\mathbf{q})\psi_{\text{ex}}(\mathbf{q})]. \tag{1.2}$$

Using (1.2), the intensity in the image plane can be written as

$$I(r) = |\psi_{\text{det}}(\mathbf{r})|^2 = \psi_{\text{det}}(\mathbf{r})\overline{\psi}_{\text{det}}(\mathbf{r}),$$

where the bar denotes complex conjugate.

optical axis z

$\psi_{\mathrm{in}} = Ae^{-\mathrm{i}k_z z}$

sample

$\psi_{\mathrm{ex}}(\vec{\mathbf{r}}) = \psi_{\mathrm{in}}(\vec{\mathbf{r}})\left[1 - \mathrm{i}\phi(\vec{\mathbf{r}})\right] = 1 - \mathrm{i}\phi(\vec{\mathbf{r}})$

$\overline{\theta}$

lower objective lens

$\psi_{\mathrm{BFP}}(\mathbf{q}) = \mathcal{F}[\psi_{\mathrm{ex}}(\mathbf{r})] = \psi_{\mathrm{ex}}(\mathbf{q})$

back focal plane

$\psi_{\mathrm{det}}(r) = \mathcal{F}^{-1}[CTF(\mathbf{q})\psi_{\mathrm{ex}}(\mathbf{q})]$

screen, image plane

$I(r) = |\psi_{\mathrm{det}}(\mathbf{r})|^2 = \psi_{\mathrm{det}}(\mathbf{r})\overline{\psi}_{\mathrm{det}}(\mathbf{r})$
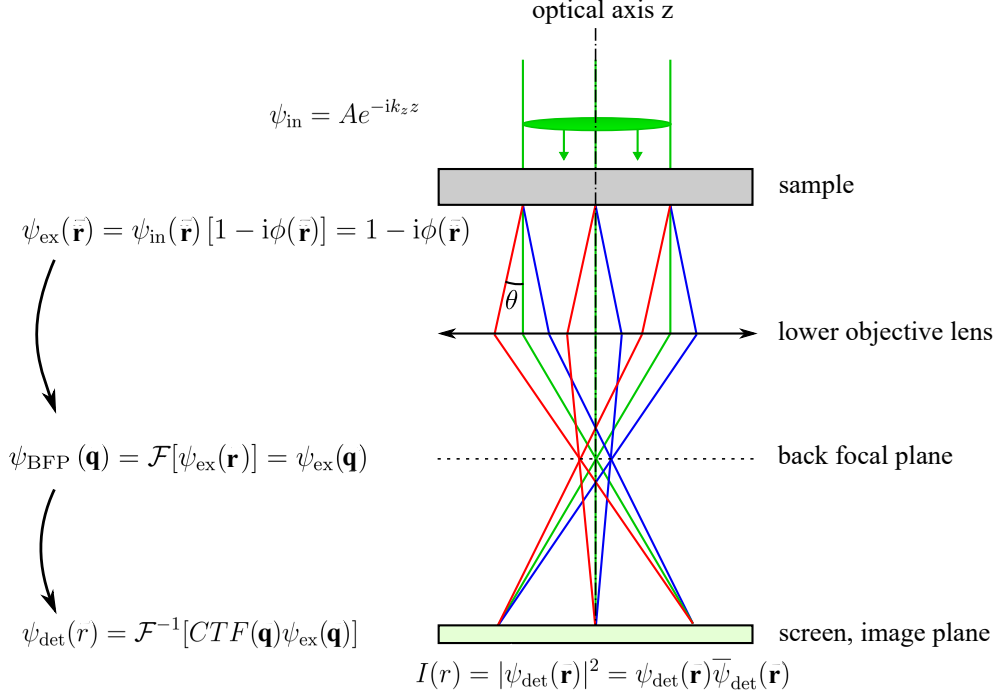
Fig. 1.17: Schematic view of image formation with terms describing an electron wave in the main optical planes shown on the left side.

The CTF describes changes in the electron wave phase introduced by lens aberrations and damping of higher spatial frequencies caused by partial temporal and spatial coherency. The CTF generally depends on 2D position vector in the spatial frequency domain $\mathbf{q}$. For small scattering angle $\theta$, the magnitude of the position vector can be written as follows

$$|\mathbf{q}| = \frac{\theta}{\lambda}, \tag{1.3}$$

where $\lambda$ is the relativistic wavelength of the electron wave. According to [28], the CTF can be written as

$$CTF(\mathbf{q}) = E_{\mathrm{t}}(\mathbf{q})E_{\mathrm{s}}(\mathbf{q})e^{-\mathrm{i}\frac{2\pi}{\lambda}\chi(\mathbf{q})}, \tag{1.4}$$

where $E_{\mathrm{t}}$ and $E_{\mathrm{s}}$ is the temporal and spatial damping envelope function, respectively. $\chi$ is the wave aberration function.

The wave aberration function can be written as a sum of aberration terms, Eq. 1.5 [29]. Each aberration term consists of aberration coefficient $C_{n,m}$ and the spatial frequency $q = |\mathbf{q}|$. The mentioned notation $C_{n,m}$ corresponds to Krivanek's notation in [29], where $n$ denotes the order of aberration and $m$ its symmetry, also called multiplicity.

An aberration coefficient is in general a complex number and thus it can be written as

$$C_{n,m} = C_{n,m,a} + \mathrm{i}C_{n,m,b} = |C_{n,m}|\,\mathrm{e}^{\mathrm{i}\phi_{n,m}} = |C_{n,m}|\left(\cos\phi_{n,m} + \mathrm{i}\sin\phi_{n,m}\right),$$

where $\phi_{\mathrm{n,m}}$ denotes azimuth orientation of the aberration and $|C_{\mathrm{n,m}}| = \sqrt{C_{\mathrm{n,m}}\overline{C}_{\mathrm{n,m}}}$ is the modulus of the complex aberration coefficient $C_{n,m}$. For rotationally symmetric aberrations ($m = 0$), the $\phi_{n,m}$ is taken as $\phi_{n,0} = 0$, thus $C_{n,0} \in \mathbb{R}$. Using summation

over the indices $n$ and $m$, the wave aberration function can be written as follows

$$\chi\left(q,\phi\right) = \sum_n \sum_m \frac{1}{n+1} \cos\left(m\phi - \phi_{n,m}\right) \left|C_{n,m}\right| \lambda^{n+1} q^{n+1},\qquad (1.5)$$

where for even $n$ it is summed over a series of odd $m$'s up to $n+1$, so $m = 1, 3, \ldots, n+1$, and for odd $n$, the summations goes over a series of even $m$'s again up to $n+1$, so $m = 0, 2, \ldots, n+1$. $\phi$ denotes azimuth angle in spatial frequency domain.

Besides electron lens aberrations, the imaging process is strongly influenced by electron beam coherence. The ideal source of the coherent electron beam is infinitely small and has zero energy spread. Such conditions are never met in the practice, which results in the finite highest transferred spatial frequency (i.e. transferred detail). This effect is described by damping envelope exponential functions for both the spatial and temporal coherence.

The temporal incoherence rises from non-zero energy spread of the electron beam. Together with the chromatic aberration of the lens, temporal incoherence leads to the chromatic focus spread $\Delta C_{\mathrm{C}(1,0)}$, which can be described by a simple model as

$$\Delta C_{\mathrm{C}(1,0)} = C_{\mathrm{C}} \sqrt{\left(\frac{\Delta E_{\mathrm{rms}}}{E_{\mathrm{kin}}}\right)^2 + \left(\frac{\Delta U}{U}\right)^2 + 4\left(\frac{\Delta I}{I}\right)^2},$$

where $C_{\mathrm{C}}$ is the chromatic aberration coefficient, $\Delta E_{\mathrm{rms}}$ is the root-mean-square energy spread of the electron beam, $E_{\mathrm{kin}}$ denotes kinetic energy of the incident beam, $\frac{\Delta U}{U}$ is the instability of the acceleration voltage $U$ and $\frac{\Delta I}{I}$ denotes the lens current instability [28]. The envelope function is then given by

$$E_{\mathrm{t}}\left(q\right) = \mathrm{e}^{-\frac{1}{2}\left(\pi\lambda\Delta C_{\mathrm{C}(1,0)} q^2\right)^2}.$$

Spatial incoherence is the consequence of a finite size of the electron source. The incident electron wave can be then decomposed into partial plane electron waves illuminating the sample under angles ranging from 0 to the illumination aperture (beam convergence half-angle) $\alpha$, see Fig. 1.18. Interference of these electron waves which are not spatially coherent results in damping of higher spatial frequencies. For homogeneous intensity distribution of the electron source, this effect can be summarized as

$$E_{\mathrm{s}}(\mathbf{q}) = \mathrm{e}^{-\left(\frac{\pi\alpha}{\lambda}\right)^2 [\nabla\chi(\mathbf{q})]^2}.$$

Assuming a Gaussian distribution would result in multiplying the argument of the exponential function by a constant [6].
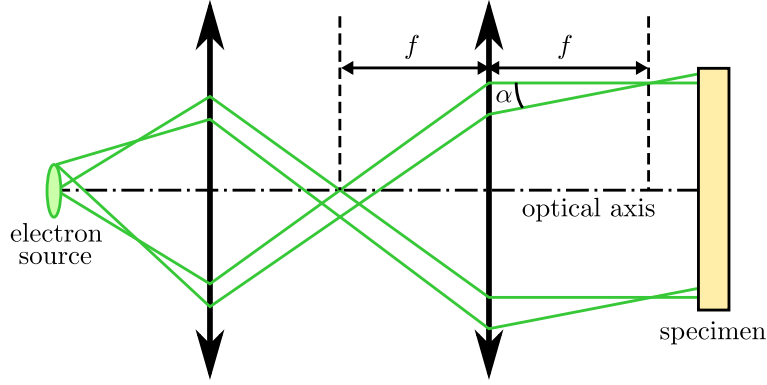
Fig. 1.18: The electron beam convergence half-angle $\alpha$ caused by the finite size of the electron source.

An example of the PCTF function at Scherzer defocus[2], which maximizes the point resolution, is shown in Fig. 1.19. Only two aberration terms were used to create the plots, the defocus term and the spherical aberration term. This yields the following aberration function

$$\chi(q) = \frac{1}{2}C_{1,0}\lambda^2 q^2 + \frac{1}{4}C_{3,0}\lambda^4 q^4, \tag{1.6}$$

where $C_{1,0}$ is the defocus and $C_{3,0}$ is the spherical aberration coefficient.

Denoted in the 1D PCTF plot are the positions of the point resolution and information limit. The point resolution is defined as the point, where the PCTF crosses zero for the first time, and the information limit is the point, where the combined damping envelope function drops down to $\frac{1}{\mathrm{e}^2}$.
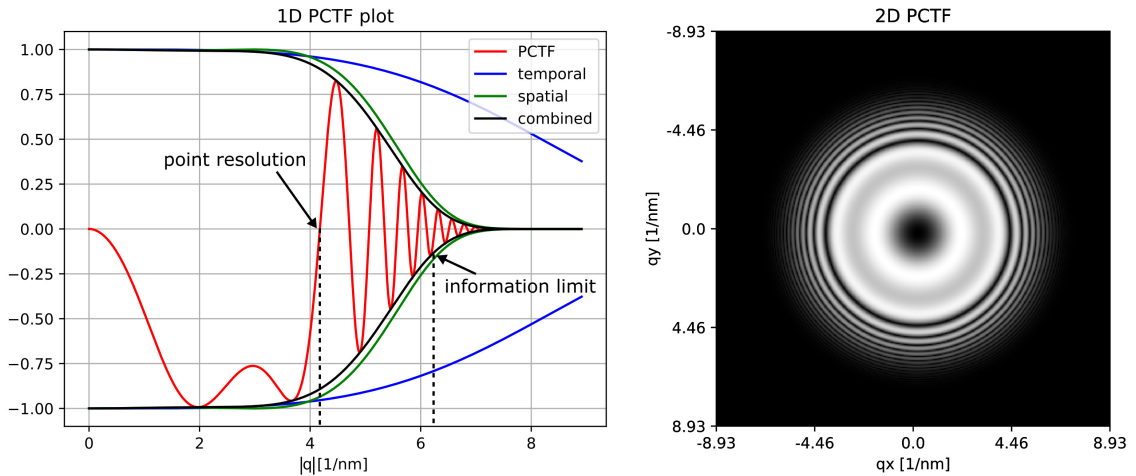


Fig. 1.19: The magnitude of the 2D PCTF at Scherzer defocus on the right and the respective 1D PCTF on the left. Following parameters were used to obtain these graphs: spherical aberration coefficient $C_{3,0} = 1.2\,\mathrm{mm}$, chromatic aberration coefficient $C_\mathrm{C} = 1.2\,\mathrm{mm}$, acceleration voltage $U = 200\,\mathrm{kV}$, root-mean-square energy spread $\Delta E_\mathrm{rms} = 0.7\,\mathrm{eV}$, HT ripple $\Delta U = 0.1\,\mathrm{V}$, lens current stability $\frac{\Delta I}{I} = 0.5\,\mathrm{ppm}$ and illumination aperture $\alpha = 0.3\,\mathrm{mrad}$.

---

[2]Scherzer defocus is defined as $C_{1,0} = -1.2\sqrt{C_{3,0}\lambda}$ [30].

## 1.2.2 TEM Difraction

Diffraction plays an essential role in study of crystalline or polycrystalinne samples. This subchapter highlights the importance of parallel beam electron diffraction. A thorough explanation of kinematical and dynamical theory of electron diffraction is given in [6].

Switching from imaging to the diffraction mode in TEM changes projector lenses excitation so the objective back focal plane is imaged on camera instead of the objective image plane. In case of a monocrystalline sample, the diffraction pattern consists of discrete bright spots, see Fig. 1.16. This is because the incident plane wave is scattered by planes of atoms and the scattered waves interfere. Whether the interference is constructive or destructive depends on whether the waves are in phase. This is determined by the angle $\theta$ between the incident and the scattered wave, see Fig. 1.20. Conditions under which the individual waves are in phase are called the Laue conditions.

A simpler than the von Laue's approach can be used to describe the very essential properties of TEM diffraction. Using trigonometry, it can be shown, that the path difference between two scattered interfering waves $2l$ is

$$l = d_{hkl} \sin\left(\theta\right).$$
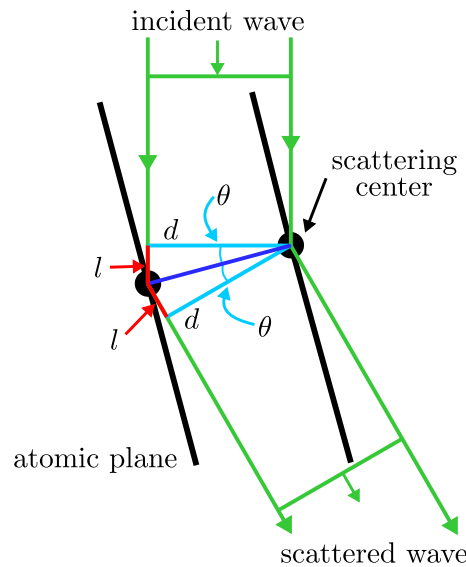


Fig. 1.20: Schematic drawing of the incident wave scattered by two different atomic planes.

The two scattered waves interfere constructively if the path difference is equal to an integer multiple of the wavelength, which yields

$$n\lambda = 2d_{hkl} \sin\left(\theta_{\mathrm{B}}\right), \tag{1.7}$$

where $\lambda$ is the electron wave wavelength, $n$ is an integer referred to as the order of diffraction and $\theta_{\mathrm{B}}$ is the Bragg's angle. The Eq. 1.7 is called the Bragg's law and the scattering angle $\theta$ is called the Bragg's angle $\theta_{\mathrm{B}}$ only if it satisfies the constructive

interference condition. Note that for this simple case of electron diffraction, only elastically scattered electrons are considered and thus the wavelength of the incident wave is equal to the wavelength of the scattered wave.

A distribution of brights spots in a diffraction pattern carries information about the crystallographic structure of the sample. The diffraction spots' distance from the central spot corresponds to the *hkl* plane distance and the order of diffraction. Tilting the sample changes diffraction conditions and therefore the diffraction pattern changes. This is used to orient the crystalline sample for atomic resolution measurements, where the precise orientation of atomic planes is crucial.

**Selected-Area Diffraction**
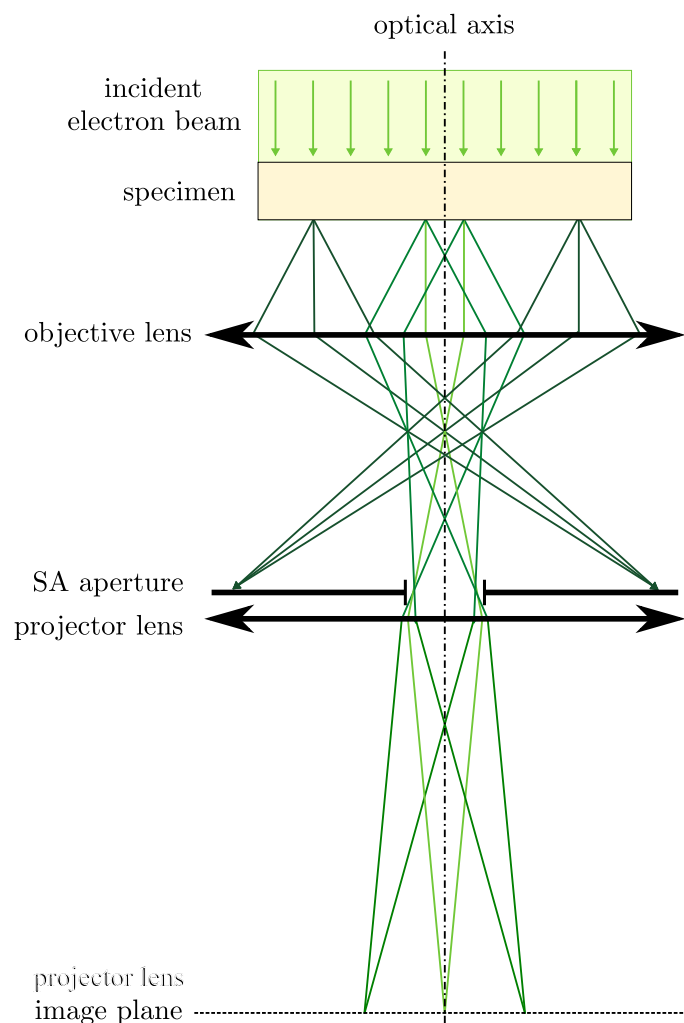


Fig. 1.21: Schematic drawing of selected-area diffraction.

Selected-area (SA) diffraction is a technique which allows to select an area of the sample from which the diffraction pattern is transferred and magnified by the projection system to a camera. This is done by placing a SA aperture in the objective lens' image plane. The desired area is selected in imaging mode and since electrons coming from other parts of the sample are blocked, the diffraction pattern recorded after switching to a

diffraction mode is created purely by the selected area of the sample, as shown in Fig. 1.21. This technique is especially useful when the condenser system is not capable of illuminating a sufficiently small area with a parallel beam.

### 1.2.3   Advanced TEM techniques

**STEM**

In the STEM mode is the specimen scanned point-by-point with a small electron probe. Scattered (DF STEM) or unscattered (BF STEM) electrons are detected from each scanning point to create an image. Typically used probe diameters are of the order of 0.2–5 nm [6]. The incident beam is focused using condensor lenses, the Fig. 1.11 d) shows focusing the beam using C2 lens with condensor mini-lens switched optically off. Modern TEMs can typically utilize both modes, conventional TEM imaging mode (1.2.1) and STEM mode. However, STEM requires additional hardware which enables fast and precise electron beam deflection and a detector (1.1.3) that integrates the signal from each scanning point.

Additional double deflection system is placed above the sample. Unlike deflection coils used for TEM imaging alignments, the STEM deflectors are excited by an alternating current and low inductance coils need to be employed to provide fast magnetic field changes.

STEM can provide images with sub-ångström resolution [31] and it is more straightforward technique, when it comes to image interpretation, than high resolution TEM. It is also frequently combined with X-ray detectors to provide elemental composition data from each scanning point.

**Ultrafast TEM**

Ultrafast TEM is a technique which introduced femtosecond time resolution to TEMs. Ultrafast laser systems are mostly employed to reach timescales beyond those limited by the frame rate of TEM cameras and detectors, although setups which utilize RF cavities also exist [32, 33].

In a typical setup, a femtosecond laser pulses are used to initiate the electron emission and also to excite the sample, as shown in Fig. 1.22. Laser is focused on the emitter and emission conditions can be set so that each laser pulse causes emission of only few electrons or even a single electron. The temporal length of produced electron pulses is thus given by the length of laser pulses.

Laser pulses focused on the sample initiate reversible processes such as phase transitions or atomic structural expansions [34]. The delay between electron pulses and laser pulses arrival to the sample is kept constant during an image acquisition. Millions of femtosecond pulses need to be detected to obtain single micrograph. The delay is changed after each acquisition and the time evolution of the reversible process is mapped.
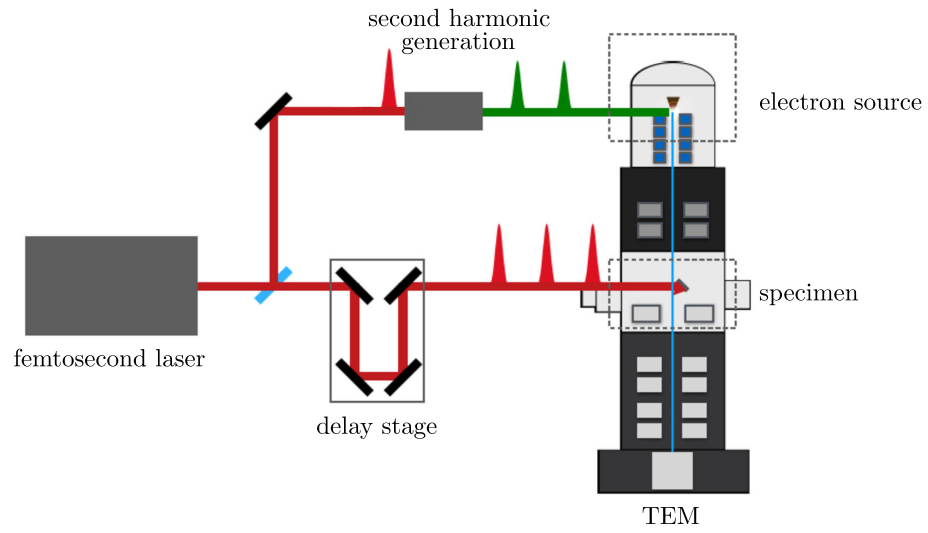
Fig. 1.22: Ultrafast transmission electron microscope setup. Adapted from [32].

# 2.   Optics

## 2.1   Gaussian and Matrix Optics Formalism

Although light optics differs from charged particle optics in many ways, some useful analogies can be found. The derivation of thick lens matrix elements in this subchapter follows [18]. The assumptions mentioned below allow a simplified description of light and charged particle phenomena. In terms of this thesis, Gaussian and matrix optics were used to get more insight into a four lens projection system optical properties, see chapter 4. Gaussian optics is based on the following essential assumptions.

The wavelength is considered to be very small compared to the size of objects with which the light (charged particles) interacts.

The investigated optical systems are symmetrical around the optical axis.

All geometrical rays propagate under small angles against the optical axis.

An important consequence of the first assumption is that Gaussian optics cannot be used to explain optical effects such as interference and diffraction. The second assumption means, that geometrical rays can be described with just two parameters for a given position along the optical axis: a radial distance from the optical axis $x(z)$ and an angle against it $x'(z) = \frac{dx}{dz}$. The last of the assumptions is called the paraxial approximation. Sine and tangent functions can be then expressed as linear functions of the angle and cosine is considered to be equal to 1, i.e. $\sin x' \approx x'$, $\tan x' \approx x'$ and $\cos x' \approx 1$.

Gaussian optics allows to describe the effect of optical elements such as lenses and mirrors on the coordinates $x$ and $x'$ with $2 \times 2$ (so called ABCD) matrices. This is especially useful for systems composed of multiple optical elements, since the effect on the rays is given by a single matrix which is created by multiplication of corresponding individual element and transfer matrices. It is important to note that any wave effects and nonlinearities are neglected in Gaussian optics. Thus phenomena like optical aberrations, diffraction or interference cannot be described. The simplest case is propagation of a charged particle in the field-free region as shown in Fig. 2.1.
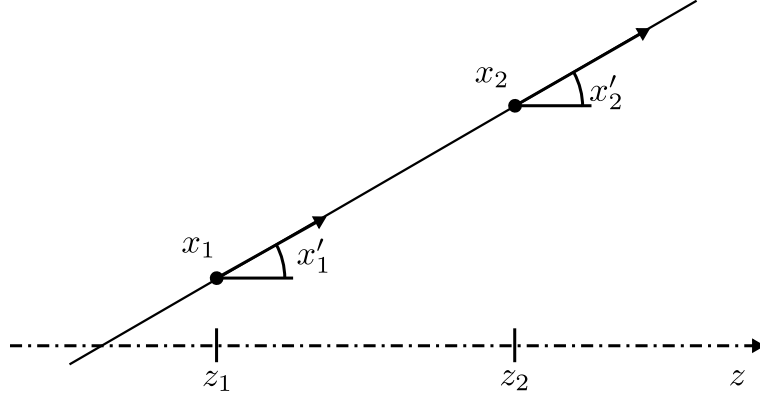
Fig. 2.1: Propagation of a ray in a field-free region from $z_1$ to $z_2$ position.

Following equations show the transformation of initial coordinates $x_1, x_1'$ due to ray propagation

$$
\begin{aligned}
x_2 &= Ax_1 + Bx_1' = x_1 + x_1'(z_2 - z_1) \\
x_2' &= Cx_1 + Dx_1' = x_1' \qquad .
\end{aligned}
\tag{2.1}
$$

Hence the transfer matrix is

$$
\mathbf{T} = \begin{pmatrix} 1 & |z_2 - z_1| \\ 0 & 1 \end{pmatrix} = \begin{pmatrix} 1 & d \\ 0 & 1 \end{pmatrix},
\tag{2.2}
$$

where $d$ is the distance along the optical axis between the two points.

Gaussian optics allows the definition of two pairs of cardinal planes for a focal optical system. These planes are the focal planes and the principal planes. All the cardinal planes are perpendicular to the optical axis and the intersection points are called the cardinal points. Since there is one more pair of cardinal points, which have no corresponding cardinal plane (nodal points), there is in total 6 cardinal points, which determine the optical properties of the focal system. As will be shown later, cardinal planes can be used to determine the imaging properties of the optical system.

The image focal plane $z_{\mathrm{Fi}}$ (also called back focal plane) is defined in the following way: an image of an infinitely far object is formed at the back focal plane of the optical system, see Fig. 2.2. This means that parallel rays entering the optical system pass through the same point at the back focal plane of the optical system. When the rays are parallel to the optical axis then this point is located on the optical axis and is called the image focal point (also called back focal point). If an object is put at the front focal plane $z_{\mathrm{Fo}}$, an image is created infinitely far from the optical system. This means that any ray which goes through the front focal point is transformed by the optical system to be parallel with the optical axis, see Fig. 2.3.
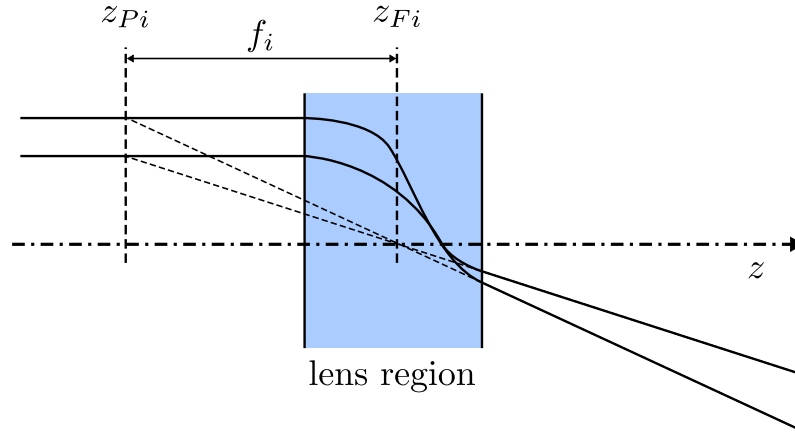
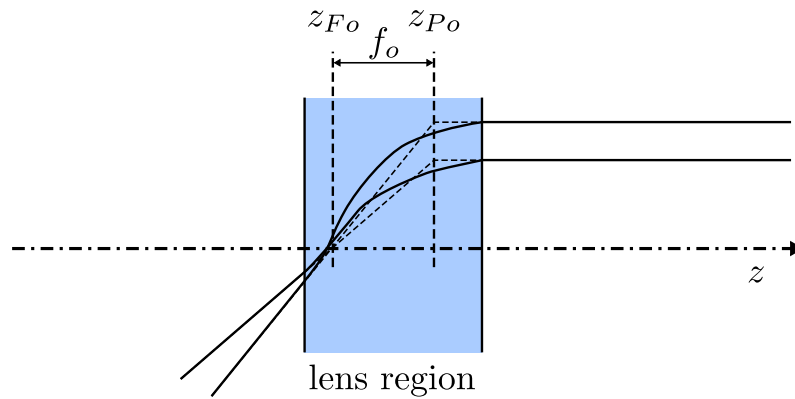Fig. 2.2: The asymptotic construction of the image focal plane $z_{\mathrm{Fi}}$ and the image principal plane $z_{\mathrm{Pi}}$. Adapted from [18].



Fig. 2.3: The asymptotic construction of the object focal plane $z_{\mathrm{Fo}}$ and the object principal plane $z_{\mathrm{Po}}$. Adapted from [18].

The principle planes $z_{\mathrm{Pi}}$ and $z_{\mathrm{Po}}$ are constructed by extrapolating incoming and outgoing rays as illustrated in the Fig. 2.2 and 2.3. The linear magnification between principle planes is 1 and the distance between corresponding principle and focal points is the focal length of the system.

The ray incident under an arbitrary angle to the front nodal point emerges from the optical system under the same angle. In other words the angular magnification between nodal points is 1. The construction which uses extrapolation of incoming and outgoing ray is shown in the Fig. 2.4.
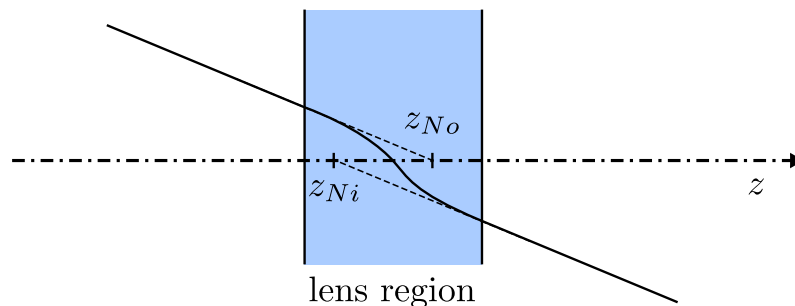


Fig. 2.4: The asymptotic construction of nodal points $z_{\mathrm{No}}$ and $z_{\mathrm{Ni}}$. Adapted from [18].

Using the definition of focal planes, two rays $r_a(z)$ and $r_b(z)$ which satisfy boundary condtitions 2.3,

$$\lim_{z \to -\infty} r_a(z) = 1, \quad \lim_{z \to \infty} r_b(z) = 1 \qquad (2.3)$$

can be defined. It is possible to express an arbitrary ray $x(z)$ as a linear combination of $r_a(z)$ and $r_b(z)$,

$$x(z) = A r_a(z) + B r_b(z), \qquad (2.4)$$

where $A$ and $B$ are constants. Using eq. 2.4 the incident and emergent asymptotes of a general ray can be expressed

$$\lim_{z \to -\infty} x(z) = A + \frac{z - z_{\mathrm{Fo}}}{f_o} B$$

$$\lim_{z \to \infty} x(z) = -\frac{z - z_{\mathrm{Fi}}}{f_i} A + B.$$

By eliminating $A$ and $B$ the transfer matrix of a focal optical system is obtained

$$\mathbf{L} = \begin{pmatrix} -\frac{z_2 - z_{\mathrm{Fi}}}{f_i} & f_o + \frac{(z_1 - z_{\mathrm{Fo}})(z_2 - z_{\mathrm{Fi}})}{f_i} \\ -\frac{1}{f_i} & \frac{z_1 - z_{\mathrm{Fo}}}{f_i} \end{pmatrix}, \qquad (2.5)$$

where $z_1$ and $z_2$ are, respectively, the position on the optical axis related to the incident asymptote $\mathbf{x_1}(z_1) = \begin{pmatrix} x_1 \\ x_1' \end{pmatrix}$ and the position related to the emergent asymptote $\mathbf{x_2}(z_2) = \begin{pmatrix} x_2 \\ x_2' \end{pmatrix}$.

Using the $\mathbf{L}$ matrix, it is easy to derive all the imaging relations. If planes $P_{\mathrm{o}}(z_1 = z_{\mathrm{o}})$ and $P_{\mathrm{i}}(z_2 = z_{\mathrm{i}})$ are conjugate, then all rays coming from any point in $P_{\mathrm{o}}$ converge to a point in $P_{\mathrm{i}}$ and thus $x_{\mathrm{i}}(z_{\mathrm{i}})$ has to be independent of $x_{\mathrm{o}}'(z_{\mathrm{o}})$. This yields

$$f_{\mathrm{o}} + \frac{(z_{\mathrm{o}} - z_{\mathrm{Fo}})(z_{\mathrm{i}} - z_{\mathrm{Fi}})}{f_{\mathrm{i}}} = 0$$

and

$$\begin{pmatrix} x_{\mathrm{i}} \\ x_{\mathrm{i}}' \end{pmatrix} = \begin{pmatrix} -\frac{z_2 - z_{\mathrm{Fi}}}{f_{\mathrm{i}}} & 0 \\ -\frac{1}{f_{\mathrm{i}}} & \frac{z_1 - z_{\mathrm{Fo}}}{f_{\mathrm{i}}} \end{pmatrix} \begin{pmatrix} x_{\mathrm{o}} \\ x_{\mathrm{o}}' \end{pmatrix}.$$

Further it can be shown that the transverse magnification M is given by

$$M = \frac{x_{\mathrm{i}}}{x_{\mathrm{o}}} = -\frac{z_2 - z_{\mathrm{Fi}}}{f_{\mathrm{i}}}. \qquad (2.6)$$

In case of $x_{\mathrm{o}} = 0$, the angular magnification $M_\alpha$ is given by the ration $\frac{x_{\mathrm{i}}'}{x_{\mathrm{o}}'}$ and hence

$$M_\alpha = \frac{z_1 - z_{\mathrm{Fo}}}{f_{\mathrm{i}}}. \qquad (2.7)$$

The often used simplified theoretical concept of the focal optical system is a thin lens. Its transfer matrix can be obtained from Eq. 2.5 by setting the origin of the

coordinate system midway between $z_{\mathrm{Fo}}$ and $z_{\mathrm{Fi}}$, so that

$$-z_{\mathrm{Fo}} = z_{\mathrm{Fi}} = z_{\mathrm{F}} > 0.$$

In the concept of thin lens, both principle and nodal points coincide at the position of thin lens, which means that

$$z_{\mathrm{F}} = f.$$

In the plane of the lens, $z_1 = z_2 = 0$ the transfer matrix is

$$\mathbf{L} = \begin{pmatrix} 1 & 0 \\ -\frac{1}{f} & 1 \end{pmatrix}. \tag{2.8}$$

Multiplying the thin lens matrix (Eq. 2.8) with two transfer matrices (Eq. 2.2) in appropriate order yields

$$\mathbf{A} = \mathbf{T}_2\mathbf{L}\mathbf{T}_1 = \begin{pmatrix} 1 - \frac{d_2}{f} & d_1 + d_2 - \frac{d_1 d_2}{f} \\ -\frac{1}{f} & 1 - \frac{d_1}{f} \end{pmatrix}.$$

If $d_1$ and $d_2$ are distances of the conjugate planes from the thin lens, then $\mathbf{A}_{1,2} = 0$ and the thin lens equation can obtained

$$\frac{1}{d_{\mathrm{o}}} + \frac{1}{d_{\mathrm{i}}} = \frac{1}{f}, \tag{2.9}$$

where $d_{\mathrm{o}} = d_1$ is the object distance and $d_{\mathrm{i}} = d_2$ is the image distance. The transverse magnification is given by $\mathbf{A}_{1,1}$ and thus

$$M = 1 - \frac{d_{\mathrm{i}}}{f} \tag{2.10}$$

.

## 2.2 Derivation of Trajectory Equation

The idea behind the derivation of the trajectory equation is to describe a path of a charged particle in a stationary electromagnetic field using only coordinates by substituting for time-dependent variables in the equation of motion. However, before deriving any terms it is convenient to first define the accelerating potential after the relativistic correction

$$\Phi^* = \Phi\left(1 + \varepsilon\Phi\right).$$

$\Phi$ is the accelerating potential before relativistic correction and $\varepsilon = \frac{e}{2m_0 c^2}$, where $e = |q|$ is the elementary charge, $m_0$ is the rest mass of the particle and $c$ the speed of light. Using this relativistic correction, the magnitude of velocity of an accelerated charged

particle can be written as follows

$$v = \frac{1}{\gamma}\sqrt{\frac{2e\Phi^*}{m_0}} = \frac{1}{1+2\varepsilon\Phi}\sqrt{\frac{2e\Phi^*}{m_0}}, \tag{2.11}$$

where $\gamma = \frac{1}{\sqrt{1-\frac{v^2}{c^2}}} = 1 + 2\varepsilon\Phi$ denotes the Lorentz factor.

The force $\mathbf{F}$ acting on a charged particle of the electric charge $q$ in the electric field $\mathbf{E}$ and the magnetic field $\mathbf{B}$ is given by the Lorentz law

$$\mathbf{F} = q(\mathbf{E} + \mathbf{v} \times \mathbf{B}), \tag{2.12}$$

where $\mathbf{v}$ is the particle's velocity. Using the Newton's second law and the relativistic mass formula, the particle's equation of motion is obtained

$$m_0\frac{d}{dt}(\gamma\mathbf{v}) = q(\mathbf{E} + \mathbf{v} \times \mathbf{B}), \tag{2.13}$$

where $\gamma = \frac{1}{\sqrt{1-\frac{v^2}{c^2}}}$ is the Lorentz factor. In the following steps it is assumed that the particle is an electron, thus $q = -e$ and that the electron is moving in the positive $z$-direction, $v_z > 0$. The next step is to parametrize motion of the electron using the $z$ coordinate, $(x(z(t)), y(z(t)), z(t))$. Time derivation can then be expressed as

$$\frac{d}{dt} = \frac{dz}{dt}\frac{d}{dz} = \dot{z}\frac{d}{dz}. \tag{2.14}$$

Using 2.14 and the definition of a vector magnitude, it is possible to write the magnitude of the velocity as

$$v = \sqrt{\dot{x}^2 + \dot{y}^2 + \dot{z}^2} = \dot{z}\sqrt{\left(\frac{dx}{dz}\right)^2 + \left(\frac{dy}{dz}\right)^2 + 1}.$$

By putting this equation together with the equation 2.11 following expression for $\dot{z}$ can be obtained

$$\dot{z} = \frac{1}{\gamma}\sqrt{\frac{2e\Phi^*}{m_0}}\frac{1}{\sqrt{\left(\frac{dx}{dz}\right)^2 + \left(\frac{dy}{dz}\right)^2 + 1}}.$$

In order to keep the form of the derived terms simpler, complex coordinates are defined as follows

$$w(z) = x(z) + \mathrm{i}y(z) = r(z)\mathrm{e}^{\mathrm{i}\theta(z)}$$
$$E_w(z) = E_x(z) + \mathrm{i}E_y(z)$$
$$B_w(z) = B_x(z) + \mathrm{i}B_y(z).$$

In this coordinate system, $\dot{z}$ is given by

$$\dot{z} = \frac{1}{\gamma}\sqrt{\frac{2e\Phi^*}{m_0}}\frac{1}{\sqrt{\left(\frac{d\omega}{dz}\right)\left(\frac{d\overline{\omega}}{dz}\right)+1}} = \frac{1}{\gamma}\sqrt{\frac{2e\Phi^*}{m_0}}\frac{1}{\sqrt{\omega'\overline{\omega}'+1}}. \tag{2.15}$$

For this complex coordinate system it can be shown that the components of the vector product $(C_\omega, C_{\overline{\omega}}, C_z) = \mathbf{C} = \mathbf{A} \times \mathbf{B}$ are

$$C_\omega = \mathrm{i}\left(A_z B_\omega - A_\omega B_z\right)$$
$$C_{\overline{\omega}} = -\mathrm{i}\left(A_z B_\omega - A_\omega B_z\right)$$
$$C_z = \frac{\mathrm{i}}{2}\left(A_\omega B_{\overline{\omega}} - A_{\overline{\omega}} B_\omega\right)$$

and $\omega$-component of the equation of motion 2.13 can be then written as

$$\frac{d}{dt}\left(\gamma m_0 \dot{\omega}\right) = -e\left[E_\omega + \mathrm{i}\left(\dot{z}B_\omega - \dot{\omega}B_z\right)\right].$$

In the final step the substitution for the last time-dependent variable $\dot{\omega}$ is done using relation $\dot{\omega} = \dot{z}\omega'$ (see 2.14) and substituting for $\dot{z}$ from 2.15 afterwards. The equation of trajectory is then written in the following form

$$\frac{d}{dz}\left[\left(\frac{\Phi^*}{1+w'\overline{w}'}\right)^{\frac{1}{2}}w'\right] = -\frac{1}{2}E_w\gamma\left(\frac{1+w'\overline{w}'}{\Phi^*}\right)^{\frac{1}{2}} - \mathrm{i}\eta\left(B_w - w'B_z\right), \tag{2.16}$$

where $\eta = \sqrt{\frac{e}{2m_0}}$.

## 2.3  Paraxial Approximation

The $E_w$, $B_w$ and $B_z$ fields in Eq. 2.16 are rarely time-dependent and thus can be considered stationary. Aiming for rotationally symmetric systems and following [18], this electrostatic and magnetostatic fields can be represented by azimuthal Fourier series expansion. Neglecting quadratic and higher-order components in $w$, $\overline{w}$ and their derivatives, the Eq. 2.16 becomes

$$w'' + \left(\frac{\gamma\phi'}{2\Phi^*} - \mathrm{i}\frac{\eta B}{\sqrt{\Phi^*}}\right)w' + \left(\frac{\gamma\phi''}{4\Phi^*} - \mathrm{i}\frac{\eta B'}{2\sqrt{\Phi^*}}\right)w = 0, \tag{2.17}$$

where $\phi$ is the axial electrostatic field and $B$ is the axial magnetic field.

In case of magnetic lenses, there is no electrostatic field present and Eq. 2.17 can be thus written as

$$w'' - \mathrm{i}\frac{\eta B}{\sqrt{\Phi^*}}w' - \mathrm{i}\frac{\eta B'}{2\sqrt{\Phi^*}}w = 0. \tag{2.18}$$

As shown in [18], the 2.18 can be transformed to

$$u'' + \frac{\eta^2 B^2}{4\Phi^*}u = 0, \qquad (2.19)$$

where $u$ is the new coordinate, such that $w = ue^{i\theta(z)}$. Neglecting higher order terms means, that the paraxial approximation is accurate only for particles traveling near the optical axis. It allows to describe properties of optical elements using several characteristic quantities and simple relations as shown in 2.1.

## 2.4   Aberrations of Round Magnetic Lenses

Including higher order terms of field expansion to 2.19 results in deviations from the linear behavior of magnetic lenses. These perturbations are called geometrical aberrations, which are the measure of deviation from linear properties and are characterized by geometrical aberration coefficients [35].

Magnetic lenses' sensitivity to charged particle energy causes other deviations from linear behavior. These are the chromatic aberrations, which are characterized by chromatic aberration coefficients.

The last type of aberrations described in this thesis are the parasitic aberrations. Parasitic aberrations rise typically from limited manufacturing precision or lens material inhomogeneities [19, 35]. Parasitic aberrations can also be characterized by aberration coefficients, although their numeric values are not often encountered, since they are different for each individual lens and may change in time [35].

### 2.4.1   Geometric Aberrations

Discussed below are the third-order geometric aberrations, which are obtained by including terms up to third order in $w$, $\overline{w}$ and their derivatives, in Eq. 2.19. These and higher order terms, together with aberration coefficient integrals exceed the scope of this thesis and can be found in [18].

**Spherical Aberration**

Spherical aberration is the most important aberration in TEM, which limits its resolution in both TEM and STEM mode. It is the only aberration from third order geometric aberrations which negatively affects imaging even when the object is located on the optical axis. Spherical aberration is caused by the increasing lens focusing power with increasing distance from the optical axis, as indicated in Fig. 2.5. Thus it is very important to keep the spherical aberration of objective lens low by a thoughtful design, because angles of the rays in the vicinity the objective may be relatively steeply inclined against the optical axis. Although the area of interest increases as the image is magnified by the projector lenses, the involved angles are proportionally lower and hence spherical aberration is not so important for a projection system [35].

In 1936, Otto Scherzer proved that it is impossible to construct a space-charge free static round lens which would have a negative spherical aberration coefficient, this is known as the Scherzer's theorem [30].
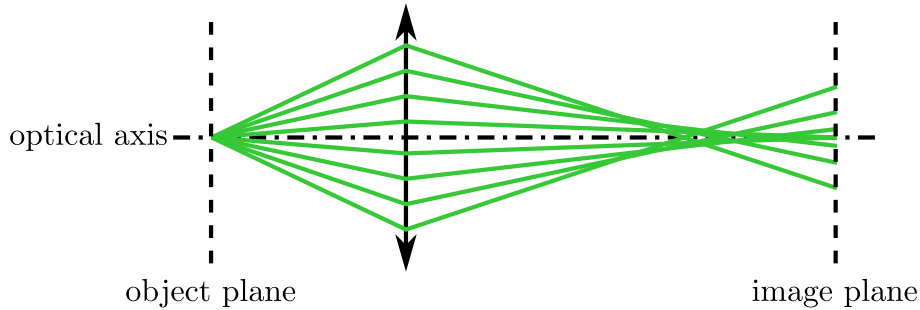


Fig. 2.5: Third order spherical aberration causes, that rays traveling further from the optical axis are focus more strongly than the paraxial ones.


**Coma**

For objective lenses the coma is usually the second most serious geometric aberration after the spherical aberration [18]. The third order coma causes that imaged off-axis points appear to have a comet-like tail, as shown in Fig. 2.6. It often caused by the inclination of the electron against the optical axis of the lens.
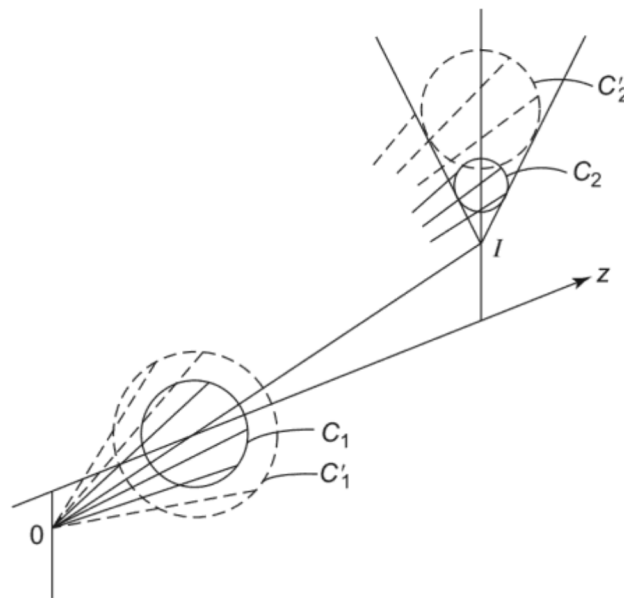


Fig. 2.6: Coma aberration ray diagram, which shows the typical comet like shape. From [18].


**Astigmatism and Field Curvature**

Astigmatism and field curvature do not typically play an important role in TEM or STEM imaging [18]. These aberrations are related to one another and both produce a circle at the Gaussian image plane. However, in case of field curvature, stigmatic

image points are located on a rotationally symmetric paraboloid and in case of astigmatism, the circle changes to an ellipse, which varies significantly in the vicinity of the Gaussian image plane [36]. The third-order astigmatism is sometimes called the Seidel astigmatism or the field astigmatism to distinguish it from the parasitic astigmatism [18, 36].

Fig. 2.7 shows typical aberration figures of astigmatism on the left and field curvature on the right.
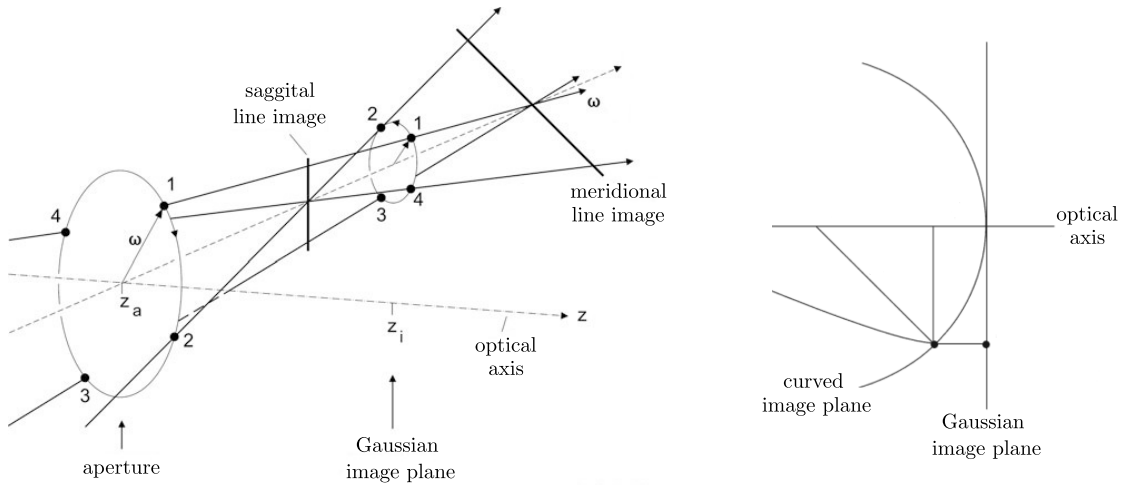


Fig. 2.7: The aberration figure of the astigmatism from [36] on the left and a curved image plane typical for the field curvature from [18] on the right.

## Distortion

Distortion aberration is more important for lenses through which the rays travel relatively far from the optical axis at the object plane. Hence it is usually the dominant geometric aberration of projector lenses. Fortunately it can be minimized by a careful design of the projection system [18].

The distortion is composed of two parts, the radial or isotropic distortion and the azimuthal or anisotropic distortion [36]. Neither the radial nor the isotropic distortion cause image blurring, but both affect the proportionality between image and object coordinates [18], as indicated in Fig 2.8.
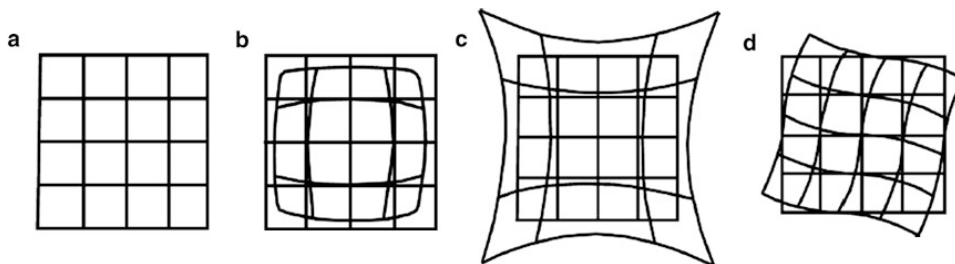


Fig. 2.8: Undistorted image is shown in a) and barrel, pincushion and azimuthal distortion is shown in b), c) and d) respectively. Adapted from [36]

## 2.4.2 Chromatic Aberrations

Unfortunately, a source of ideally monochromatic particle beam does not exist and the voltage and current supplies of the accelerator and the lenses are not perfectly stable. In TEM is the energy spread often further worsen by inelastic interactions with the specimen. Since the lens strength depends on the particle's energy, its effect on particles with different energies varies, which results in image blurring. Similar negative effect may also be caused by the fluctuations of the lens driving current..

There are two kinds of chromatic aberrations, axial aberration and distortion, which consists, analogically to the geometric distortion, from the radial and azimuthal part [36]. The axial chromatic aberration is characterized by a chromatic aberration coefficient. Analogically to the spherical aberration coefficient, the chromatic aberration coefficient is always positive for a space-charge free static round lens [18]. A ray diagram of axial chromatic aberration is shown in Fig. 2.9. If the energy spread of the particle beam is sufficiently lowered (sub-20 meV have been reported [37]), chromatic aberrations of higher orders must be taken into account [36].
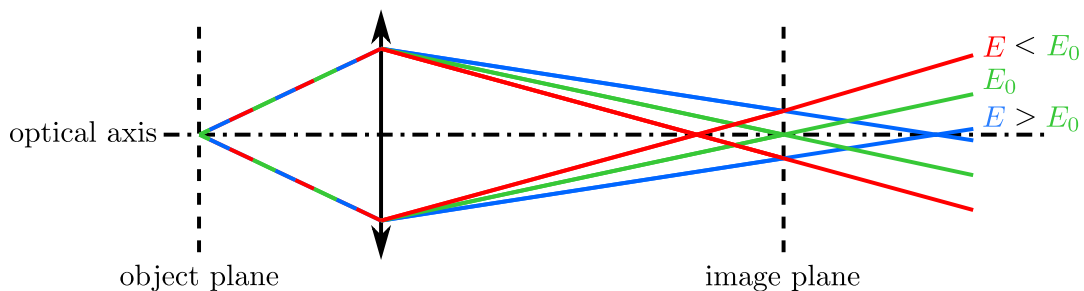


Fig. 2.9: Ray diagram of the axial chromatic aberration. Lower is the electron energy, more strongly it is focused.

## 2.4.3 Parasitic Aberrations

Parasitic aberrations are the consequence of various forms of lens manufacturing imperfections. In TEM, the twofold axial astigmatism is the most often encountered parasitic aberration. It is caused by an elliptical deviation from rotational symmetry of the lens polepieces [19].

In general, any deviations from rotational symmetry generate weak multipole fields of different orders. This leads to deviations from paraxial behaviour, which can be characterized by aberration coefficients. Extensive studies done by Uhlemann and Haider, Krivanek et al., Sawada and other researchers. Unfortunately, they often do not use the same notation and thus extra care should be taken when referring to parasitic aberration coefficients [18].

# 3.   Single Particle Analysis

The dominant technique used to obtain high resolution structural data of biological molecules is X-ray crystallography. Until recently, the X-ray crystallography and nuclear magnetic resonance (NMR) spectroscopy were the only techniques which significantly contributed to the protein data bank. As can be seen from Fig. 3.1, cryo-electron microscopy (cryo-EM) revolution caused, that electron microscopy techniques gained much more importance in last few years.
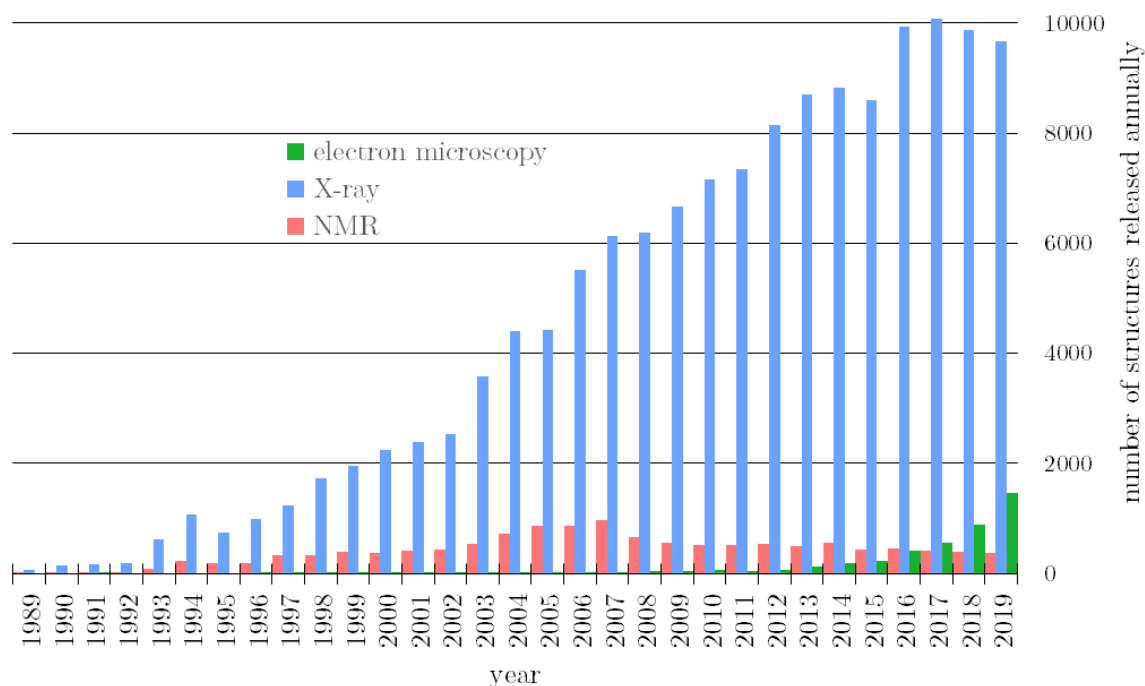


Fig. 3.1: Number of new entries to the protein data bank per year. Data from [38].

There are three main electron microscopy techniques used to study biological molecules and assemblies, electron cryo-crystallography, cryo-electron tomography (CET) and single particle analysis (SPA). Unlike CET and SPA, electron cryo-crystallography cannot be used to study individual and randomly oriented structures. In contrast to CET [39], which reconstructs the structure from tilt-series[1] of images of single or a low number of identical biological assemblies, SPA uses multiple views of a large number of identical randomly oriented biological assemblies to gain information about its structure. The following selected articles document recent advances in SPA [2, 3, 4, 5].

---

[1]Images are recorded by incrementally varying the orientation of the sample relative to the incident beam [39].

## 3.1  Sample Preparation

The cryo-EM sample preparation step of utmost importance is the sample vitrification. A biomolecule solution is first transferred to a holey or lacey carbon grid (see Fig. 3.2) using a pipette. The grid is then blotted nearly dry and immediately after blotting it is rapidly immersed usually in liquid ethane. High cooling rate prevents the remaining water from forming crystalline ice and ensures that water freezes in amorphous phase, which keeps the biomolecules in state close to the initial state [40]. To gain maximal control over the key blot parameters, the vitrification process is semiautomated (see Fig. 3.3), which highly improves sample preparation repeatability.

A liquid of temperature lower than $\approx -160\,°\mathrm{C}$ and sufficient heat capacity is needed to ensure amorphous (vitreous) ice forming. Although the temperature of liquid nitrogen is lower than required $-160\,°\mathrm{C}$, its low heat capacity causes, that it starts to evaporate immediately after contact with a room temperature sample, which lowers the cooling rate. Liquid nitrogen is thus not used to vitrify the sample, but only to cool down the liquid ethane or propane [41], which both have higher heat capacity, and also to transfer and store vitrified samples.

The next step is to transfer the sample to the microscope. In order to prevent contamination growth and ice phase changes, the sample is submerged in liquid nitrogen during transfer and manipulation and its exposure to air is kept at minimum. Vitrified samples are loaded to a cartridge which is then loaded into a transfer capsule. The transfer capsule is docked to a microscope, which automatically loads the samples.
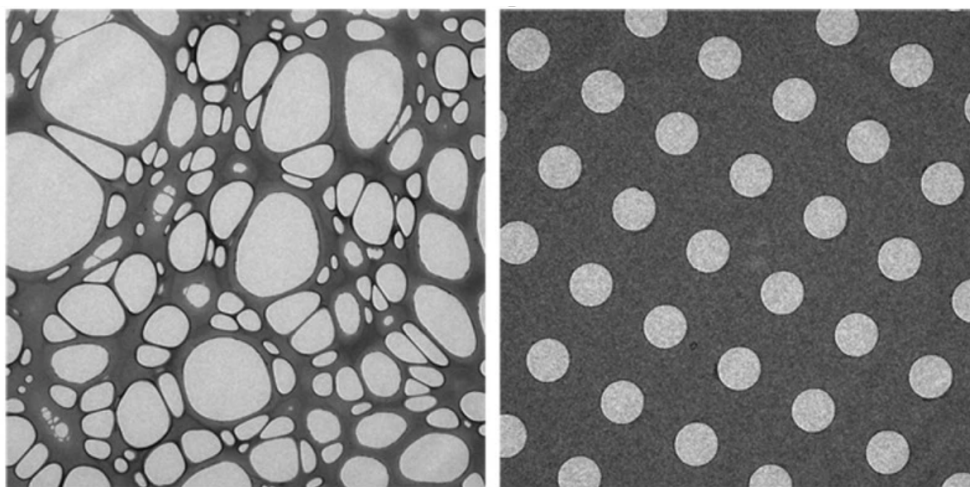


Fig. 3.2: A TEM micrograph of the lacey carbon on the left and the holey carbon on the right. From [42].
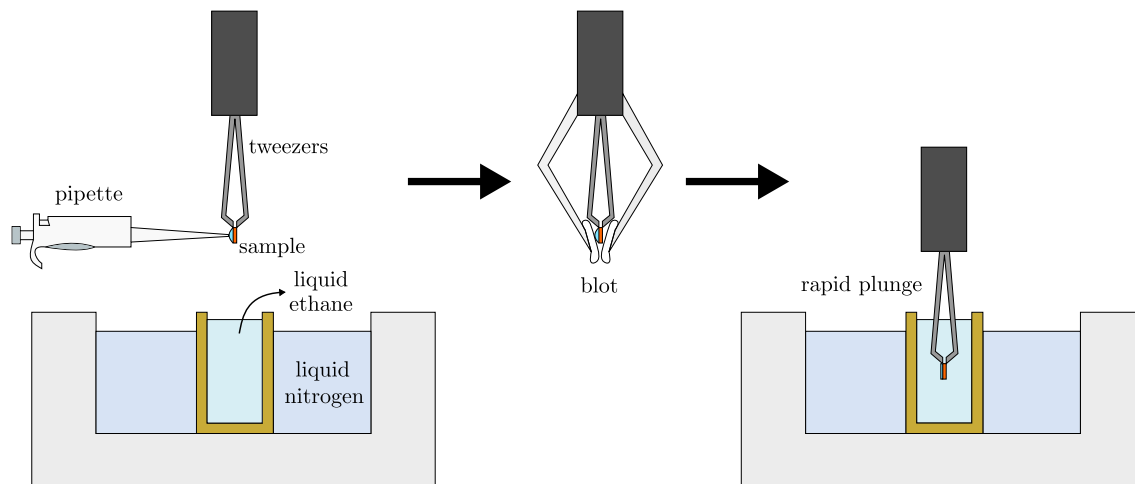
Fig. 3.3: Sample vitrification process. Biomolecules are transferred to a TEM grid in form of a solution using pipette. The sample is then blotted and plunged to the reservoir with liquid ethane. The liquid ethane reservoir is cooled by the liquid nitrogen.

## 3.2 Sample Screening and Data Acquisition

In order to limit the sample exposure to electron beam, a calibration specimen is typically used to pre-align the microscope. Despite of best efforts during sample preparation are some sample areas useless for data acquisition. Thus samples are usually checked (screened) prior to high resolution acquisition. The whole sample is mapped in low magnification and acquired images are then investigated. It is important to check, whether the ice is amorphous or crystalline, and also the ice thickness needs to be checked, since too thick ice means high electron absorption and scattering which results in low signal. Fig. 3.4 shows a sample map created by stitching multiple low magnification images together. Defocused images are typically captured to show Bragg diffraction spots in case of crystalline ice as shown in Fig. 3.4 on the right.

After identifying usable areas, the next step is to start data acquisition. High resolution images of selected areas are then automatically recorded using loaded microscope presets. An example of a high resolution micrograph, Fig. 3.5, shows streptavidin protein. Since hundreds or thousands of micrographs are needed for single particle reconstruction, this process takes usually hours to complete. The frequently used scenario thus employs two TEMs. The samples are screened using TEM with high sample throughput and then are the selected high quality samples moved to image corrected TEM for data acquisition.

Very low total electron doses, typically tens of electrons per ångström squared, are used for data acquisition to prevent beam induced sample damage and that is why an ultra sensitive camera is needed [3]. The role of a camera can be described in terms of phase contrast theory (1.2.1) by adding a damping envelope function and modulating the signal with modulation transfer function of recording device [7, 28]. Recent developments in direct electron detection had major contribution to what is often referred as cryo-EM revolution [43, 44].
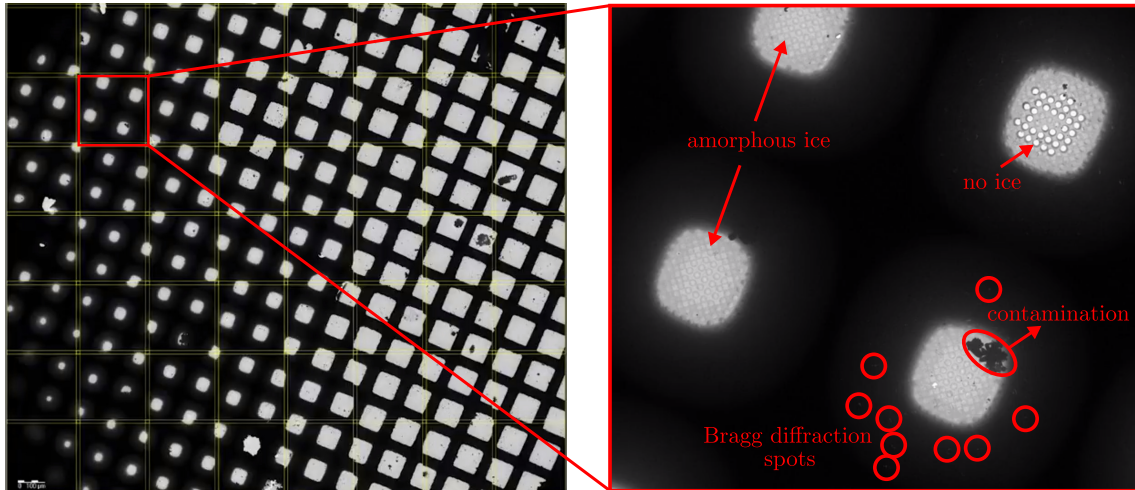
Fig. 3.4: A map of vitrified is shown on the left and its detail on the right.
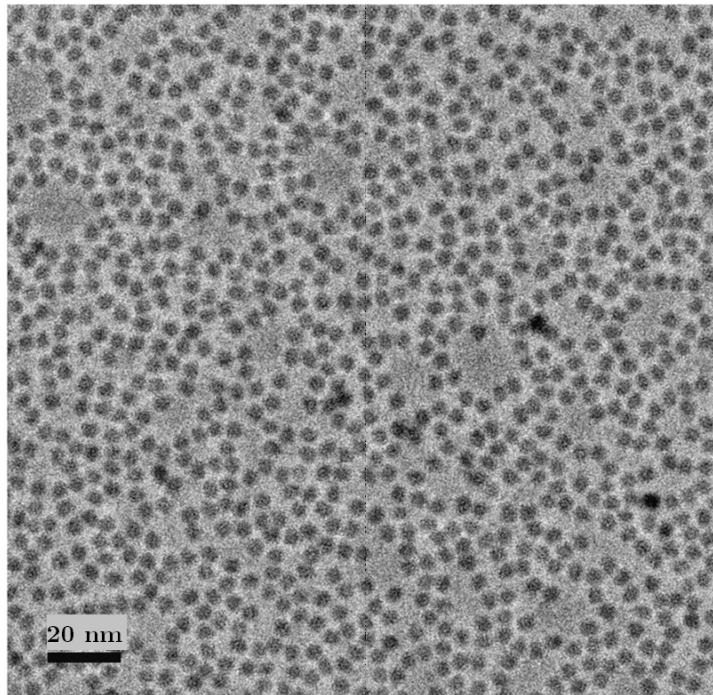


Fig. 3.5: Example micrograph of vitrified streptavidin from [3].

## 3.3 Single Particle Reconstruction

Each captured micrograph may contain hundreds or thousands of identical particles in different orientations. The goal of the single particle reconstruction is to determine 3D structure of the studied particle. The reconstruction process is complicated by the fact, that the studied biomolecules might exist in multiple conformations and that large biological assemblies are flexible.

Multiple images of the same sample area are typically captured and then averaged to obtain better signal-to-noise ratio [39]. However, the electron beam induces a local sample motion which needs to be corrected during micrograph post-process. Motion-

corrected and averaged micrographs are then analyzed and the CTF parameters are estimated for each averaged micrograph [45, 46]. The next step, after a CTF correction using found parameters, is to identify the positions of suitable individual particles in the micrographs. This task can be semi-automated and an extra care should be taken when selecting the autopicking thresholds and choosing the template particles. Possible risks are demonstrated in [47].

After filtering out the possible false positive autopicks, the next step is to computationally classify different conformational states. An according initial 3D model is then linked to obtained 2D projections and iteratively refined to a high resolution 3D structure. Reconstructed 3D structure must of course obey the chemical constrains on bonding and stereochemistry [44]. There are multiple software programs which utilize different algorithms and approaches and the description above gives just a general idea about the single particle reconstruction workflow, Fig. 3.6. It is important get good understanding of the workflow for the particular software to gain as much information about the structure as possible.
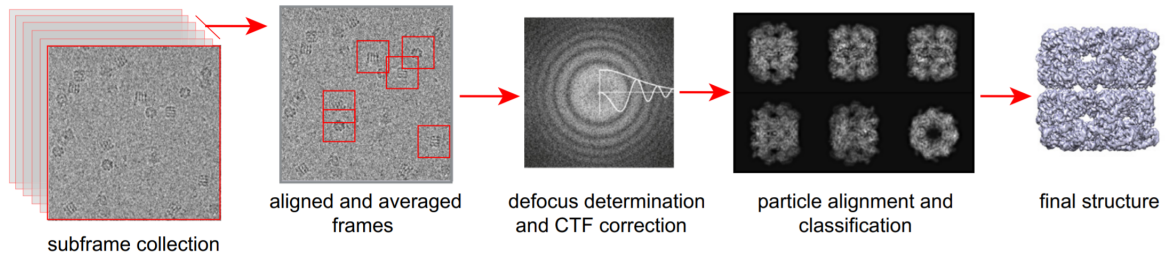


Fig. 3.6: Single particle reconstruction workflow. Adapted from [48].

# 4. Projection System Optical Design and Calculations

An electron optical model of 200 kV TEM rotation-free projection system was designed within the framework of this thesis. 200 kV electron beam was chosen because it is dominant acceleration voltage used for SPA on mid-range TEMs and the image rotation free imaging is required to allow easy orientation on the sample. The optical model includes three low magnifications which can be used for sample screening and thus the projection system magnification range spans from 50 to 10 000. Important for a SPA use case is to be able reach a $1\,\text{Å/px}$ resolution. Taking into account a pixel size $14\,\mu\text{m} \times 14\,\mu\text{m}^1$ and objective lens magnification $M_{\text{obj}} = 40$, this requires the projection system magnification $M_{\text{proj}} = 3500$, to reach $2\,\text{Å}$ resolution at half the sampling frequency.

Details of used approaches and achieved results are discussed in following subchapters. It is important to emphasize that the main goal is to deliver an optical model and not a complete mechanical design of a TEM projection system assembly, which would require close cooperation of multiple vacuum, electrical and mechanical experts. It was decided to use four identical magnetic electron lenses to obtain the optical model. Four lens projection systems are frequently used in modern TEMs, although the four lenses are not typically identical for various purposes, such as compactness combined with need to accommodate vacuum pipes, DPAs and other mechanical and vacuum elements, cost reduction purposes etc. However, because the goal is to build the optical model, these requirements are not considered and identical lenses are used.

## 4.1 Magnetic Lens Design

The magnetic electron lens was designed and studied in Electron optical design (EOD) software, which facilitates electro- and magnetostatic fields computation and optical properties computation. The used coarse mesh design of the magnetic lens is shown in Fig. 4.1.

A symmetric lens design is used. The bore diameter is 7.5 mm, so the liner with diameter of 7.0 mm can be placed inside it. The gap has diameter of 5.0 mm. According to [50], the ratio between the gap and the bore diameter should not strongly deviate from 1 : 1, which is ideal for minimizing spherical and chromatic aberration coefficients.

---

[1] The pixel size of the Falcon™ 3EC direct electron detection camera [49].

Note that this optical design lacks some key features of real lenses, such as water cooling, power cable feedthroughs and others. Influence of these elements on optical performance can be minimized by a careful design of the whole assembly.

The used material is pure soft iron known under commercial names Behanit or ARMCO® Pure Iron and its initial magnetization curve is showed in Fig. 4.2. The yoke walls thickness is chosen to prevent magnetic field leaks. In later assembly design phases, the material would be probably used for polepieces only. It is because its price is high and the yoke, where lower magnetization is reached can be made of cheaper alloys without changing the optical performance.
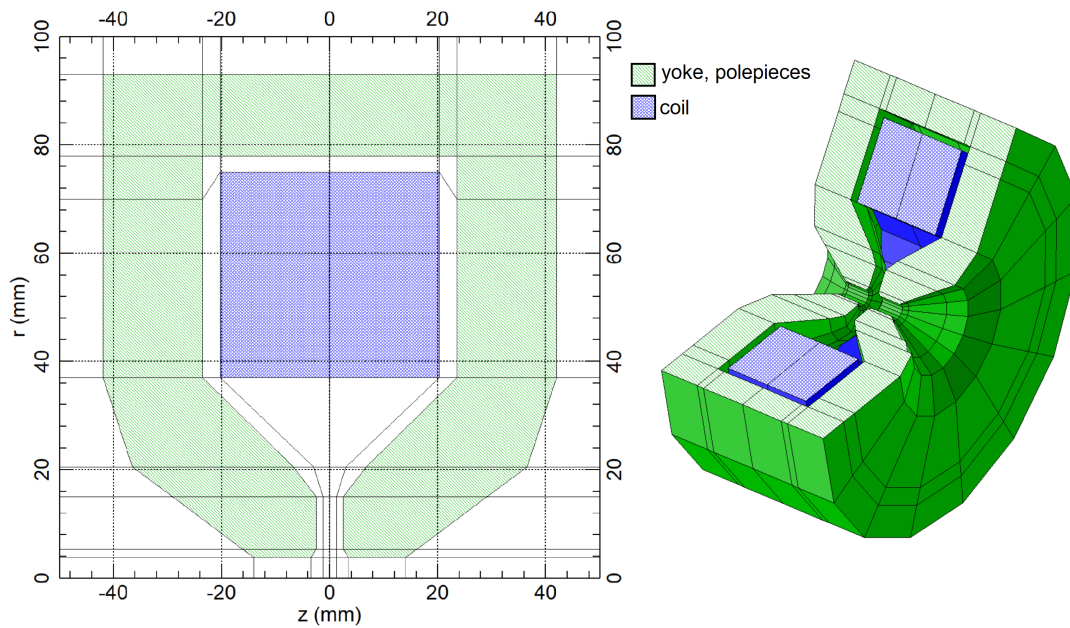


Fig. 4.1: 2D and 3D cross-section of the coarse mesh lens design on the left and right respectively.
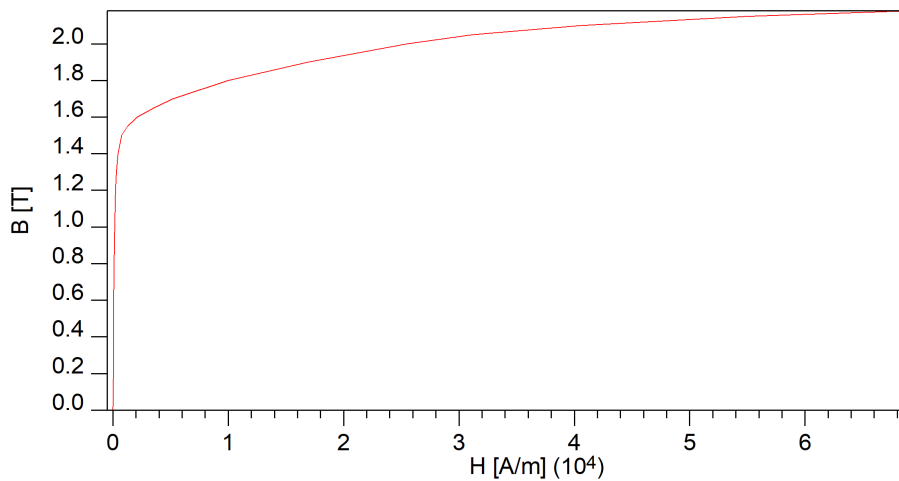


Fig. 4.2: The initial magnetization curve of the used pure iron.

As can be seen from Fig. 4.2, the magnetization curve shows linear behavior up to $\approx 1.1\,\text{T}$, where it starts to deviate from linearity. The saturation magnetization goes

beyond 2.1 T. Since this lens is used in both, the linear and the saturated regime, it is important to find the excitation, where the magnetization of the material reaches $\approx$ 1.1 T and where it gets saturated, to be able to distinguish between these two regimes. The Fig. 4.3 was obtained using EOD and it shows the magnetization map for excitation $NI = 2800$ At up to which is the material in the linear regime (left) and for excitation $NI = 5500$ At, where the maximum magnetization reaches 2.1 T. Areas with the highest magnetization are those near the magnetic gap corners and thus these parts have to be machined with the highest precision.

In the next step, the lens optical properties have been studied for a 200 kV electron beam. The Fig. 4.4, 4.5 and 4.6 show asymptotic values of focal length, principal plane position and rotation angle, respectively, for different lens excitations. The values were obtained using EOD Optics Asymptotic module. Since manually obtaining a large data set from EOD is a time consuming task, the computation process was automated utilizing programming language Julia and EOD application programming interface.

The discrete focal length and the principal plane position data were interpolated using one dimensional cubic interpolation as implemented in SciPy python library. Interpolation is here preferred over fitting which did not yield satisfactory results. The rotation angle data were fitted using linear regression as implemented in polyfit function from NumPy python library. Linear fit is chosen because the rotation angle is linearly proportional to the lens excitation [6] . All three data sets are later used to calculate magnification series and thus continuous data are needed.
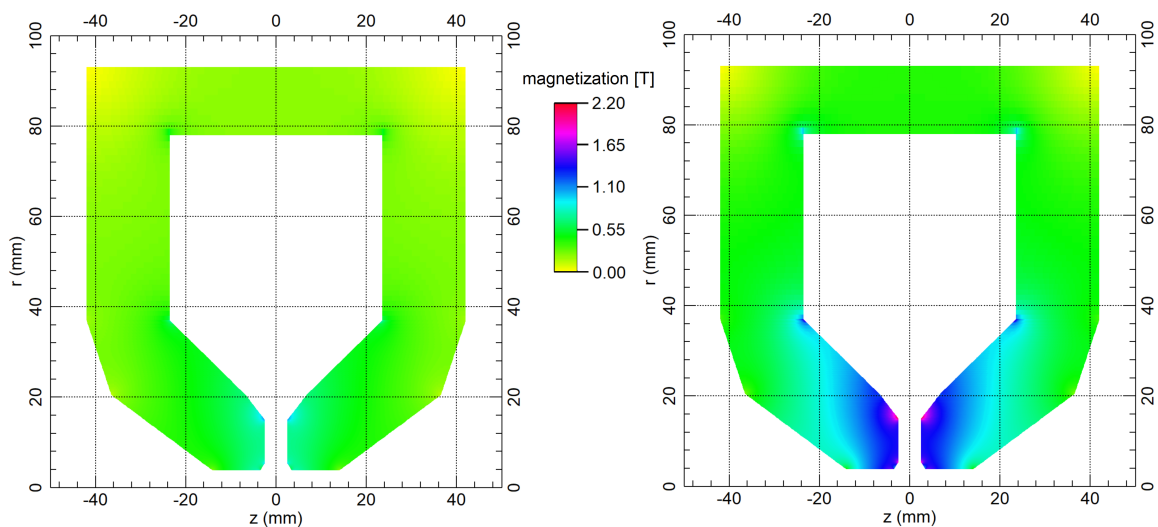


Fig. 4.3: Material magnetization maps computed in EOD for lens excitation $NI = 2800$ At on the left and $NI = 5500$ At on the right.
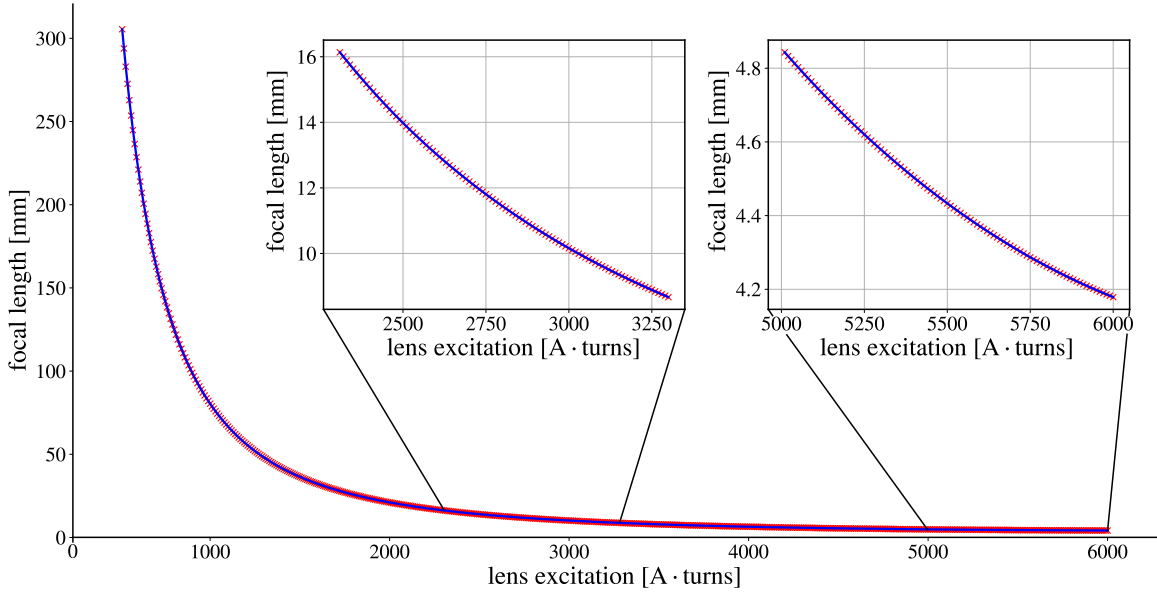
Fig. 4.4: Calculated and interpolated focal lengths for various lens excitation values.

The focal length steeply decreases with increasing lens excitation, but this trend changes for higher excitation values for which its first derivative goes to zero. Hence, a lens operated in saturated regime is less sensitive to fluctuations of lens excitation. However, the principle plane position changes more rapidly with increasing lens excitation. In case of a symmetric lens, both principal planes are positioned symmetrically around its center. The calculated positions can thus reduced to a single parameter, the principal plane distances from the lens center.

Electrons traveling through the magnetic field of the lens follow the helix trajectory. The rotation direction can be flipped by changing the current direction, thus the negative lens excitation values in Fig. 4.6. Switching the current direction does not have any impact on the focal length or the principal plane position.



Fig. 4.5: Calculated and interpolated principal plane positions (principal plane distances from the lens center) for various lens excitation values.
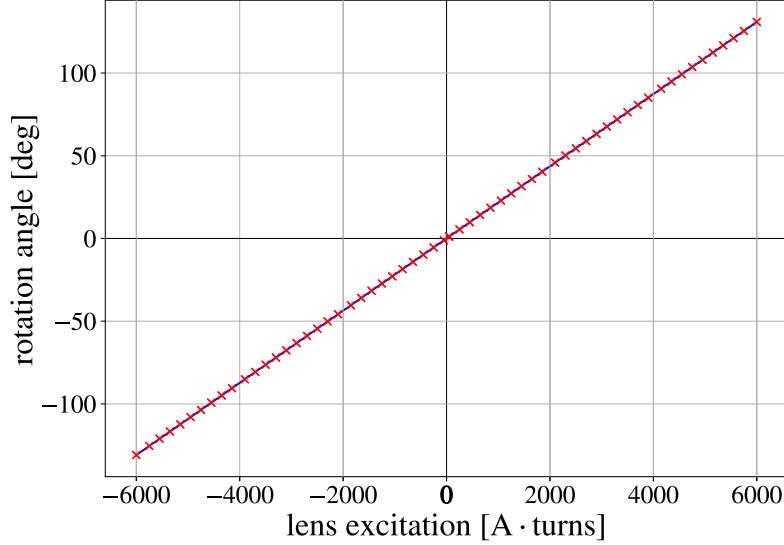
Fig. 4.6: Calculated and linear fitted azimuth rotation angles for various lens excitation values.
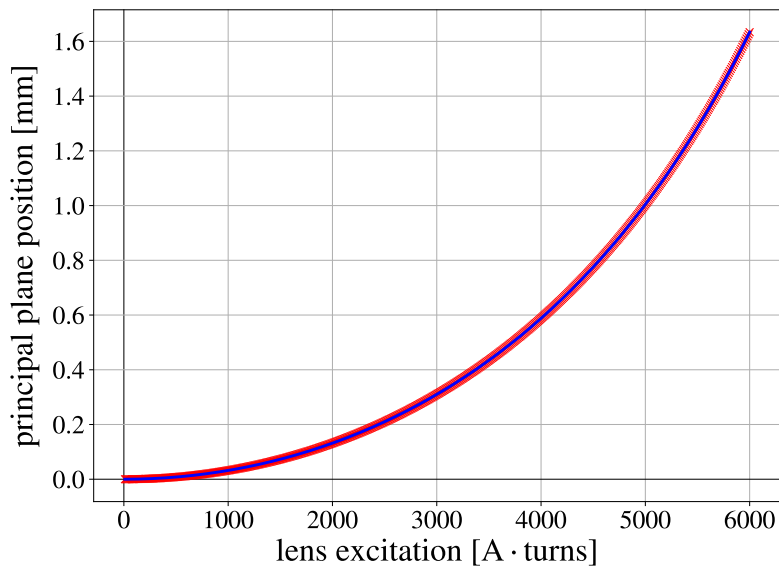
## 4.2    Projection System Design

Dimensions of the designed projection system (see Fig. 4.12) were chosen to be comparable to commercially available systems. The object plane and image plane intersect the optical axis at $z_o = 0\,\mathrm{mm}$ and $z_i = 800\,\mathrm{mm}$, respectively. When designing the projection assembly for TEM it is also important to have enough space below the microscope for accessories, such as cameras or energy filters which are mounted to the bottom of a TEM. Fig. 4.7 show lens and focal length notation used in this chapter.
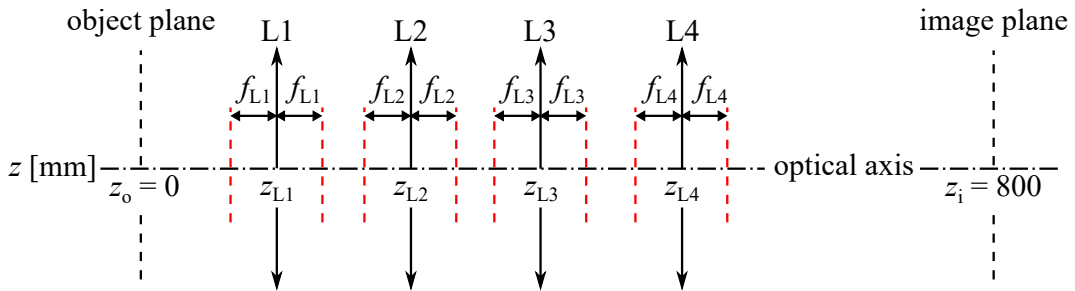


Fig. 4.7: Notation used for projection system lenses. Red dashed lines denote focal planes.

Properties of a general four lens projection system were first studied using thin lens approximation. This approach allows to qualitatively research the properties using equations which require only object and image plane position, lens focal lengths and lens positions.

Magnification maps shown in Fig. 4.8, 4.9, 4.10 and 4.11 are used to demonstrate the effects of various lens positions and focal lengths. The focal length values are chosen to be reachable by the designed magnetic lens. Maps were created for different $f_{L1}$ and $f_{L2}$ focal lengths, horizontal and vertical axis respectively, and a fixed value of

$f_{L4}$. The value of $f_{L3}$ was calculated to satisfy the thin lens equation for a given object and image positions using the following equation

$$f_{L3} = \frac{AB}{C+D},$$

where

$$A = f_{L4}\left(z_i - z_{L3}\right) + \left(z_i - z_{L4}\right)\left(z_{L3} - z_{L4}\right),$$

$$
\begin{aligned}
B = &\left(z_{L2} - z_{L3}\right)\left[-z_{L1}^2 - f_{L1}z_{L2} + f_{L1}z_o - z_{L2}z_o + z_{L1}\left(z_{L2} + z_o\right)\right] + \\
&f_{L2}\left[-z_{L1}^2 - f_{L1}z_{L3} + f_{L1}z_o - z_{L3}z_o + z_{L1}\left(z_{L3} + z_o\right)\right],
\end{aligned}
$$

$$
\begin{aligned}
C = &\left\{f_{L2}\left[f_{L4}\left(z_i - z_{L1}\right) + \left(z_i - z_{L4}\right)\left(z_{L1} - z_{L4}\right)\right] + \right.\\
&\left.\left(z_{L1} - z_{L2}\right)\left[f_{L4}\left(z_i - z_{L2}\right) + \left(z_i - z_{L4}\right)\left(z_{L2} - z_{L4}\right)\right]\right\}\left(z_{L1} - z_o\right)
\end{aligned}
$$

and

$$
\begin{aligned}
D = f_{L1}\Big\{&\left(z_{L2} - z_o\right)\left[f_{L4}\left(z_i - z_{L2}\right) + \left(z_i - z_{L4}\right)\left(z_{L2} - z_{L4}\right)\right] + \\
&f_{L2}\left[\left(z_i - z_{L4}\right)\left(z_{L4} - z_o\right) + f_{L4}\left(-z_i + z_o\right)\right]\Big\}.
\end{aligned}
$$

The magnification is then calculated as follows

$$M = \frac{E + F + G}{H},$$

where

$$
\begin{aligned}
E = f_{L2}\Big\{&f_{L3}\left[f_{L4}\left(z_{L1} - z_i\right) + \left(z_{L1} - z_{L4}\right)\left(z_{L4} - z_i\right)\right] + \\
&\left(z_{L1} - z_{L3}\right)\left[f_{L4}\left(z_{L3} - z_i\right) + \left(z_{L3} - z_{L4}\right)\left(z_{L4} - z_i\right)\right]\Big\},
\end{aligned}
$$

$$
\begin{aligned}
F = \left(z_{L1} - z_{L2}\right)\Big\{&f_{L3}\left[f_{L4}\left(z_{L2} - z_i\right) + \left(z_{L2} - z_{L4}\right)\left(z_{L4} - z_i\right)\right] + \\
&\left(z_{L2} - z_{L3}\right)\left[f_{L4}\left(z_3 - z_i\right) + \left(z_{L3} - z_{L4}\right)\left(z_{L4} - z_i\right)\right]\Big\},
\end{aligned}
$$

$$
\begin{aligned}
G = f_{L1}\Big\{&f_{L3}\left[f_{L4}\left(z_{L2} - z_i\right) + \left(z_{L2} - z_{L4}\right)\left(z_{L4} - z_i\right)\right] + \\
&\left(z_{L2} - z_{L3}\right)\left[f_{L4}\left(z_{L3} - z_i\right) + \left(z_{L3} - z_{L4}\right)\left(z_{L4} - z_i\right)\right] + \\
&f_{L2}\left[f_{L4}\left(z_{L3} - z_i\right) + \left(z_{L3} - z_{L4}\right)\left(z_{L4} - z_i\right) + f_{L3}\left(f_{L4} + z_{L4} - z_i\right)\right]\Big\}
\end{aligned}
$$

and

$$H = f_{L1} f_{L2} f_{L3} f_{L4}.$$

Similar maps were created also for focal length $f_{L3}$ and their side by side comparison with magnification maps reveals which magnifications can be reached with the third lens operated in the linear regime, as shown in Fig. 4.9. This is important because operating lens in the linear regime reduces hysteresis effects when changing the lens excitation. The same concept of magnification maps is in following chapters used to illustrate rotation-free magnification series solutions.

It was found that it is beneficial to place the first lens L1 close to the object plane. Two magnification maps created using two different positions of the first lens, $z_{L1} = 20\,\mathrm{mm}$ and $z_{L1} = 80\,\mathrm{mm}$ are compared in Fig. 4.8. Details of highlighted areas from both maps are presented in Fig. 4.9, where the green dashed lines separates the areas where the $f_{L3} < 10\,\mathrm{mm}$, which is approximately the minimal focal length which can be achieved in the linear regime. From comparison of a) and c), it is clear that the area c) is of more interest when high magnifications are needed. Comparing c) to e) reveals why it is beneficial to place the lens L1 closer to the object plane. However, it cannot be placed too close, so the SA aperture can be moved around in object plane and thus the position $z_{L1} = 52\,\mathrm{mm}$ was chosen.
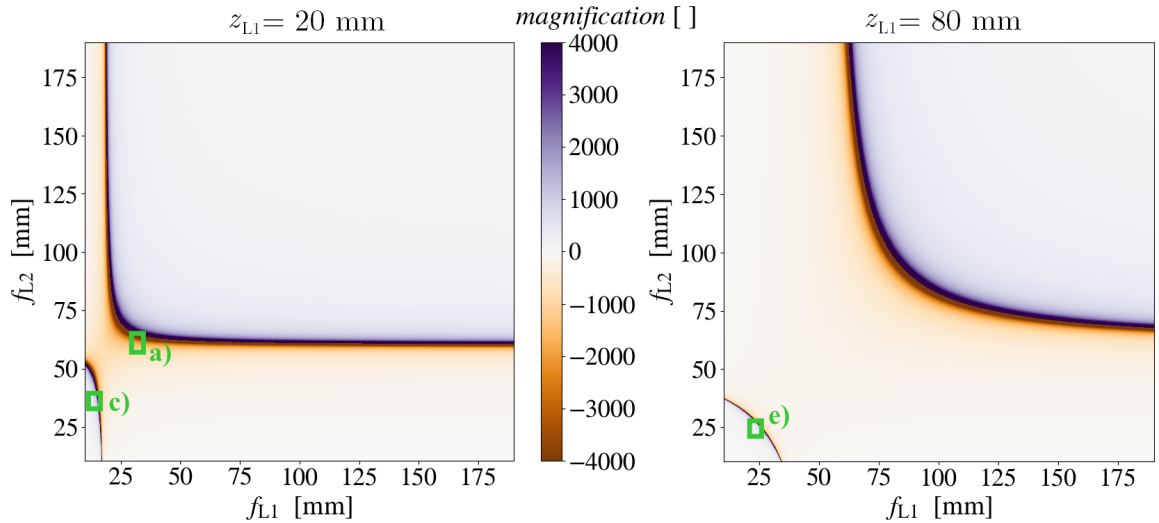


Fig. 4.8: Magnification maps for two different L1 positions. Highlighted areas refer to Fig. 4.9. The $f_{L3}$ is calculated to satisfy thin lens equation and $f_{L4} = 4.5\,\mathrm{mm}$. If the value of any parameter is not explicitly mentioned, the value from the final design (Fig. 4.12) was used.

The L2 and L3 lenses were positioned relatively close to each other, so a more compact design can be achieved. However, putting them too close means that a higher excitation, i.e. a lower focal length, is needed to obtain high magnification and it can results in an unwanted crosstalk between magnetic circuits of lenses. Hence, positions $z_{L2} = 152\,\mathrm{mm}$ and $z_{L3} = 252\,\mathrm{mm}$ were chosen.

A similar analysis as for finding the position of L1 was done also for finding the position of L4. The magnification and $f_{L3}$ maps are shown in 4.10 and the green dashed lines and the green areas indicate that $f_{L3}$ lower than $10\,\mathrm{mm}$ is needed. Although the

figure shows that placing L4 further from L3 is beneficial, further the L4 is placed, higher is the chance that the beam will be cut off by the lens polepieces. Taking this, the call for compactness, and the fact, that an electron beam traveling further from the optical axis suffers more from distortion and other aberrations, into account the L4 was positioned at $z_{L4} = 400\,\text{mm}$.

It was decided to operate the L4 in saturated regime, i.e. low focal length, and there are several arguments that support this decision. Magnification maps for two different focal lengths $f_{L4} = 10\,\text{mm}$ and $f_{L4} = 4.5\,\text{mm}$ are shown in Fig. 4.11. The figure shows that higher magnifications can be reached when lower $f_{L4}$ value is used. Since the L4 is the last lens of the projection system and the column opens wide to the detection unit, the risk of electron beam being limited by the lens or the liner is lowered. It is also preferred that the last lens of the projection system has the highest magnification, because than the image created by previous lenses can be smaller, i.e. the electron beam can travel closer to the optical axis, which results in lower distortion.
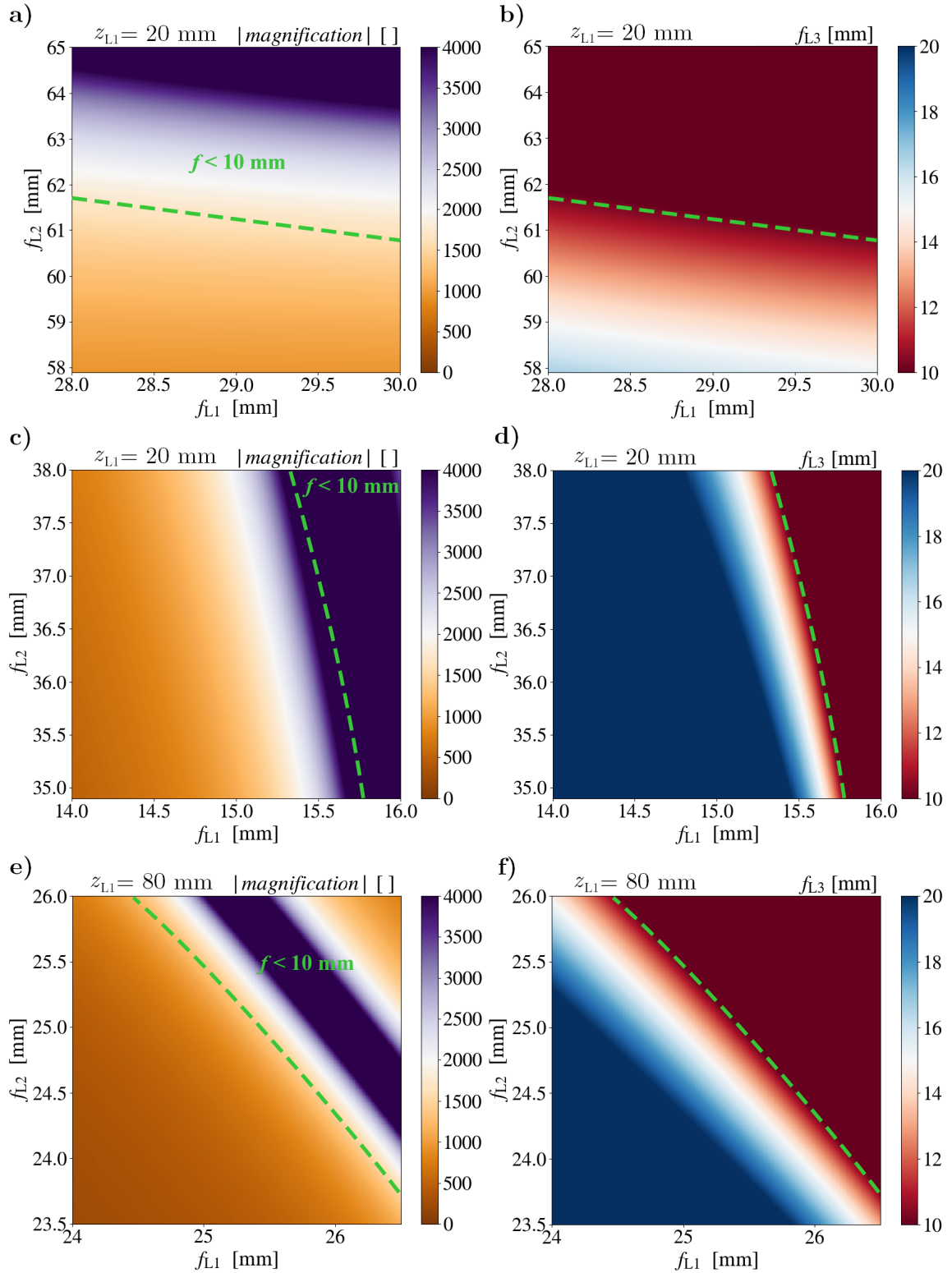
Fig. 4.9: a), c) and e) show detailed study of magnification maps presented in Fig. 4.8 and b), d) and f) show respective $f_{L3}$ maps. Dashed green lines delimit areas with $f_{L3}$ lower than 10 mm, i.e. areas where the lens is expected to be operated in nonlinear regime. The $f_{L3}$ is calculated to satisfy thin lens equation and $f_{L4} = 4.5$ mm. If the value of any parameter is not explicitly mentioned, the value from the final design (Fig. 4.12) was used.

The final design of the projection system is summarized in Fig. 4.12, which shows the schematic drawing and the EOD model of the projection system. The first three lenses L1, L2 and L3 are operated in the linear regime and the L4 is saturated.
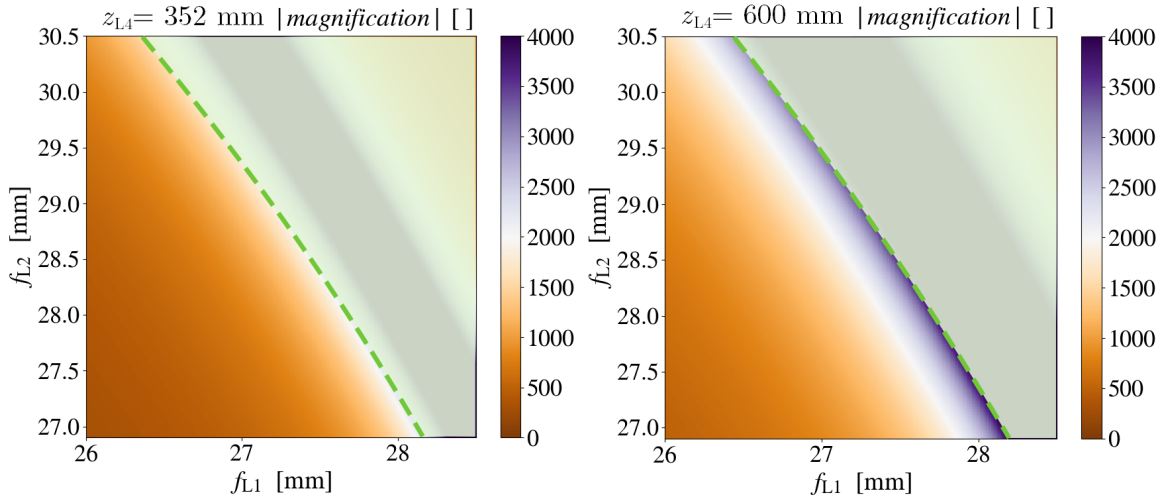


Fig. 4.10: Magnification maps for two different L4 positions. Dashed green lines and areas indicate where the value of $f_{L3}$ is lower than $10\,\text{mm}$, i.e. areas where the lens is expected to be operated in nonlinear regime. The $f_{L3}$ is calculated to satisfy thin lens equation and $f_{L4} = 4.5\,\text{mm}$. If the value of any parameter is not explicitly mentioned, the value from the final design (Fig. 4.12) was used.



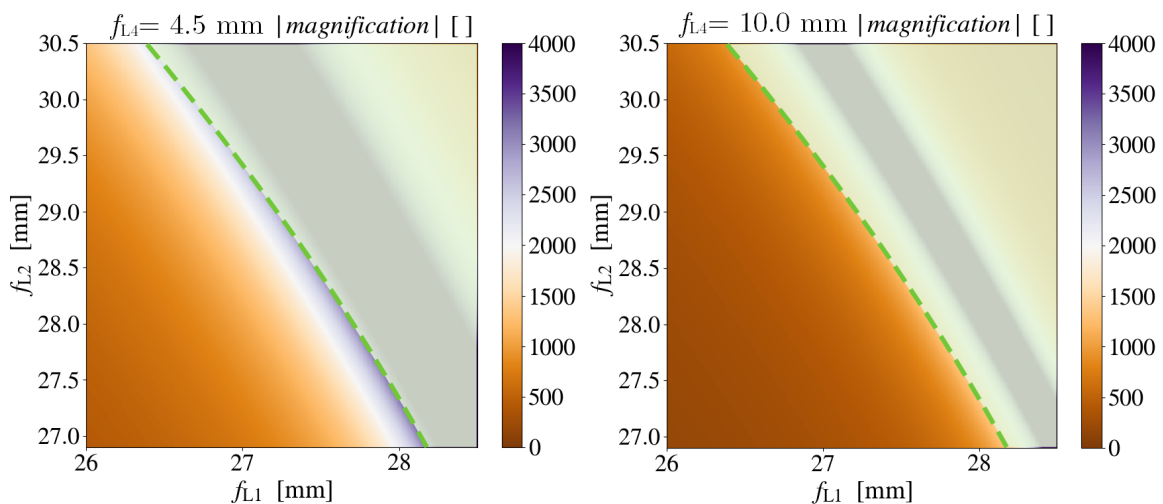Fig. 4.11: Magnification maps for two different $f_{L4}$ values. Dashed green lines and areas indicate where the value of $f_{L3}$ is lower than $10\,\text{mm}$, i.e. areas where the lens is expected to be operated in nonlinear regime. The $f_{L3}$ is calculated to satisfy thin lens equation. If the value of any parameter is not explicitly mentioned, the value from the final design (Fig. 4.12) was used.
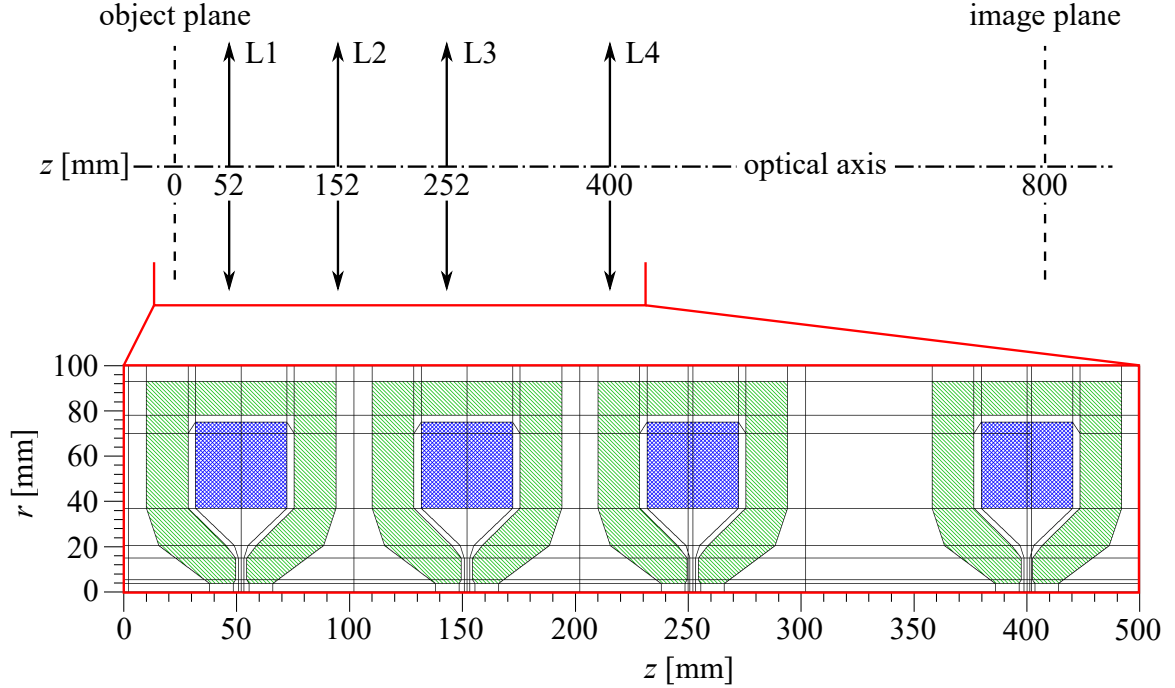
Fig. 4.12: The final design of the projection system. Shown below the schematic drawing is the final version of the EOD model.

## 4.3   Calculation Approaches

A TEM projection system has to cover a wide range of magnifications, which typically spans from hundreds in low magnification mode to tens of thousands in high magnification modes. The total magnification is then given by multiplying the objective lens magnification with the projection system magnification and although the objective lens is saturated in medium and high magnification modes, its excitation is usually very low in low magnification mode. This enables illuminating larger areas and also dramatically changes the objective image position and its magnification. To get a rough estimate of these changes the lower part of the objective lens magnetic field is treated as a thin lens. The focal length $f = 3\,\text{mm}$ and the magnification $M = -40$ are assumed. The minus sign means that the image is inverted relative to the object. The image $d_\text{i}$ and object $do$ distances are then obtained using thin lens equation (Eq. 2.9) and the equation of transverse magnification in thin lens approximation (Eq. 2.10)

$$d_\text{i,HM} = f\left(1 - M\right) = 123\,\text{mm}$$

and

$$d_\text{o} = \frac{d_\text{i,HM} f}{d_\text{i,HM} - f} = 3.08\,\text{mm},$$

respectively. For low excitation is the focal length multiple times longer, $f = 200\,\text{mm}$ is assumed for this estimate. The objective lens thus creates a virtual image as shown

in Fig. 4.13 and the calculated image distance is $d_{i,LM} = -3.13\,\text{mm}$.

Since the objective lens image plane is the object plane for projection system, the position $z_o = d_{i,HM} - d_{i,LM} = -126\,\text{mm}$ is used for calculation of low magnification series, rather than $z_o = 0.00\,\text{mm}$, which used for medium and high magnifications.
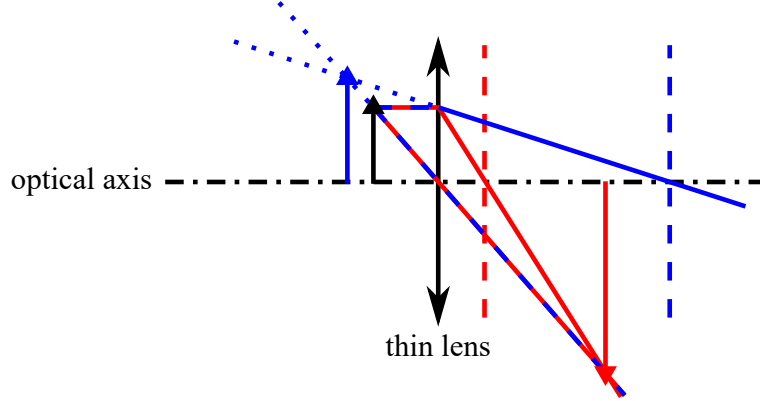


Fig. 4.13: Image construction schematic for two different focal plane positions denoted by a dashed line of respective color.

The thick lens approximation is used as the default approach to finding rotation-free magnification series. Thin lens approximation is later also used and results are compared in the following subchapter. There are four free parameters, the excitations of four lenses, to satisfy following requirements. First, the lens equation needs to be satisfied for given positions of the object, image and lenses. The second requirement is that a certain magnification is achieved. Then it is demanded that the image does not rotate for different magnification values. Since the image rotation is a linear function of lens excitation as shown in Fig. 4.6, the roation-free condition with the tolerance $\pm 1°$ yields that the sum of all four lens excitations has to be within a certain range of values for various magnifications. Moreover, in case of a square detector, an image can be easily rotated by software and thus the total image rotation of $n90°$, where $n$ is an integer, can be also used.

Further requirement is that the L4 excitation is constant, which reduces the number of free parameters to three. The reasoning behind using the L4 in saturated regime is given in previous subchapter and the reason to keep its excitation constant is to preserve the benefits and to minimize the hysteresis effect. The last requirement is to operate L1, L2 and L3 in the linear regime to minimize the hysteresis effect.

Magnification and $f_{L3}$ maps proved to be a convenient way of investigating different parameters during the projection system design phase and thus the same concept is used here to visualize and explore various solutions. For this purpose, excitations of lenses are used as variables rather than focal lengths. In thick lens approximation, a set of two parameters (2.1) is needed to describe the imaging properties and these parameters are unambiguously connected through the lens excitation. Thus, the interpolated data from Fig. 4.4 and 4.5 need to be employed in order to calculate the magnification maps.

The excitations of the first lens $NI_{L1}$ and the second $NI_{L2}$ are varied. The excitation of the fourth lens $NI_{L4} = 5500\,\text{At}$ is fixed and the excitation value of the third lens

$NI_{\mathrm{L3}}$ is found, so the lens equation is satisfied. However, as mentioned in previous paragraph, there are two parameters to be found, the focal length and the principle plane distance from the lens center. The corresponding lens excitation is found using python script, which employs the iterative process depicted in Fig. 4.14.

This iterative process uses the analytical form of equation for $f_{\mathrm{L3}}$, which was obtained from the respective lens equation for four thick lenses,

$$f_{\mathrm{L3}} = \frac{AB}{C+D},$$

where

$$A = f_{\mathrm{L4}}^2 - (z_{\mathrm{Fi,L4}} - z_{\mathrm{i}})(z_{\mathrm{L3}} - z_{\mathrm{Fo,L4}} - d_{\mathrm{P,L3}}),$$

$$B = f_{\mathrm{L1}}^2 (z_{\mathrm{L3}} - z_{\mathrm{Fi,L2}} + d_{\mathrm{P,L3}}) + (z_{\mathrm{Fo,L1}} - z_{\mathrm{o}}) \left[ f_{\mathrm{L2}}^2 + (z_{\mathrm{Fi,L1}} - z_{\mathrm{Fo,L2}})(z_{\mathrm{L3}} - z_{\mathrm{Fi,L2}} + d_{\mathrm{P,L3}}) \right],$$

$$C = (z_{\mathrm{Fo,L1}} - z_{\mathrm{o}})$$
$$\left\{ f_{\mathrm{L4}}^2 (z_{\mathrm{Fi,L1}} - z_{\mathrm{Fo,L2}}) + (z_{\mathrm{Fi,L4}} - z_{\mathrm{i}}) \left[ f_{\mathrm{L2}}^2 - (z_{\mathrm{Fi,L1}} - z_{\mathrm{Fo,L2}})(z_{\mathrm{Fi,L2}} - z_{\mathrm{Fo,L4}} - 2d_{\mathrm{P,L3}}) \right] \right\}$$

and

$$D = f_{\mathrm{L1}}^2 \left[ f_{\mathrm{L4}}^2 - (z_{\mathrm{Fi,L4}} - z_{\mathrm{i}})(z_{\mathrm{Fi,L2}} - z_{\mathrm{Fo,L4}} - 2d_{\mathrm{P,L3}}) \right].$$

$z_{\mathrm{o}}$ and $z_{\mathrm{i}}$ denote the position object and image plane, respectively, $z_{\mathrm{L}n}$ is the position of a respective lens, $z_{\mathrm{Fo,L}n}$ and $z_{\mathrm{Fi,L}n}$ denote the positions of object and image focal planes, respectively, $f_{\mathrm{L}n}$ denotes the focal length and $d_{\mathrm{P,L3}}$ is the L3 principle plane distance from the lens center. The fact that the magnetic field created by the lens is symmetric, was implemented to simplify given terms. The principal planes are located symmetrically around the lens center and thus only the distance can be given. Also the object and the image focal lengths are equal, hence $f_{\mathrm{o,L}n} = f_{\mathrm{i,L}n} = f_{\mathrm{L}n}$.
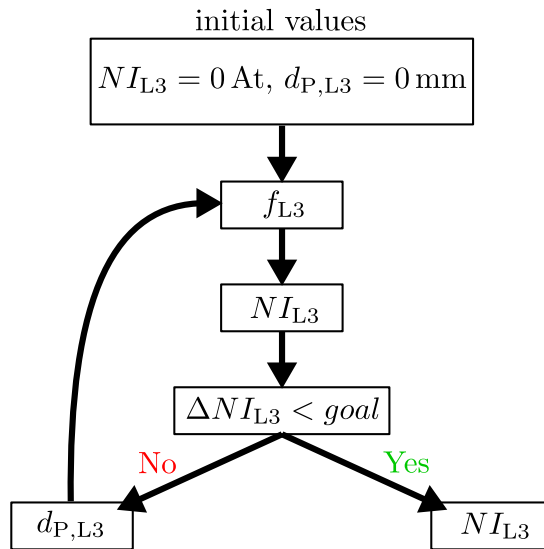


Fig. 4.14: Workflow diagram of the iterative method used to find the L3 excitation, for which $f_{\mathrm{L3}}$ and $d_{\mathrm{P,L3}}$ satisfy lens equation.

After the value of $NI_{\mathrm{L3}}$ is found, the magnification is calculated using the following

analytical form

$$M = \frac{EF + G}{H},$$

where

$$E = \left(z_{\text{Fo,L2}} - z_{\text{Fi,L1}}\right),$$

$$F = f_{\text{L4}}^2 \left(z_{\text{Fi,L2}} - z_{\text{Fo,L3}}\right) + \left(z_{\text{Fi,L4}} - z_{\text{i}}\right) \left[f_{\text{L3}}^2 - \left(z_{\text{Fi,L2}} - z_{\text{Fo,L3}}\right) \left(z_{\text{Fi,L3}} - z_{\text{Fo,L4}}\right)\right],$$

$$G = f_{\text{L2}}^2 \left[f_{\text{L4}}^2 - \left(z_{\text{Fi,L3}} - z_{\text{Fo,L4}}\right) \left(z_{\text{Fi,L4}} - z_{\text{i}}\right)\right]$$

and

$$H = f_{\text{L1}} f_{\text{L2}} f_{\text{L3}} f_{\text{L4}}.$$

To fully understand the achieved solutions it is important to know how is the image created in different areas of magnification maps. Grey areas in Fig. 4.15 on the right denote where L3 needs to be operated in saturated regime, i.e its excitation exceeds 3000 At. These solutions does not fulfill the requirements, hence they are excluded. Remaining segments are color-coded based on how much intermediate real images is created and where they are positioned. Since the $NI_{\text{L4}}$ is constant, at least one intermediate real image needs to be created. $NI_{\text{L3}}$ is calculated so it is created at given position $z = 396.8\,\text{mm}$ so it is imaged by the L4 to the projector image plane $z = 800\,\text{mm}$.

Blue color denotes that only one intermediate real image is created, whereas in the red area are the real images created in between each lens. For both, the green and yellow area, there are two intermediate real images created as shown in Fig. 4.16. The color-coding of imaged rays matches the color-coding from Fig. 4.15, where the respective L1 and L2 excitation values are indicated by white crosses.

The next step is to find the area where the highest required magnification, $\mid M \mid = 10\,000$ can be reached. By careful investigation of magnification maps it was found, that solutions, whose magnification is equal or higher than the highest required, lie in close vicinity of the red and grey area interface. A detail of this interface is shown in Fig. 4.17, where white areas denote that the magnification is lower than required, i.e. $|M| < 10\,000$, grey area contains solutions where the $NI_{\text{L3}} > 3000\,\text{At}$ is needed and in the red area are the solutions with $|M| \geq 10\,000$.

Following excitation values were used to achieve this magnification, $NI_{\text{L1}} = 1590.7\,\text{At}$, $NI_{\text{L2}} = 2749.1\,\text{At}$, $NI_{\text{L3}} = 2658.4\,\text{At}$ and $NI_{\text{L4}} = 5500.0\,\text{At}$. The sum of all excitations, $NI_{\text{sum}} = 12\,498.2\,\text{At}$, is used as default value for finding other rotation-free ($\pm 1°$) solutions and solutions, for which the image rotates by $n90°$. Hence the excitation sum of other solutions have to satisfy following condition

$$NI_{\text{sum}} = (12\,498.2 \pm NI_{1°} - n90 \cdot NI_{1°})\text{At}, \tag{4.1}$$

where $NI_{1°} = 45.8\,\text{At}$ is the excitation that corresponds to a $1°$ rotation. Solutions which satisfy this condition for $n = 0,1,2,3$ are depicted in Fig. 4.18.
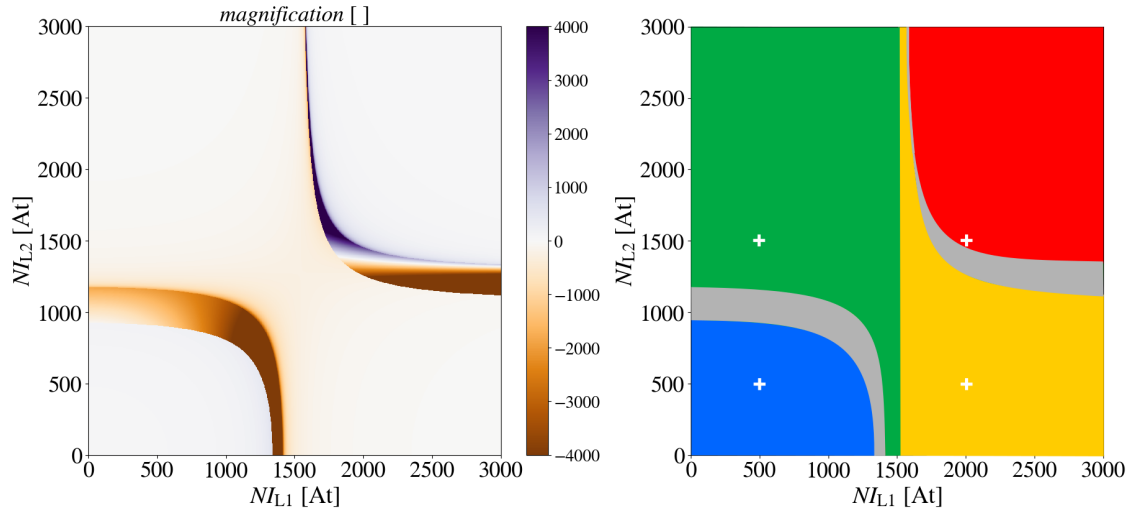
Fig. 4.15: Magnification map shown on left and its segmentation based on the number of intermediate real images and their position shown on right. Blue denotes one intermediate image, green and yellow denote two intermediate images, where the first image is positioned between L2 and L3 and between L1 and L2, respectively. In the red segment, there are three intermediate real images. White crosses denote respective lens excitations used in Fig. 4.16. The $NI_{L3}$ is calculated using the iterative method depicted in Fig. 4.14 and the two grey segments denote where it exceeds 3000 At.
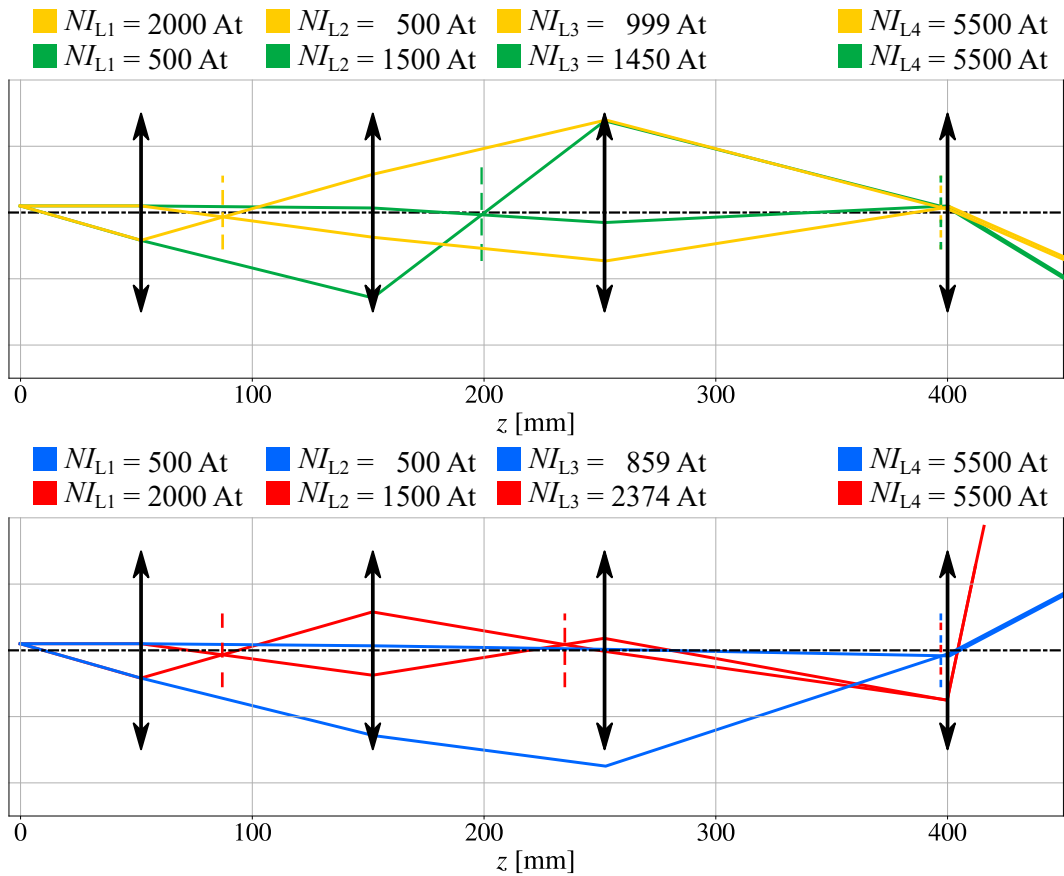


Fig. 4.16: Thick lens ray tracing for given lens excitations. Dashed lines denote intermediate real image planes.
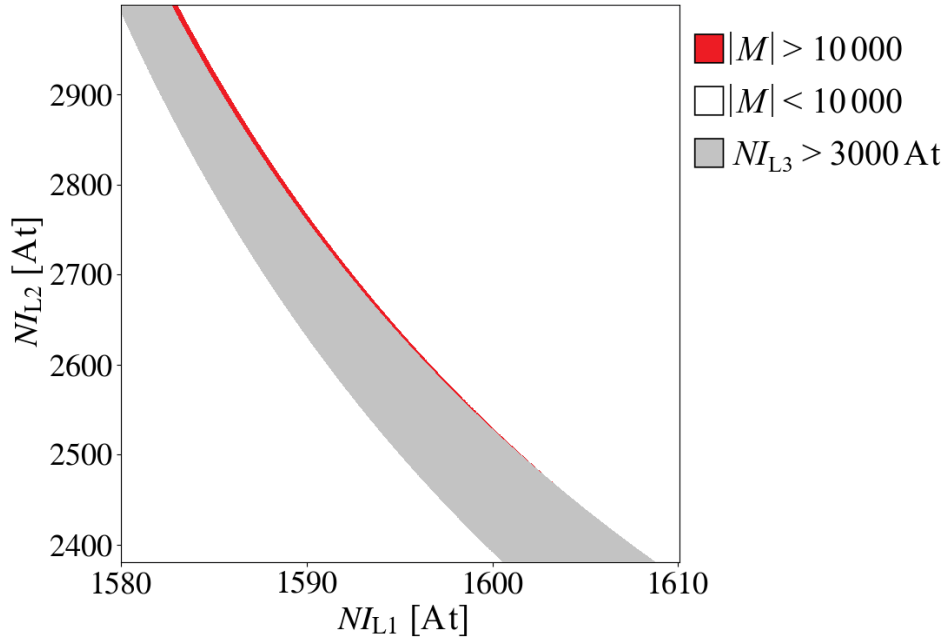
Fig. 4.17: Map of three different groups of solutions. The grey area also contains solutions for which is $|M| > 10\,000$, but these solutions violate the requirement, that L3 needs to be operated in the linear regime.
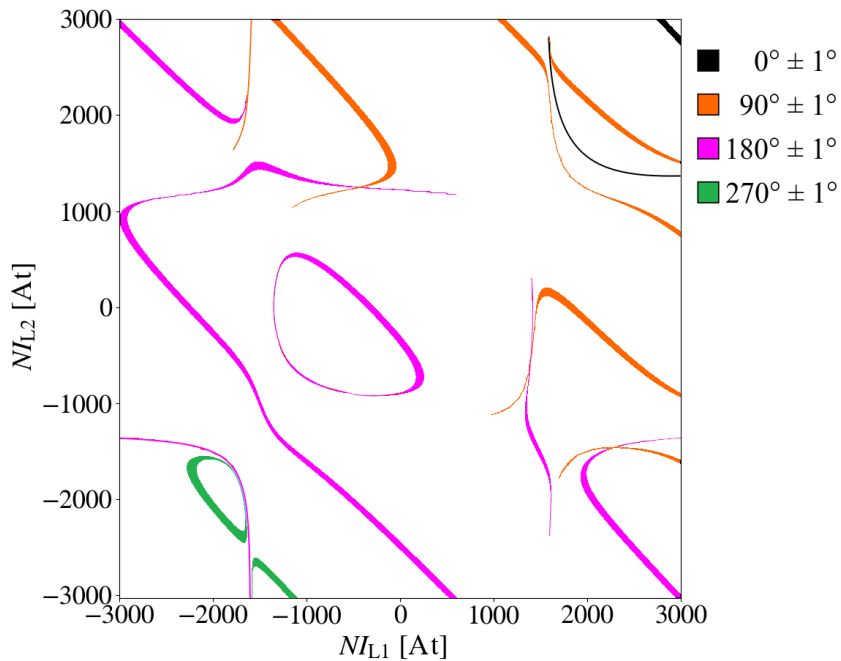


Fig. 4.18: Map of four groups of rotation-free solutions with $\pm 1°$ tolerance. The size of some areas is exaggerated and its shape is smoothed for better visibility. Solutions, for which is $NI_{L3} > 3000\,\text{At}$, are omitted.

## 4.4 Results and Discussion

Two lists of excitations were created, Tab. 4.1 and 4.2. $NI_{L1}$ and $NI_{L2}$ values for given magnifications are found using a magnification map, where only selected rotation-free solutions are displayed, as indicated in Fig.4.18. This map is created using a thick lens approximation and thus the respective value of $NI_{L3}$ is already know. All four $NI_{Ln}$ values are then applied to the EOD 5.003 model of the projection system and the $NI_{L3}$ is then used as a parameter for EOD linear focus method, which iterates over the field magnitude. This approach is very fast and each linear focus computation took less than five seconds. Laptop equipped with Intel® Core™ i5-6300U 2.5 GHz, 8.00 GB RAM and 64-bit Windows 10 operating system was used for all computations. Linear focus results were validated using EOD nonlinear focus, which iterates over the lens excitation, and respective $\Delta = |NI_{L3,\mathrm{lin}} - NI_{L3,\mathrm{nonlin}}|$ values are shown in the rightmost column. Since the magnetic field needs to be calculated during each iteration, nonlinear computation took up to ten minutes depending on number of iterations needed. The linear behavior was confirmed for all the calculated magnifications. The same $NI_{L1}$, $NI_{L2}$ and $NI_{L4}$ values were then also used to calculate $NI_{L3}$ in thin lens approximation.

The first list is the low magnification list, for which is the excitation of objective lens considered to be very low. Thus, $z_{\mathrm{o}} = -126$ mm is used to calculate $NI_{L3}$ excitation, as explained in previous subchapter. These three magnifications were selected to facilitate orientation on the sample and to be used for automatized screening of the sample. Therefore, it is needed to ensure that the field of view is not limited by the projection system. The risk that the electron beam is limited by the liner is higher for low magnification series, because the beam travels further from the optical axis. All three magnifications were checked for possible cutoffs by tracing particles in EOD, see Fig. 4.19, where $|M| = 50$ and $|M| = 500$ are compared.

The initial positions of particles are chosen so that the particles, which start furthest from optical axis, intersect the image plane at $r = 42$ mm. This would be the distance from the corner to the center of a $6$ cm $\times$ $6$ cm detector.

Lens aberrations cause that the particles actually intersect the image plane further or closer to the optical axis, but this has low importance for low magnification imaging.

By summing the excitations of all four lenses it is easily seen that the values obtained by thick lens approximation and EOD satisfy the rotation-free condition (Eq. 4.1) for $n = 2$, which means that the image is rotated 180° against the highest magnification image. However, unlike for the highest magnification, where three intermediate images are created, in case of $|M| = 50$ and $|M| = 200$, there are only two intermediate real images and thus the image is not actually rotated at all. For $|M| = 500$ there are three intermediate images. The thin lens values satisfy the rotation-free condition only for $|M| = 50$ and $|M| = 200$.

It is important to note, that since the sample is immersed in the objective lens magnetic field, the change of the objective excitation introduces a change of an image rotation, which should be taken into account. However, this thesis deals solely with a projection system and this effect is unknown and therefore not considered.
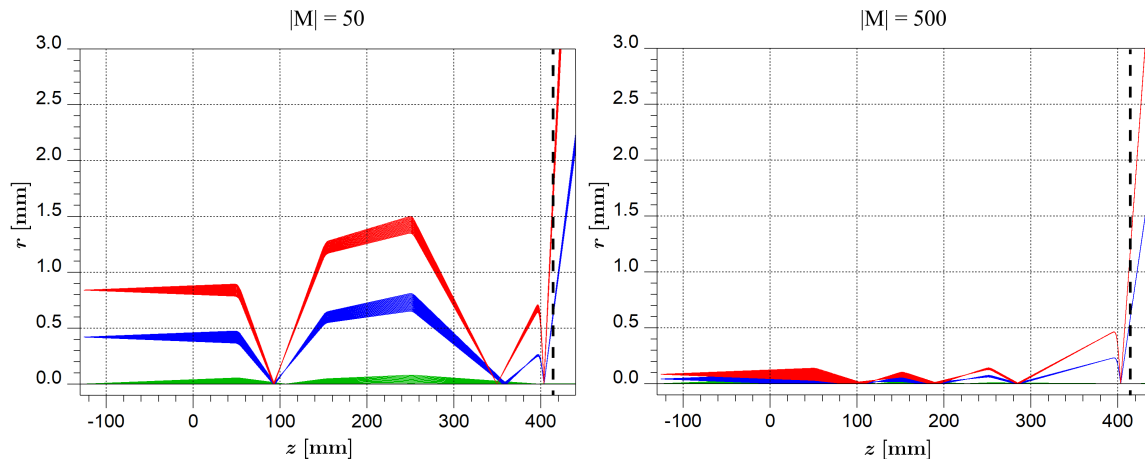
Fig. 4.19: Low magnification series particle trajectories for $|M| = 50$ on the left and $|M| = 500$ on the right. The data were obtained using EOD particle tracer. The liner radius is $3.0\,$mm and the dashed black line denotes the position, where the narrow part of the last lens gap ends.

Tab. 4.1: Calculated $NI_{L3}$ values for low magnification series using various approaches, $NI_{L4} = 5500\,$At. The rightmost column contains the $NI_{L3}$ differences between EOD linear and nonlinear focus method.

|  |  |  | thin lens | thick lens | EOD | linearity |
|---|---|---|---|---|---|---|
| nominal $|M|$ | $NI_{L1}$[At] | $NI_{L2}$[At] | $NI_{L3}$[At] | $NI_{L3}$[At] | $NI_{L3}$[At] | $\Delta$[At] |
| 50 | $-1400.0$ | $1083.3$ | $-948.2$ | $-944.7$ | $-944.6$ | $0.0$ |
| 200 | $950.0$ | $-659.0$ | $-1543.3$ | $-1539.8$ | $-1539.8$ | $0.0$ |
| 500 | $-1270.3$ | $1980.0$ | $-2028.2$ | $-1972.9$ | $-1971.1$ | $0.2$ |

The medium and high magnification list (Tab. 4.2) covers a wide range of magnifications. The objective lens is considered to be operated in saturated regime, hence $z_o = 0\,$mm is used for calculations. Note that listed are the projection system magnifications, the total magnification of a TEM is the product of the objective and projection system magnification.

The medium magnification range 50–1000 is included, because it is necessary for TEM alignment procedures. The rest of the list covers the most critical magnifications for SPA, 2000–5000, and goes even beyond, which gives the projection system more versatility.

Tab. 4.2: Calculated $NI_{L3}$ values for high magnification series using various approaches, $NI_{L4} = 5500\,\text{At}$. The rightmost column contains the $NI_{L3}$ differences between EOD linear and nonlinear focus method.

|  |  |  | thin lens | thick lens | EOD | linearity |
|---|---|---|---|---|---|---|
| nominal $\lvert M \rvert$ | $NI_{L1}[\text{At}]$ | $NI_{L2}[\text{At}]$ | $NI_{L3}[\text{At}]$ | $NI_{L3}[\text{At}]$ | $NI_{L3}[\text{At}]$ | $\Delta[\text{At}]$ |
| 50 | $-775.0$ | $-1780.0$ | $1318.2$ | $1315.1$ | $1315.1$ | $0.0$ |
| 100 | $-1055.0$ | $-1561.0$ | $1374.0$ | $1370.8$ | $1370.8$ | $0.0$ |
| 500 | $-1694.0$ | $1984.0$ | $-1539.9$ | $-1524.3$ | $-1524.7$ | $0.1$ |
| 1000 | $-1656.8$ | $2068.4$ | $-1700.2$ | $-1657.6$ | $-1658.8$ | $0.3$ |
| 2000 | $-1628.1$ | $2220.0$ | $-2004.6$ | $-1848.3$ | $-1853.7$ | $0.0$ |
| 2500 | $-1620.5$ | $2285.0$ | $-2163.8$ | $-1915.1$ | $-1921.8$ | $0.3$ |
| 3000 | $-1614.5$ | $2347.5$ | $-2358.3$ | $-1974.0$ | $-1983.8$ | $0.1$ |
| 3500 | $-1610.2$ | $2398.5$ | $-2623.0$ | $-2035.2$ | $-2049.6$ | $0.4$ |
| 4000 | $-1606.5$ | $2449.0$ | $-2992.6$ | $-2087.3$ | $-2104.6$ | $0.2$ |
| 5000 | $-1600.8$ | $2450.0$ | $-5132.0$ | $-2182.3$ | $-2204.3$ | $0.1$ |
| 7500 | $-1591.6$ | $2734.0$ | $< -5500.0$ | $-2373.1$ | $-2320.0$ | $0.1$ |
| 10 000 | $1590.7$ | $2749.1$ | $< -5500.0$ | $2658.4$ | $2572.3$ | $0.2$ |

There is a notable variation between the thick lens and EOD $NI_{L3}$ values for the highest magnifications, which is even stronger for thin lens values. The ratios between thick and thin lens $NI_{L3}$ values are plotted in Fig. 4.20 together with thick lens to EOD ratios.
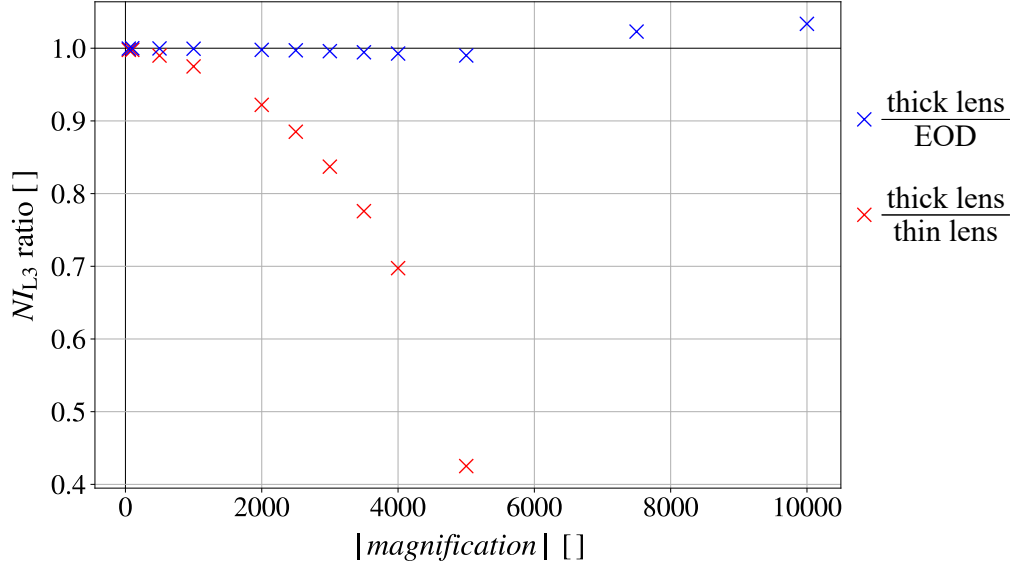


Fig. 4.20: $NI_{L3}$ ratios for different calculation approaches.

All listed magnifications have been checked for possible electron beam cutoffs utilizing EOD tracer. The same strategy, that has been used to determine initial positions of electrons for low magnification tracing, is employed. The initial half angle spread for the highest magnification is calculated from Eq. 1.3, where $\lvert \mathbf{q} \rvert = \frac{1}{d}$. Assuming the desired resolution $d = 2\,\text{Å}$ and $200\,\text{kV}$ electron beam yields $\theta = 12.55\,\text{mrad}$, which is

further by the objective lens. The respective half angle spread at projection system object plane $z_\mathrm{o}$ can be then written as $\theta_\mathrm{proj} = \frac{\theta}{|M_\mathrm{obj}|}$, where $M_\mathrm{obj}$ is the transverse magnification of the objective lens. Since the $|M_\mathrm{obj}| = 40$ is assumed, the $\theta_\mathrm{proj} = 0.31\,\mathrm{mrad}$ is used for tracing. The trajectories through the projection system for $|M| = 50$, $3500$ and $10\,000$ are shown in Fig. 4.21. The particles were traced using $NI_\mathrm{L3}$ obtained by thick lens approximation and EOD linear focus to confirm that the beam cutoff does not appear for any of both approaches.

EOD tracer includes the effect of geometrical aberrations and therefore were the obtained tracing data also used to measure the radial spread of particles intersecting the image plane $z_\mathrm{i}$. It is required that the radial spread is smaller than the assumed pixel size $14\,\mathrm{\mu m}$. The results are shown in Tab. 4.3. The $NI_\mathrm{L3}$ values obtained by EOD linear focus clearly give better results than the thick lens approach, for which the $\Delta r$ data show that the required spatial frequency is not sufficiently transferred. This is demonstrated also in Fig. 4.21 d), which shows $\Delta r_0$ spread for $|M| = 3500$.
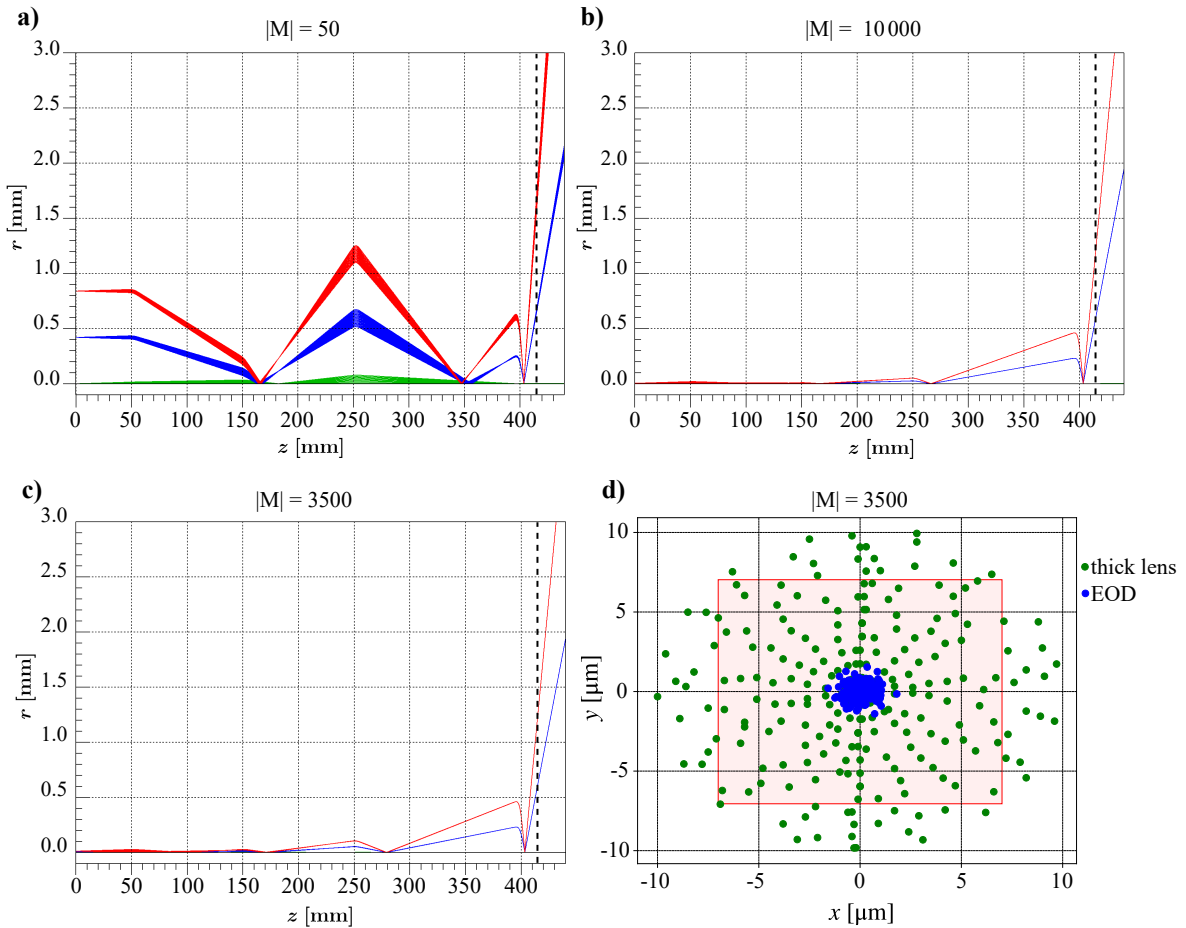


Fig. 4.21: High magnification series particle trajectories for a) $|M| = 50$, b) $|M| = 10\,000$ and c) $|M| = 3500$. The data were obtained using EOD particle tracer. The liner radius is $3.0\,\mathrm{mm}$ and the dashed black line denotes the position, where the narrow part of the last lens gap ends. d) shows where the particles starting from $r = 0.0\,\mathrm{mm}$ intersect the image plane. Dimensions of the red rectangle correspond to the size of a single $14\,\mathrm{\mu m} \times 14\,\mathrm{\mu m}$ pixel.

Tab. 4.3: List of radial spread values at image plane for $r = 0\,\mathrm{mm}$ and $r = 42\,\mathrm{mm}$.

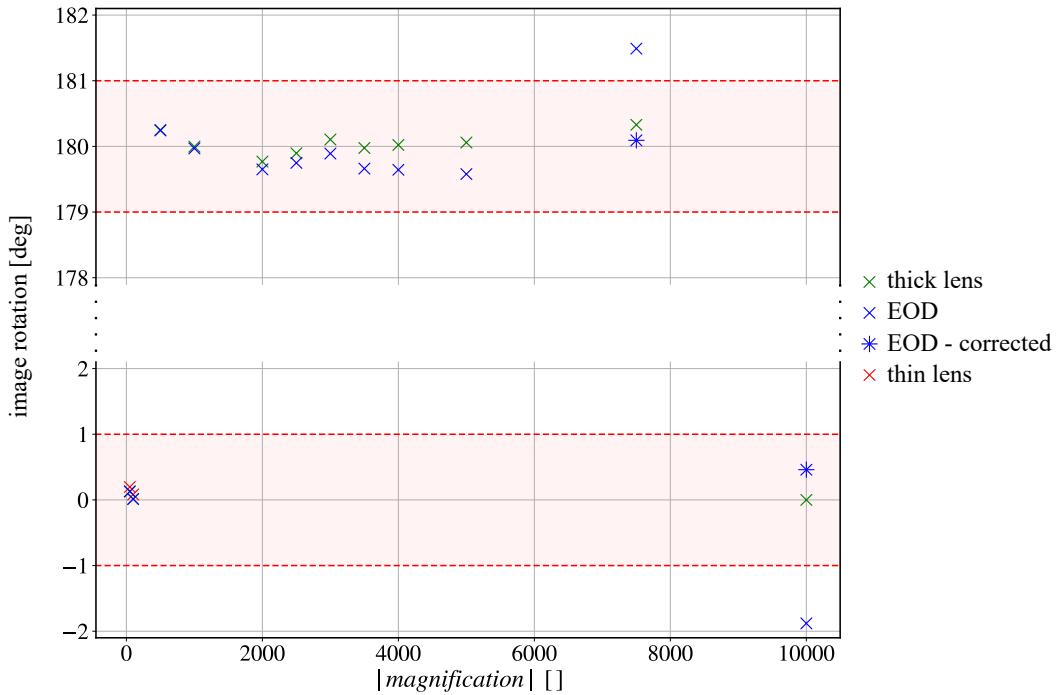| | thick lens | | EOD | |
| --- | --- | --- | --- | --- |
| nominal $|M|$ | $\Delta r_0\,[\mu\mathrm{m}]$ | $\Delta r_{42}\,[\mu\mathrm{m}]$ | $\Delta r_0\,[\mu\mathrm{m}]$ | $\Delta r_{42}\,[\mu\mathrm{m}]$ |
| 50 | $< 5$ | $> 200$ | $< 5$ | $> 200$ |
| 100 | 20 | 180 | 20 | 180 |
| 500 | $< 5$ | 150 | $< 5$ | 150 |
| 1000 | 6 | 25 | $< 5$ | 35 |
| 2000 | 10 | $< 5$ | $< 5$ | 10 |
| 2500 | 12 | 6 | $< 5$ | 7 |
| 3000 | 15 | 9 | $< 5$ | $< 5$ |
| 3500 | 20 | 22 | $< 5$ | $< 5$ |
| 4000 | 22 | 19 | $< 5$ | $< 5$ |
| 5000 | 24 | 18 | $< 5$ | $< 5$ |
| 7500 | 40 | 40 | $< 5$ | $< 5$ |
| 10 000 | 50 | 50 | $< 5$ | $< 5$ |



Fig. 4.22: Image rotation of medium and high magnification series with respect to image rotation of $|M| = 10\,000$ in thin lens approximation. Although all solutions, except for $|M| = 10\,000$, satisfy the rotation-free condition for $n = 2$, there is one less intermediate real image created in case of $|M| = 50$ and $|M| = 100$.

The total image rotation relative to the image rotation of the highest magnification in thick lens approximation is shown in Fig. 4.22. The solutions for which $n = 2$, except for the highest magnification for which $n = 0$, were chosen to satisfy rotation-free condition. The figure shows, that EOD calculated values violate this condition for $|M| = 7500$ and $|M| = 10\,000$. Since the radial spread analysis proved that EOD

calculated $NI_{L3}$ yield better results, these two magnifications were recalculated, so the desired magnification is achieved and the rotation-free condition satisfied. $NI_{L1}$ values were lowered by 0.1 At and new respective $NI_{L3}$ values were computed by EOD linear focus, see Tab. 4.4. This correction provided results, which fulfill all requirements.

Tab. 4.4: Corrected excitation parameters and respective radial spread values.

| nominal $|M|$ | $NI_{L1}$[At] | $NI_{L2}$[At] | $NI_{L3}$[At] | $\Delta r_0$ [µm] | $\Delta r_{42}$ [µm] |
|---|---|---|---|---|---|
| 7500 | $-1591.5$ | 2734.0 | $-2384.1$ | $< 5$ | $< 5$ |
| 10 000 | 1590.6 | 2749.1 | 2677.0 | $< 5$ | $< 5$ |

# Conclusion

The main focus of this diploma thesis was to deliver an optical model of TEM projection system optimized for the SPA use case and to compare results achieved by various calculation approaches. The EOD model of the designed four lens projection system and lens excitations calculated by thin and thick lens approximation, EOD linear focus and nonlinear focus method are the main outputs of this thesis.

The theoretical study provided in the first chapter covers essential TEM modules and techniques. The origin of contrast in TEM was explained with an extra focus on phase contrast, which is the dominant contrast mechanism in SPA measurements. The second chapter introduced Gaussian and matrix optics formalism which was later used to obtain analytical formulae of lens equation in thin and thick lens approximation for the whole projection system. The SPA workflow was explained in the third chapter.

The last chapter is dedicated to the electron optical design of the $200\,\text{kV}$ TEM rotation-free projection system and various approaches of lens excitation series calculation. Based on the articles presented in the third chapter, the target resolution was determined to be $2\,\text{Å}$ at half the sampling frequency of a pixelated detector with $14\,\mu\text{m} \times 14\,\mu\text{m}$ pixel size.

It was decided to create a projection system, which consists of four identical lenses. The magnetic lens design was created in EOD and its optical properties for a wide range of lens excitations were obtained utilizing a Julia script to control EOD. The effect of lens positions on imaging performance of the projection system was studied in thin lens approximation. Together with mechanical limitations, these findings were used to determine positions of all four lenses.

Using the same procedure as for finding the lens positions, it was found that it is beneficial to operate the last lens of the projection system at minimum focal length. Since the lens polepieces get saturated when operated at low focal lengths, it was decided to keep the excitation of this lens constant to avoid hysteresis effect. The excitations of first two lenses were set freely and the excitation of the third lens was computed to satisfy thick lens equation. This approach allowed easy selection of solutions, which satisfied image rotation and magnification requirements. The image rotation requirements were set so the image can rotate by $n90° \pm 1°$, where $n$ is an integer, since such rotation can be easily corrected by software without loosing any information if a square detector is used.

Two lists of magnifications were created, one for low magnifications, for which is the excitation of the objective lens very low, and one for medium and high magnifications, for which is the objective lens saturated. The projection system magnification ranges

from 50 to 500 and from 50 to 10 000, respectively. Solutions were first found using the thick lens approach and then the same excitation of the first, the second and the fourth lens were used to find the excitation of third lens using thin lens approximation. The excitation values determined by thick lens approach were used for EOD linear focus method, which iterated over the field magnitudes of the third lens.

Values of lens excitations found by thick lens approach and EOD linear focus, were used to calculate magnetic fields and EOD tracer was used to compare the performance. It was found that EOD linear focus gives better results and that the desired resolution can be achieved for all relevant magnifications. Since the solutions found by EOD linear focus for the two highest magnifications violated the rotation-free requirements, the new solutions were found by a slight offset of the first lens excitation and recalculation of the EOD linear focus for the third lens. This corrected solutions fulfill all requirements.

# Bibliography

[1] *Press release: The Nobel Prize in Chemistry 2017.* Nobel Media AB. Available also from:
    <https://www.nobelprize.org/prizes/chemistry/2017/press-release/>.

[2] HAMAGUCHI, T.; MAKI-YONEKURA, S.; NAITOW, H., et al. A new cryo-EM system for single particle analysis. *Journal of Structural Biology.* 2019, **207**(1), 40–48. ISSN 10478477. Available from DOI: 10.1016/j.jsb.2019.04.011.

[3] FAN, X.; WANG, J.; ZHANG, X., et al. Single particle cryo-EM reconstruction of 52 kDa streptavidin at 3.2 Angstrom resolution. *Nature Communications.* 2019, **10**(1). ISSN 2041-1723. Available from DOI: 10.1038/s41467-019-10368-w.

[4] SEVVANA, M.; LONG, F.; MILLER, A. S., et al. Refinement and Analysis of the Mature Zika Virus Cryo-EM Structure at 3.1 A Resolution. *Structure.* 2018, **26**(9), 1169–1177.e3. ISSN 09692126. Available from DOI: 10.1016/j.str.2018.05.006.

[5] WU, M.; LANDER, G. C.; HERZIK, M. A. Sub-2 Angstrom resolution structure determination using single-particle cryo-EM at 200 keV. *Journal of Structural Biology: X.* 2020, **4**, 100020. ISSN 2590-1524. Available from DOI: 10.1016/j.yjsbx.2020.100020.

[6] REIMER, L.; KOHL, H. *Transmission electron microscopy: physics of image formation.* 5th ed. New York: Springer, 2008. ISBN 978-0-387-40093-8.

[7] WILLIAMS, D. B.; CARTER, C. B. *Transmission electron microscopy: a textbook for materials science.* 2nd ed. New York: Springer, 2009. ISBN 978-0-387-76500-6.

[8] CARTER, C. B.; WILLIAMS, D. B. *Transmission Electron Microscopy: Diffraction, Imaging, and Spectrometry.* Switzerland: Springer, 2016. ISBN 978-3-319-26649-7.

[9] *Lanthanum hexaboride filaments.* Available also from:
    <https://www.agarscientific.com/lanthanum-hexaboride-filaments>.

[10] *Electron Microscope Filaments: Cathodes Overview.* Available also from:
    <https://www.tedpella.com/apertures-and-filaments_html/tungsten-filaments.htm>.

[11]  *Micro to Nano: Innovative Microscopy Supplies.* Available also from: `<https://www.microtonano.com/YPS-TFE-emitters-schottky-thermal-field-emission-sources.php>`.

[12]  *YPS :: Emitters.* Available also from: `<http://www.yps-ltd.com/index.php/products/emitters/>`.

[13]  *Electron Microscopy Sciences: Applied Physics Lanthanum and Cerium Hexaboride LaB6 and CeB6 Filaments / Cathodes.* Available also from: `<https://www.emsdiasum.com/microscopy/products/microscope/lab6_ceb6.aspx>`.

[14]  SWANSON, L. W.; SCHWIND, G. A. Review of ZrO/W Schottky Cathode. In: *Handbook of Charged Particle Optics.* 2nd ed. Boca Raton: CRC Press, 2009, pp. 1–28. ISBN 978-1-4200-4554-3.

[15]  UL-HAMID, A. Components of the SEM. In: *A Beginners' Guide to Scanning Electron Microscopy.* Switzerland: Springer, 2018, pp. 15–76. ISBN 978-3-030-07498-2.

[16]  TSUNO, K. Magnetic Lenses for Electron Microscopy. In: *Handbook of Charged Particle Optics.* 2nd ed. Boca Raton: CRC Press, 2009, pp. 129–157. ISBN 978-1-4200-4554-3.

[17]  HAWKES, P. W.; KASPER, E. *Principles of Electron Optics: Basic Geometrical Optics.* Academic Press, 1996. ISBN 9780080962412.

[18]  HAWKES, P. W.; KASPER, E. *Principles of Electron Optics: Basic Geometrical Optics.* 2nd ed. London: Elsevier AP, Academic Press, 2018. ISBN 978-008-1022-566.

[19]  SHANEL, O. *Tolerances and Misalignment Aberrations for Electron Optical Elements and Systems.* Brno, 2014. Dissertation. Brno University of Technology, Faculty of Mechanical Engineering.

[20]  BISCHOFF, M.; HENSTRA, A.; LUECKEN, U.; TIEMEIJER, P. C. *Distortion free stigmation of a TEM.*

[21]  ZHU, X.; LIU, H.; MUNRO, E. Dynamic correction of aberrations in focusing and deflection systems with shaped beams. *International Symposium on Optical Science, Engineering, and Instrumentation.* 1995, 66–77. Available from DOI: `10.1117/12.221617`.

[22]  *Electron Microscope Aperture Overview.* Available also from: `<https://www.tedpella.com/apertures-and-filaments_html/apertures-overview.htm>`.

[23]  ZHANG, C.; FIRESTEIN, K. L.; FERNANDO, J. F. S., et al. Recent Progress of In Situ Transmission Electron Microscopy for Energy Materials. *Advanced Materials.* 2020, **32**(18). ISSN 0935-9648. Available from DOI: `10.1002/adma.201904094`.

[24] UESUGI, K.; HOSHINO, M.; YAGI, N. Comparison of lens- and fiber-coupled CCD detectors for X-ray computed tomography. *Journal of Synchrotron Radiation*. 2011, **18**(2), 217–223. ISSN 0909-0495. Available from DOI: 10.1107/S0909049510044523.

[25] WU, S.; ARMACHE, J.-P.; CHENG, Y. Single-particle cryo-EM data acquisition by using direct electron detection camera. *Microscopy*. 2016-02-03, **65**(1), 35–41. ISSN 2050-5698. Available from DOI: 10.1093/jmicro/dfv355.

[26] WELLNER, A.; NELLIST, P. D.; PALMER, R. E., et al. Orientational and translational ordering of sub-monolayer films of passivated multiply-twinned gold clusters. *Journal of Physics D: Applied Physics*. 2000-01-21, **33**(2), 23–26. ISSN 0022-3727. Available from DOI: 10.1088/0022-3727/33/2/104.

[27] KACHTÍK, L. *Aplikace transmisní elektronové mikroskopie s vysokým rozlišením pro strukturní analýzu nanovláken*. Brno, 2016. Master's thesis. Brno University of Technology, Faculty of Mechanical Engineering.

[28] ERNI, R. *Aberration-Corrected Imaging in Transmission Electron Microscopy: An Introduction*. 2nd rev. ed. Imperial College Press, 2010. ISBN 978-1-84816-536-6.

[29] KRIVANEK, O. L.; DELBY, N.; MURFITT, M. F. Aberration Correction in Electron Microscopy. In: *Handbook of Charged Particle Optics*. 2nd ed. Boca Raton: CRC Press, 2009, pp. 601–640. ISBN 978-1-4200-4554-3.

[30] SCHERZER, O. The Theoretical Resolution Limit of the Electron Microscope. *Journal of Applied Physics*. 1949, **20**(1), 20–29. ISSN 0021-8979. Available from DOI: 10.1063/1.1698233.

[31] MULLER, D. A. Structure and bonding at the atomic scale by scanning transmission electron microscopy. *Nature Materials*. 2009, **8**(4), 263–270. ISSN 1476-1122. Available from DOI: 10.1038/nmat2380.

[32] ARBOUET, A.; CARUSO, G. M.; HOUDELLIER, F. Ultrafast Transmission Electron Microscopy: Historical Development, Instrumentation, and Applications. *Advancen in Imaging and Electron Optics*. 2018, **207**, 1–72. ISBN 9780128152157. ISSN 1076-5670. Available from DOI: 10.1016/bs.aiep.2018.06.001.

[33] RENS, J. F. M. van; VERHOEVEN, W.; KIEFT, E. R., et al. Dual mode microwave deflection cavities for ultrafast electron microscopy. *Applied Physics Letters*. 2018-10-15, **113**(16). ISSN 0003-6951. Available from DOI: 10.1063/1.5049806.

[34] BARWICK, B.; PARK, H. S.; KWON, O.-H., et al. 4D Imaging of Transient Structures and Morphologies in Ultrafast Electron Microscopy. *Science*. 2008-11-21, **322**(5905), 1227–1231. ISSN 0036-8075. Available from DOI: 10.1126/science.1164000.

[35] HAWKES, P. W. Aberrations. In: *Handbook of Charged Particle Optics*. 2nd ed. Boca Raton: CRC Press, 2009, pp. 210–339. ISBN 978-1-4200-4554-3.

[36]  ROSE, H. *Geometrical Charged-Particle Optics*. 2nd ed. Berlin: Springer, 2012. ISBN 978-3-642-32118-4.

[37]  KRIVANEK, O. L.; LOVEJOY, T. C.; MURFITT, M. F., et al. Towards sub-10 meV energy resolution STEM-EELS. *Journal of Physics: Conference Series*. 2014-06-11, **522**. ISSN 1742-6588. Available from DOI: 10.1088/1742-6596/522/1/012023.

[38]  *PDB Statistics*. Available also from: <https://www.rcsb.org/stats>.

[39]  PAL, S. *Fundamentals of Molecular Structural Biology*. Elsevier, 2020. ISBN 978-0-12-814855-6.

[40]  RAY, P.; KLAHOLZ, B. P.; FINN, R. D., et al. Determination of Escherichia coli RNA Polymerase Structure by Single Particle Cryoelectron Microscopy. *RNA Polymerases and Associated Factors, Part C*. 2003, 24–42. ISBN 9780121822736. Available from DOI: 10.1016/S0076-6879(03)70003-2.

[41]  DUBOCHET, J.; MCDOWALL, A. W. Vitrification of pure water for electron microscopy. *Journal of Microscopy*. 1981, **124**(3), 3–4. ISSN 00222720. Available from DOI: 10.1111/j.1365-2818.1981.tb02483.x.

[42]  CHO, H.-J.; HYUN, J.-K.; KIM, J.-G., et al. Measurement of ice thickness on vitreous ice embedded cryo-EM grids: investigation of optimizing condition for visualizing macromolecules. *Journal of Analytical Science and Technology*. 2013, **4**(1). ISSN 2093-3371. Available from DOI: 10.1186/2093-3371-4-7.

[43]  MCMULLAN, G.; FARUQI, A. R.; HENDERSON, R. Direct Electron Detectors. *The Resolution Revolution: Recent Advances In cryoEM*. 2016, 1–17. ISBN 9780128053829. Available from DOI: 10.1016/bs.mie.2016.05.056.

[44]  EGELMAN, E.H. The Current Revolution in Cryo-EM. *Biophysical Journal*. 2016, **110**(5), 1008–1012. ISSN 00063495. Available from DOI: 10.1016/j.bpj.2016.02.001.

[45]  SCHERES, S. H. W. Processing of Structurally Heterogeneous Cryo-EM Data in RELION. In: *Methods in Enzymology*. Academic Press, 2016, pp. 125–157. ISBN 9780128053829.

[46]  ZHANG, K. Gctf: Real-time CTF determination and correction. *Journal of Structural Biology*. 2016, **193**(1), 1–12. ISSN 10478477. Available from DOI: 10.1016/j.jsb.2015.11.003.

[47]  HENDERSON, R. Avoiding the pitfalls of single particle cryo-electron microscopy: Einstein from noise. *Proceedings of the National Academy of Sciences*. 2013-11-05, **110**(45), 18037–18041. ISSN 0027-8424. Available from DOI: 10.1073/pnas.1314449110.

[48]  CARRONI, M.; SAIBIL, H. R. Cryo electron microscopy to determine the structure of macromolecular complexes. *Methods*. 2016, **95**, 78–85. ISSN 10462023. Available from DOI: 10.1016/j.ymeth.2015.11.023.

[49]  *Falcon 3EC Direct Electron Detector*. 2018. Available also from:
      `<https://assets.thermofisher.com/TFS-Assets/MSD/Technical-`
      `Notes/Falcon-3EC-Datasheet.pdf>`.

[50]  HAWKES, P. W. *Magnetic Electron Lenses*. Berlin: Springer-Verlag Berlin
      Heidelberg, 1982. ISBN 978-3-642-81518-8.

# List of Abbreviations

| | |
|---|---|
| **ACTF** | Amplitude Contrast Transfer Function |
| **ADF** | Annular Dark-Field |
| **BF** | Bright-Field |
| **CCD** | Charge-Coupled Device |
| **CFEG** | Cold Field Emission Gun |
| **CMOS** | Complementary Metal-Oxide-Semiconductor |
| **CTF** | Contrast Transfer Function |
| **DF** | Dark-Field |
| **EOD** | Electron Optical Design |
| **HAADF** | High-Angle Annular Dark-Field |
| **PCTF** | Phase Contrast Transfer Function |
| **SA** | Selected-Area |
| **SPA** | Single Particle Analysis |
| **STEM** | Scanning Transmission Electron Microscope |
| **TEM** | Transmission Electron Microscope |